

ABSTRACT

ANDERSON, BRYAN DANIEL. Chemical Synthesis and Silica Overcoating of Nanoparticles with Tailored Morphologies (Under the direction of Joseph B. Tracy).

Colloidal nanoparticle chemistry is a blossoming branch of chemistry that is focused on the development and understanding of the composition, structure, and manipulation of nanoscale materials in solution. Efforts to construct functional materials using colloidal nanoparticles as the building blocks is necessary and can benefit useful applications and fundamental understandings in the field.

The overarching focus of this dissertation is to present a comprehensive discussion and present experimental studies on the chemical synthesis and silica overcoating of nanoparticles with tailored morphologies. The technical advancements that this thesis covers the following: (1) The synthesis of NPs with controlled chemistries and morphologies obtained through the Kirkendall effect, galvanic exchange, and anion exchange reactions. Through reacting template NPs with reactive precursors new types of nanoparticles with controlled morphologies can be obtained. (2) Controlling the deposition and structure of silica overcoatings on CdSe/CdS quantum dot nanorods. (3) Functionalizing the surface of silica coated quantum dot nanorods with iron oxide nanoparticles. (4) Creating composite nanofibers containing aligned Au nanorods and quantum dot nanorods to study the alignment of the nanorods and how physical properties of the nanorods can be used to modify the properties of the nanofibers and/or exploit unique properties of Au nanorods and semiconductor nanorods.

© Copyright 2016 Bryan Daniel Anderson

All Rights Reserved

Chemical Synthesis and Silica Overcoating of Nanoparticles with Tailored Morphologies

by
Bryan Daniel Anderson

A dissertation submitted to the Graduate Faculty of
North Carolina State University
in partial fulfillment of the
requirements for the degree of
Doctor of Philosophy

Materials Science and Engineering

Raleigh, North Carolina

2016

APPROVED BY:

Dr. Joseph B. Tracy
Committee Chair

Dr. Thomas H. LaBean

Dr. Linyou Cao

Dr. Orlin D. Velev

DEDICATION

To my wife (Amber), parents (Bruce and Joyce), and grandparents (Skip, Dee, Bob, and Ruth) for their everlasting love and wisdom.

BIOGRAPHY

I am the son of Bruce Dwayne Anderson and Joyce Eileen Beegle Anderson and was born in New Martinsville, West Virginia on January 5th, 1983. I am grandson of Robert “Bob” and Ruth Nice Anderson of New Martinsville, West Virginia and Burl “Skip” and Deloris “Dee” Deulley Beegle of Paden City, West Virginia. My parents and I moved to Creedmoor, North Carolina in June 1994.

I graduated from South Granville High School in Creedmoor in 2001. I then attended Vance-Granville Community College (VGCC) from 2001-2004. While studying at VGCC, I developed a fascination for how the world was put together in a way that supported life as we know it. In pursuit of the newly developed interest, I transferred from Vance-Granville in 2004 to North Carolina State University where I studied Geology. After receiving my B.S. in Geology in May 2007, I worked as a geologist for Unimin Corporation, where I conducted industrial mineral exploration, and for URS Corporation, where I conducted environmental remediation of contaminated soil and groundwater. In January 2011, I returned to graduate school at North Carolina State University to earn an MMSE and PhD in materials science and engineering under the direction of Dr. Joseph B. Tracy.

TABLE OF CONTENTS

LIST OF TABLES	viii
LIST OF FIGURES	ix
CHAPTER 1: Thesis Overview and Timeline of Projects	1
CHAPTER 2: Introduction	2
2.1 Background information	2
2.2 Quantum dots	3
2.2.1 Quantum dots: What are they and what defines them	3
2.2.2 Types of quantum dots: Type I, II, and III and quasi types	7
2.3 CdSe/CdS Quantum Dot Nanorods	9
2.3.1 Synthesis of heterostructured anisotropic CdSe/CdS QDNRs: Factors that control the formation of anisotropic nanostructures	9
2.3.2 Properties of CdSe/CdS QDNRs	10
2.4 Silica: For Use in Nanoparticle Composites	11
2.4.1 Types, properties, and the significance of silica	11
2.4.2 Significance of silica as an earth-based material	11
2.4.3 Crystalline versus amorphous silica	13
2.4.5 The surface chemistry of silica	16
2.5 References	19
Chapter 3: Nanoparticle Conversion Chemistry: Kirkendall Effect, Galvanic Exchange, and Anion Exchange	23

3.1 Motivation.....	23
3.2 Manuscript Reprint	24
CHAPTER 4: Silica Overcoating of CdSe/CdS Quantum Dot Nanorods with Tunable Morphologies	48
4.1 Motivation.....	48
4.2 Manuscript Reprint	49
CHAPTER 5: Synthesis of Fe₃O₄-SiO₂-QDNR Nanocomposites	66
5.1 Introduction.....	66
5.2 Experimental Details.....	66
5.2.1 Chemicals.....	66
5.2.2 Nanoparticle synthesis	67
5.2.3 Structural characterization	70
5.2.4 Optical characterization	70
5.3 Results and Discussions.....	70
5.4 Conclusions.....	75
5.4 References.....	76
CHAPTER 6: Synthesis of Electrospun Polymer Fiber Nanocomposites and Polarization Anisotropy Dependence of Energy Transfer between Gold Nanorods and CdSe/CdS Quantum Dot Nanorods.....	78
6.1 Introduction.....	78
6.2 Experimental Details.....	80

6.2.1 Chemicals.....	80
6.2.2 Nanoparticle synthesis	80
6.2.3 Structural characterization	82
6.2.4 Optical characterization	83
6.3 Results and Discussion	84
6.3.1 Alignment of QDNRs, GNRs, and PEG-SiO ₂ -QDNRs in PEO fibers	84
6.3.2 Conclusions and ongoing work.....	92
6.4 References.....	93
CHAPTER 7: Silica and Cobalt-Silica Aerogel Composites.....	97
7.1 Introduction.....	97
7.2 Experimental Details.....	98
7.2.2 Material synthesis	98
7.2.3 Structural characterization	100
7.3 Results and Discussion	100
7.4 Conclusions.....	104
7.5 References.....	105
CHAPTER 8: Contributions to Other Projects	107
8.1 Airbrushed Nickel Nanoparticles for Large-Area Growth of Vertically Aligned Carbon Nanofibers on Metal (Al, Cu, Ti) Surfaces ¹	107
8.2 Transfer of Vertically Aligned Carbon Nanofibers to Polydimethylsiloxane (PDMS) While Maintaining their Alignment and Impalefection Functionality ²	109

8.3 Silica overcoating of nickel and Fe ₃ O ₄ nanoparticles in a reverse microemulsion	110
8.4 Synthesis of porous nickel sulfide nanoparticles obtained through the Kirkendall effect	112
8.5 Surface modification and convective assembly of PbS nanoparticles	113
8.6 References	115

LIST OF TABLES

Chapter 2

Table 1. Chemical composition (wt%) of Earth, mantle, and crust. Data obtained from Ref. 18.....	12
Table 2. Polymorphs of crystalline SiO ₂ . Data obtained from Ref. 19.....	14

Chapter 4.

Table S1. Parameters for synthesizing fully encapsulated and lobed SiO ₂ -QDNRs with different lengths.....	61
-------------------------------------------------------------------------------------------------------------------------------	----

LIST OF FIGURES

Chapter 2

Figure 1. A schematic of an exciton in the bulk state and quantum-confined state5

Figure 2. A description of quantum dots. (a) A schematic illustrating how the band gap changes with respect to the change in sizes of quantum dots. (b) Typical optical spectra of CdSe quantum dots (c) Various solutions of CdSe quantum dots of different sizes emitting light (d) Spectral ranges of quantum dots of different compositions6

Figure 3. A schematic of ligand stabilized core/shell colloidal quantum dot.....7

Figure 4. A schematic of the band gap configurations of different types of core/shell quantum dots9

Figure 5 Types of silanol and siloxane bridges found in colloidal silica particles that includes infrared spectroscopy data of 3750 cm^{-1} and 3660 cm^{-1} that represent single and vicinal groups, respectively. Q^n is used in NMR analyses where n indicates the number of bridging oxygens bound to a single Si.....17

Figure 6. Silica gel modification schemes using (a) long chain aliphatic alcohols, (b) triethoxysilane, (c) chlorosilane, and (d) chlorination of silica surface and subsequent modification with Grignard reagent.....18

Chapter 3

Scheme 1. Graphical depictions of examples of NP conversion chemistry. (a) Kirkendall effect: during the reaction of the metal (M) with reactive species X to form MX_n , void formation occurs. (b) Galvanic exchange: reduction of ions (N^{IV+}) of a more noble metal (N) drives oxidation of a less noble metal (M), which dissolves into solution (M^{w+}) through

pinholes formed in the shell. (c) Anion exchange: during the reaction of a metal compound (MY) with a reactive anion (X^{2-}), anions (Y^{2-}) are released to form MX. Void formation through the Kirkendall effect can occur when cations diffuse outward to react with the reactive anions.....27

Figure 1. TEM and corresponding graphical depictions of morphological changes through the Kirkendall effect during the oxidation of 26 nm diameter Ni NPs under ambient atmosphere at 300 °C for (a and k) 90, (b and l) 120, (c and m) 150, (d and n) 180, and (e and o) 210 min. Formation of a single void at the core/shell interface causes asymmetrical outward diffusion of Ni, resulting in a non-uniform NiO shell thickness.....29

Scheme 2. Graphical depiction of the initial stages of oxidation of a metal NP according to the Cabrera–Mott model, resulting in a thin metal oxide layer. An electric field generated in the metal oxide layer drives diffusion of ions and flow of electrons through the oxide layer.....29

Figure 2. TEM images showing the formation of thin oxide shells on Fe NPs in air at room temperature. After rapid formation of the initial thin oxide, the oxidation rate slows by several orders of magnitude.....29

Figure 3. Cyclic transformations of hollow MnO–SiO₂ NPs with small embedded Pt NPs into Mn₃O₄/SiO₂ core/shell NPs with small PtO NPs embedded in the shell by heating in air. Subsequent heating with H₂ drives the reverse reaction.....31

Figure 4. Overview with inset TEM and XRD measurements of the chemical levers that control the composition, size, and morphology of Ni_xP_y NPs. Low P : Ni precursor ratios resulted in large, hollow NPs, while higher P : Ni precursor ratios gave small, solid NPs.....32

Figure 5. Successive phosphidation reactions of Co NPs with TOP at elevated temperature. After formation of an amorphous Co–P shell, outward diffusion of Co results in hollow, crystalline Co₂P NPs. Further phosphidation into CoP can occur through two mechanisms: (a) the void size and outer diameter increase as a result of further outward diffusion of Co through the Kirkendall effect. (b) Fragmentation into smaller solid NPs, which may then grow into larger sizes through Ostwald ripening.....33

Figure 6. Graphical representations and corresponding TEM images of the products for several conversion chemical reactions of large Cd NPs: (a) oxidation gives urchin-shaped CdO NPs, (b) a large excess of S in dichlorobenzene (DCB:S) produces hollow CdS NPs with high inner : outer radius ratios, (c) smaller amounts of DCB:S or use of TOP:S drive formation of hollow CdS NPs with low inner:outer radius ratios, (d) TOP:Se produces hollow CdSe NPs, and (e) TOP:Te produces hollow CdTe NPs, as well as (e, inset) smaller solid CdTe NPs.....33

Figure 7. (a–d) TEM images and graphical schematics below for different morphologies of NPs during or after conversion chemical reactions, where void formation occurs through the Kirkendall effect. (a) Ni/NiO core/shell NP, where the core is asymmetrically positioned on the inside of the shell, resulting in non-uniform shell thickness, (b) Cd/CdS core/ shell NP, where the core is asymmetrically positioned on the inside of the uniformly thick shell, (c) Co/CoSe core/shell NP, where the core is suspended symmetrically within the void space by filaments extending from the core to the shell, and (d) Ni₂P yolk/shell NP displaying a core completely separated from the shell that floats freely within the void space.....34

Figure 8. a) Graphical schematic showing the process for synthesizing Au/Co core/shell NPs, assembling them into chains, and converting them into Au/Co₃O₄ nanowires. TEM images of chained (b) Au/Co core/ shell NPs and (c) Au/Co₃O₄ core/shell NPs, where Au is located asymmetrically within the voids formed during oxidation of Co into Co₃O₄.....35

Figure 9. (a) Graphical schematic depicting the stepwise formation of hollow PtBi NPs and TEM images showing (b) aggregates of Pt NPs, (c) Bi₂O₃ sheets surrounding the Pt NP aggregates, (d) Bi NPs formed within the Bi₂O₃ sheets, and (e) hollow or porous PtBi NPs..37

Figure 10. Graphical schematic and TEM images for galvanic exchange reactions of Ag NPs with K₂PtCl₄ in the presence of HCl under different reaction conditions, resulting in (a) nanoboxes, (b) heterodimers, (c) multimers, and (d) popcorn-shaped NPs.....38

Figure 11. TEM images showing galvanic exchange in oxide NPs: (a) starting Mn₃O₄ nanocubes and (b) the γ -Fe₂O₃ nanocage product.....39

Figure 12. TEM images acquired at different stages of anion exchange of ZnO NPs with hexamethyldisilathiane, resulting in ZnS NPs: (a) solid ZnO NPs with HRTEM inset, (b) partial anion exchange products, ZnO/ZnS core/shell NPs with prominent voids formed through the Kirkendall effect, and (c) hollow ZnS NPs obtained after complete anion exchange with HRTEM inset. (d) Reconstructed image from fast Fourier transform (FFT) spots showing heteroepitaxial growth of ZnS onto ZnO during partial anion exchange. Alignment of the spots in the inset FFT confirms epitaxy.....40

Figure 13. a) Graphical schematic depicting stepwise formation of multi- shelled Cu₂S hollow NPs through anion exchange at 220 °C. TEM images of (b) double-shelled NPs and (c) a mixture of double- and triple-shelled NPs.....40

Figure 14. TEM images of Au–Ge–(Ag)_nNPs. Multiple Ag NPs were deposited onto the Ge domains through a selective galvanic exchange reaction, where the Au domains remained unperturbed. Lower panels display individual Au–Ge–(Ag)_nNPs.....41

Chapter 4

Figure 1. TEM images show morphological control of SiO₂ shells on short CdSe/CdS core/shell QDNRs (AR of 8.0) by varying the amounts of TEOS and water. (a) 15 μL and (b) 30 μL of TEOS give single and double lobes of SiO₂ at the ends of the QDNRs, respectively. (c) Addition of 256 μL of water (giving a total of 298 μL, when combined with 42 μL from NH₄OH) results in fully encapsulated QDNRs.....52

Figure 2. Histograms of length distributions measured by TEM of QDNR cores in the samples presented in Figure 1: (a) fully encapsulated SiO₂-QDNRs, (b) single-lobed and double-lobed SiO₂-QDNRs, and (c) subpopulations of different morphologies within the double-lobed sample.....53

Figure 3. Varying the amount of water during SiO₂ deposition on high-AR QDNRs (initial length of 134.1 nm and AR of 19.1) gives morphological control, shown in TEM images of (a) lobed (84 μL of water) and (b) fully encapsulated SiO₂-QDNRs (576 μL of water).....53

Figure 4. TEM images at (a) low and (b) high magnifications of the same sample of SiO₂-QDNRs prepared with a reduced concentration of CO520, which are crosslinked at their ends.....54

Figure 5. (a-e) Representative TEM images from injection of PEG-silane (a) 1 hour, (b) 3 hours, (c) 10 hours, and (d) 20 hours after addition of TEOS, compared with (e) no injection

(24 hours). (f) Dependence of the SiO₂ shell thickness on the PEG-silane injection time. The scale bar in (a) applies to all panels.....54

Figure 6. QYs of QDNRs and SiO₂-overcoated QDNRs of different ARs and morphologies.....55

Figure S1. TEM images of (a) CdSe QD seeds and typical CdSe/CdS QDNRs with average lengths of (b) 50 nm, and (c) 101 nm.....60

Figure S2. Normalized optical (a,b) absorbance spectra and (c,d) emission spectra of QDNRs and SiO₂-QDNRs reported in Figure 6 with aspect ratios of (a,c) 6.0 and (b,d) 9.1.....62

Figure S3. TEM images of the samples presented in Figure 6: (a) QDNRs with an AR of 6.0 were used to synthesize (b) fully encapsulated SiO₂-QDNRs. (c) QDNRs with AR of 9.1 were used to synthesize (d) single-lobed SiO₂-QDNRs and (e) fully encapsulated QDNRs.....63

Figure S4. Asymmetric, lobed SiO₂ overcoatings on QDNRs with an initial length of 134.1 nm and an AR of 19.1.....64

Figure S5. Histogram of length distribution measured by TEM for SiO₂-QDNRs presented in Figure 3a, synthesized using 30 μL of TEOS. The initial length of the bare QDNR was 134.1 nm (AR of 19.1).....65

Chapter 5

Figure 1. TEM images of (a) SiO₂-QDNRs used in the synthesis of (b) Fe₃O₄-SiO₂-QDNRs produced by thermal decomposition of Fe(acac)₃.....71

Figure 2. Heat treatment of SiO₂-QDNRs. (a-b) are TEM images of the SiO₂-QDNRs post heat treatment in benzyl ether and oleylamine at 290 °C. Normalized optical (c) absorbance spectra and (d) emission spectra.....73

Figure 3. Optical absorbance and emission spectra of SiO₂-QDNRs (a) before and (b) after heat treatment in benzyl ether and oleylamine at 290 °C.....75

Figure 4. TEM images of (a) SiO₂-QDNRs used in the synthesis of (b) Fe₃O₄-SiO₂-QDNRs produced by ligand crosslinking.....75

Chapter 6

Figure 1. SEM and TEM images of electropun PEO fibers containing embedded nanorods. SEM images of (a) randomly oriented and (b) aligned fibers. TEM images of aligned (a) CTAB functionalized QDNRs and (b) CTAB stabilized GNRs in PEO fibers.....85

Figure 2. An illustration and TEM images of PEG-SiO₂-QDNRs in PEO fibers. (a) is an illustration showing the generalized structure of the fiber. TEM images of PEG-SiO₂-QDNRs with (a) large AR and (b) small AR embedded in PEO fibers.....86

Figure 3. STEM images of aligned GNRs and PEG-SiO₂-QDNRs embedded in PEO nanofibers. (a) bright field lower magnification image and (b) dark field image show the structure of the fibers.....87

Figure 4. Polarized absorbance and emission spectra of QDNRs in PEO nanofibers.....89

Figure 5. Optical spectra of QDNRs and GNRs. (a) Optical absorbance and emission spectra of QDNRs and (b) emission spectra of QDNRs and absorbance spectra of GNRs that were used to fabricate the composite NFs.....90

Figure 6. Schematic of the types of nanofiber composites that were used to optically characterize.....91

Figure 7. Fluorescence lifetime spectra of QDNR-GNR nanofiber composites with random orientation.....92

Chapter 7

Figure 1. A simplified schematic for the synthesis of an aerogel.....101

Figure 2. A photograph of the supercritical dryer built in our lab for the synthesis of SiO₂ and Co-SiO₂ composite aerogels.....102

Figure 3. TEM images of colloidal Co NPs used for fabricating the Co-SiO₂ composite aerogels.....103

Figure 4. TEM images of (a) SiO₂ aerogel and (b) Co-SiO₂ aerogel composite.....104

Chapter 8

Figure 1. (a) TEM image of 150 nm Ni NPs used to grow VACNFs. (b) A schematic illustrating a simplified method of depositing Ni NPs and silicon powder to grow VACNFs. (c) SEM images of VACNFs grown on aluminum, copper, and titanium substrates.....108

Figure 2. Images of Ni NPs, VACNFs, and VACNFs embedding PDMS (a) TEM images of the Ni NPs (b) SEM image of the silicon nitride coated VACNFs grown an aluminum substrate (c) EDX map illustrating the location of silicon in the same area as panel b (d) EDX map illustrating the location of aluminum in the same area as panel b (e) VACNFs that project from the surface of PDMS.....110

Figure 3. TEM images of SiO₂ overcoated Fe₃O₄ NPs with (a) low loading of NPs and (b) high loading of Fe₃O₄ NPs.....112

Figure 4. A table indicating the compositions of nickel sulfide synthesized and TEM images of the formation of porosity when Ni NPs react to form nickel sulfide.....113

Figure 5. TEM images of (a) PbS NP (b-e) SiO₂ overcoated PbS NPs. The images show that the PbS NPs partially decompose during the SiO₂ overcoating synthesis.....115

CHAPTER 1: Thesis Overview and Timeline of Projects

The objective of this thesis is two-fold. First, I thoroughly discuss the synthesis of NPs with controlled chemistries and morphologies. I have conducted a thorough investigation on modifying the surface chemistry of semiconductor nanorods with organic molecules, amorphous silica, and other types of inorganic NPs. Additionally, within the scope of synthesizing NPs with controlled chemical makeup and morphologies, I discuss my work in governing chemical compositions and structures of NPs through nanoparticle conversion chemistry. The second part of this thesis is to integrate multifunctional composite NPs into polymer nanofiber composites with semiconductor nanorods, iron oxide nanoparticles, and plasmonic Au nanorods. The objective was to study the alignment of the nanorods and how physical properties of the nanorods can be used to modify the properties of the nanofibers and/or exploit unique properties of Au nanorods and semiconductor nanorods by embedding them into polymer nanofibers.

I arrived at NC State University to earn my PhD in January 2011. I immediately began working in Dr. Tracy's research group, and my first project was on the synthesis of silica and metal nanoparticle composite aerogels. Through this project, I built supercritical dryer reactor and synthesized metal nanoparticle (NP) and silica composite aerogels. During this time, we shifted our focus onto the airbrushing project. In this project, I developed my skills on the synthesis of Ni and Co NPs and worked on a team using airbrushing to deposit large area arrays of Ni NPs used for growing vertically aligned carbon nanofibers. Our research group became interested conducting research on colloidal quantum dots. Therefore, I developed a plan of research to overcoat CdSe/CdS quantum dot nanorods (QDNRs) with

silica overcoatings, fabricate nanofiber composites, and overcoat them with magnetic nanoparticles. At the end of the air brush project, I gained some experience in synthesizing Ni and Co NPs and did some work on nanoparticle conversion chemistry. So, we extended this work and I authored a review article on NP conversion chemistry and led a team of undergraduate students in performing experiments on the synthesis of nickel sulfide nanoparticles through NP conversion chemistry.

CHAPTER 2: Introduction

2.1 Background information

The study of nanoparticle (NP), also referred to as nanocrystal, chemistry has been of significant interest to many disciplinary fields. Due to the unique physical properties of colloidal NPs, their understanding, development, and employment into functional materials and devices is becoming an important issue in the world's economies and environmental issues due to the demand for higher performing and safer technologies. NPs are important because they bridge the gap between individual atoms and small molecules to bulk materials, which make them useful for many different types of applications.

There are at least three major contributing factors that give NPs their unique properties. The first contributor is the inherent surface chemistry of the NPs. For colloidal NPs, the surface chemistry is strongly dictated by the stabilizing ligands that are bound to the surface of the core material. The second contributor is the chemical composition of the NP core. The third contributor is the morphology of the core material. NP shape and morphology strongly affect the properties of the NPs.

The solvothermal method is a common approach to synthesizing thermodynamically stable colloidal NPs with well controlled compositions, structures, and surface chemistries. Solvothermal synthesis is typically conducted at pressures between 1 atm to 10,000 atm and temperatures between 100 °C and 1,000 °C. These pressures and temperatures allow for decomposition and reactions of NP precursors. Solvothermal syntheses are conducted with organic solvents, unlike hydrothermal methods, where NPs are synthesized in water.

2.2 Quantum dots

2.2.1 Quantum dots: What are they and what defines them

Quantum dots (QDs) are a type of semiconductor NP where there is a size-dependent relationship of the nanoparticle to the optical and electronic properties. The behavior of an exciton in a semiconductor can be best described by the “particle in a box” model. In bulk semiconductors, a band gap exists that separates the electron valence and conduction bands. When the electrons in the material are excited into the conduction band, an exciton consisting of an electron and electron hole is generated (**Figure 1**). Depending on the condition, multiple excitons can be generated within the material. When excitons are generated in a semiconductor material, there is an average distance in physical separation between the electron and the electron hole, referred to as the exciton Bohr radius. This physical distance is different for each material but, typical exciton Bohr radii of semiconductor materials is on the order of a few nanometers. The exciton Bohr radius of a particle can be described as

$$a_B = \varepsilon \frac{m}{m^*} a_o \quad (1.1)$$

where ϵ is the material dielectric constant, m^* is the particle mass, m is the rest mass of the electron, and a_0 is the Bohr radius of the hydrogen atom. In bulk semiconductors, the dimensions of the semiconductor crystal are much larger than the exciton Bohr radius, allowing the exciton to extend to its natural limit. In this regime, the electron energy levels in the semiconductor material are averaged and are continuous (**Figure 2a**). However, if the size of a semiconductor NP becomes small enough that it approaches the size of the material's exciton Bohr Radius, then the electron energy levels can no longer be treated as continuous - they must be treated as discrete, meaning that there is a small and finite separation between energy levels. When the electron energy levels become discrete and the material properties begin to diverge from bulk state. The electrons are quantum confined and, depending on the dimensions at which the electrons are confined, the material can be called a quantum well, quantum wire, and QD (**Figure 1 and 2a**). This has large repercussions on the absorptive and emissive behavior of the semiconductor material during radiative recombination of the electron with the hole (**Figure 2b and 2c**). The band gap of the quantum-confined exciton can be adjusted based on the size of the QD due to a higher degree of confinement of the exciton. The size tunability of the band gap in QDs can be observed in the absorbance and optical emission spectra (**Figure 2c**). The core composition of the QD also determines the emission wavelength from the UV to infrared (**Figure 2d**).

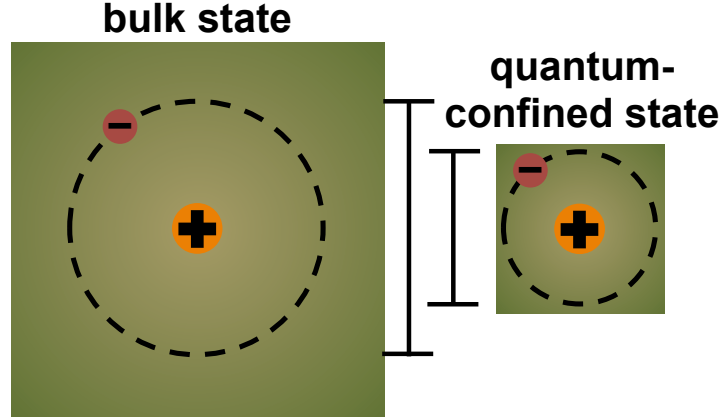


Figure 1. A schematic of an exciton in the bulk state and quantum-confined state.

The effective-mass approximation model can be used to show the confinement energy levels of quantum wells, quantum wires, and QDs through the Schrödinger equation. The effective-mass solutions for the Schrödinger equation for the quantum nanostructures are:

Quantum well:

$$E_n(k_x k_y) = \frac{\pi^2 \hbar^2 n^2}{2m^* L_z^2} + \frac{\hbar^2}{2m^*} (k_x^2 + k_y^2), \psi = \phi(z) \exp(ik_x x + ik_y y) \quad (1.2)$$

Quantum wire:

$$E_{n,m}(k_x) = \frac{\pi^2 \hbar^2}{2m^*} \left(\frac{n^2}{L_z^2} + \frac{m^2}{L_y^2} \right) + \frac{\hbar^2 k_x^2}{2m^*}, \psi = \phi(z) \phi(y) \exp(ik_x x) \quad (1.3)$$

Quantum dot:

$$E_{n,m,l} = \frac{\pi^2 \hbar^2}{2m^*} \left(\frac{n^2}{L_z^2} + \frac{m^2}{L_y^2} + \frac{l^2}{L_x^2} \right), \psi = \phi(z) \phi(y) \phi(x) \quad (1.4)$$

where n , m , and l are quantum confinement integers, m^* is the effective mass of the particle, \hbar is Planck's constant, L_x, L_y , and L_z are confining dimensions, and $\exp(ik_x x + ik_y y)$ is the electronic wave function describing the motions in the x and y directions.

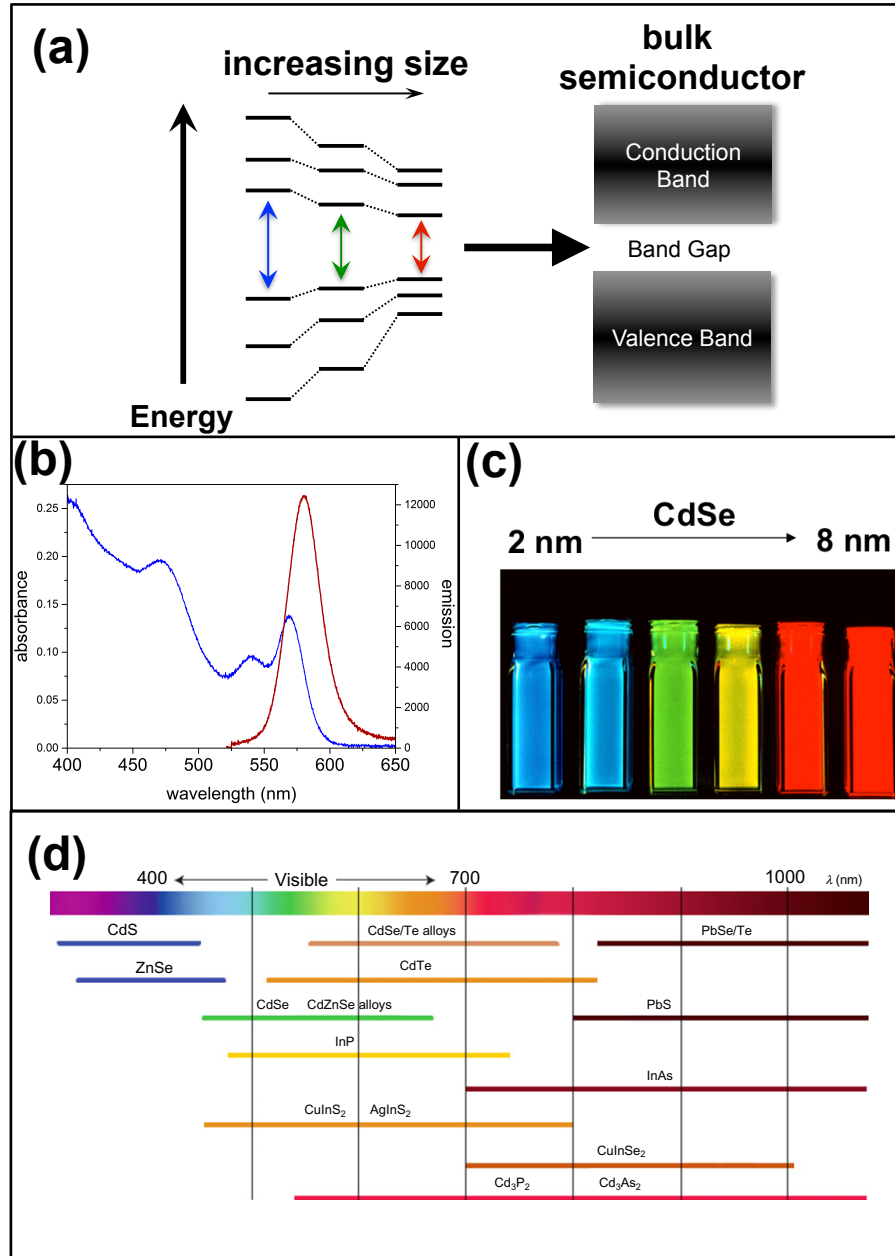


Figure 2. A description of quantum dots. (a) A schematic illustrating how the band gap changes with respect to the change in sizes of quantum dots. (b) Typical optical spectra of

CdSe quantum dots. (c) Various solutions of CdSe quantum dots of different sizes emitting light. (d) Spectral ranges of quantum dots of different compositions data in this part of the figure are from Ref. 1

2.2.2 Types of quantum dots: Type I, II, and III and quasi types

The environment surrounding QDs can affect the behavior of generated excitons. A general strategy to shield QDs from their local environment is to functionalize the surface of the QD with an organic capping ligand (**Figure 3**). While the capping ligand do serve to protect the QD to a certain extent, the ligand itself can act as a surface trap and can result in non-radiative decay of the excited electron. In order to mitigate the strong ligand effects on the generated exciton, one or more inorganic semiconducting layers can be added to the surface of the QD to create a core/shell structure (**Figure 3**). Some example core/shell compositions include, but is not limited to, CdSe/CdS, CdSe/ZnTe, ZnTe/CdSe, PbSe/PbS, CdS/PbS, and CdSe/ZnS.²⁻⁵.

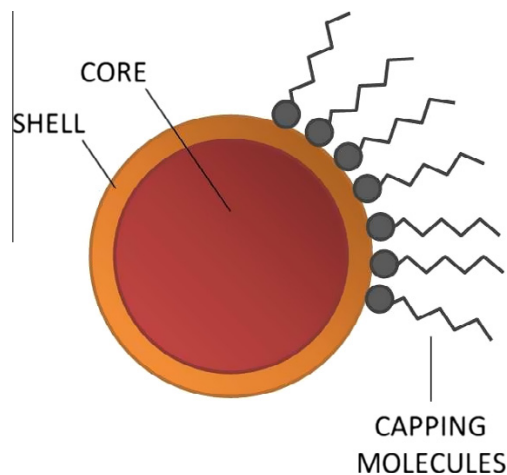


Figure 3. A schematic of ligand stabilized core/shell colloidal quantum dot. Schematic obtained from Ref. 6

The semiconductor materials that compose a core/shell QD impose a band gap structure on the NP that strongly influences the behavior of excitons, which ultimately determines the optical behavior. Each semiconductor material has a known bandgap and, depending on the relative energies of the valence and conduction bands, different classes of core/shell QDs can exist (**Figure 4**). Type I core/shell QDs occur when the core material has a smaller band gap and resides within the band gap of the shell material. Upon excitation, the exciton resides within the core, since the excited charge carriers occupy the lowest electronic states. Conversely, core/shell QDs with an inverse type I band gap structure can exist, where the exciton will reside within the shell upon excitation. A type II QD is formed when the band gaps of the core and the shell are staggered and there is a spatial separation between the excited charge carriers, where one of the carriers (either the electron or the hole) will be delocalized in the core and the other carrier will be delocalized to the shell. In a quasi-type II system, one of the band edges of the core and shell will be aligned. The aligned edge allows for partial charge separation between the two charge carriers, where one carrier can be delocalized and can migrate through the core and the shell. For example, for a quasi-type II system where the conduction bands are aligned, the hole will be confined to the core, while the electron will occupy the entire nanostructure.

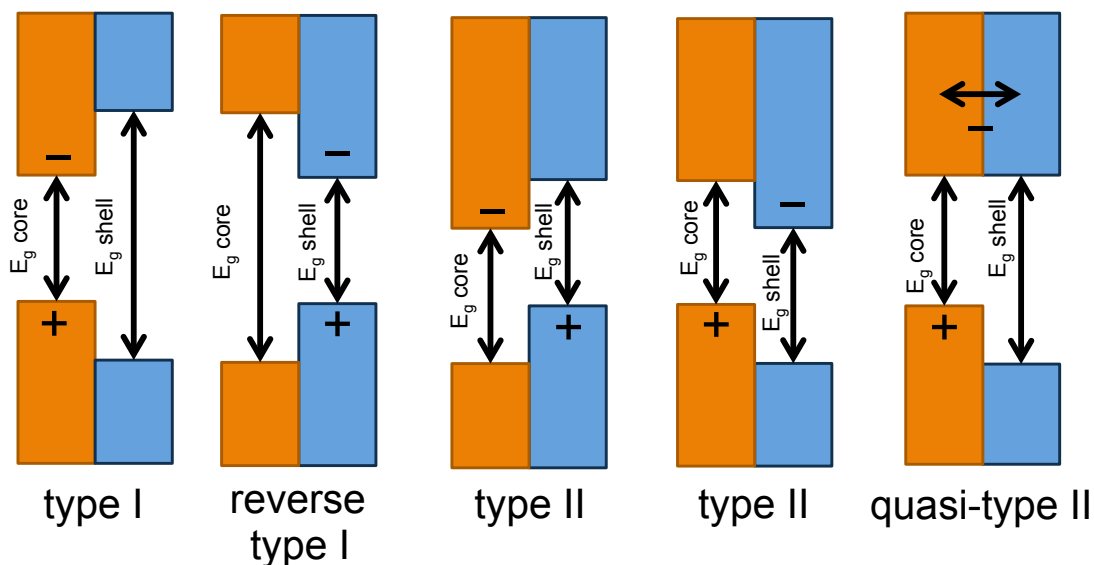


Figure 4. A schematic of the band gap configurations of different types of core/shell quantum dots.

2.3 CdSe/CdS Quantum Dot Nanorods

A partial focus of this thesis is the synthesis of NPs with anisotropic shapes.

Advances in the development and synthesis of semiconductor nanocrystals have improved, such that we can now have tight controls on the morphology of the NPs in addition to controlling the basic chemistry.⁷ This section of the thesis will review the properties of CdSe/CdS quantum dot nanorods (QDNRs) and the developments in semiconductor NP syntheses that control NP chemistry and morphology.

2.3.1 Synthesis of heterostructured anisotropic CdSe/CdS QDNRs: Factors that control the formation of anisotropic nanostructures

One of the more common methods in synthesizing CdSe/CdS QDNRs is through seeded growth.⁸ In the seeded growth approach to synthesizing colloidal QDNRs with anisotropic morphologies, a CdSe seed with a hexagonal wurtzite crystal structure serves as a

template for the epitaxial overgrowth of a CdS shell. The CdS shell is also hexagonal wurtzite and grows parallel to the c-axis direction due to polarity in the crystal structure.⁹ There are several factors that are involved in the controlled growth of the CdSe/CdS QDNRs.

The CdSe seed crystal structure has been found to be the primary factor in controlling the growth of the CdS shell.⁷ The crystal structure of the seed can be controlled by through controlling reaction conditions such as the growth temperature and through the use of alkyl phosphonic acids ligands.^{10, 11} The use of phosphonic acids has been a critical parameter that has shaped the development of seeded growth of anisotropic semiconductors. Long-chained phosphonic acids have been shown to promote the stabilization of wurtzite CdSe seeds, while short-chained phosphonic acids stabilized zinc blende CdSe seeds.¹² During CdS shell growth, phosphonic acids bind more strongly to Cd and S in the (001) planes, causing growth in the (0001) facets. It has been shown that oleylamine binds more strongly in the (0001) plane and HPA preferentially binds in the (001) plane.¹³ As a result of oleylamine's stronger binding affinity, CdSe/CdS hexagonal platelets were synthesized.

2.3.2 Properties of CdSe/CdS QDNRs

The physical properties, such as optical, excitonic, and band gap characteristics, of CdSe/CdS QDNRs are closely associated with the anisotropic 1D dimensional shape of the NP. Sitt *et al.* has provided a nice review article that provides a nice summary of the physical properties associated with seeded semiconductor nanorods, include CdSe/CdS QDNRs.¹⁴ Quantum yields for the CdSe/CdS QDNRs in the projects discussed in this thesis are approximately 75-80% for short aspect ratios.⁸ The radiative recombination rate decreases as the nanorod volume increases likely from an increased number of defects in the CdS shell

that serve as electron traps. Traps in the CdS shell affect the behavior of the electron and can result in non-radiative decay. The CdSe/CdS QDNRs exhibit a quasi-type II band gap configuration and, during the generation of an exciton, partial charge separation occurs where the hole is confined to the core and the electron is delocalized throughout the nanostructure.¹⁵ A recent study has found that there is approximately a 25% chance that the electron can be found in the shell and the mobility is about $700 \text{ cm}^2 / (\text{V s})$ along the QDNR c-axis.¹⁶ The mobility was about 1.6 times greater than the electron mobility in bulk CdS, which can be attributed to higher electron-phonon scattering and quantum confinement effects on the electronic structure of the nanostructure.¹⁶ An additional feature that CdSe/CdS QDNRs exhibit is polarization anisotropy in the absorbance and emission spectra with a degree of polarization ranging from 0.45 to 0.6.^{16, 17} These properties of the QDNRs made them attractive for employing in my studies.

2.4 Silica: For Use in Nanoparticle Composites

2.4.1 Types, properties, and the significance of silica

This section will discuss the significance of silica as a naturally occurring material and how its properties make it suitable for use as an engineering material.

2.4.2 Significance of silica as an earth-based material

Next to iron, of which a large portion is estimated to be found in Earth's core, silicon and oxygen are two of the most abundant elements that make up the composition of Earth (**Table 1**). In geochemistry, oxygen and silicon most often form a compound in the form of SiO_2 (commonly referred to as "silica"). In the outer most surfaces of the Earth, including

the mantle and crust (oceanic and continental), SiO₂ is the most abundant compound found. In particular, continental and oceanic crusts are mostly composed of SiO₂ where they contain approximately 49.4 and 60.3 wt. % of SiO₂, respectively.

Table 1. Chemical composition (wt.%) of Earth, mantle, and crust.
Data obtained from Ref. 18

Element	Earth	Oxide	Mantle	Oceanic crust	Continental crust
Fe	31	SiO ₂	45.2	49.4	60.3
O	30	TiO ₂	0.71	1.4	1
Si	18	Al ₂ O ₃	3.54	15.4	15.6
Mg	16	FeO ^d	8.48	10.1	7.2
Ni	1.7	MnO	0.14	0.3	0.1
Ca	1.8	MgO	37.48	7.6	3.9
Al	1.4	CaO	3.08	12.5	5.8
Na	0.9	Na ₂ O	0.57	2.6	3.2
		K ₂ O	0.13	0.3	2.5
		P ₂ O ₅	-	0.2	0.2

Silicon and oxygen routinely combine with metal cations to form an intricate class of silicate minerals. The silicate mineral class is an important class of minerals that make a majority of the Earth's crust where it makes up well over 90% of the crust and is a major component of the igneous, metamorphic, and sedimentary rock types.¹⁹ The SiO₄ tetrahedron is fundamental unit on which the structure of all silicates is based. It consists of four O²⁻ at the apices of a regular tetrahedron surrounding and coordinated by one Si⁴⁺ at the center. The strong bond between Si⁴⁺ and O²⁻ gives silica and related silicate minerals their unique properties. From a geological point of view, these properties that arise between the silicon and oxygen ions helps give Earth's crust fundamental properties that is able to sustain life. From an industrial and technological point of view, these strong bonds give the natural and

synthetic varieties of silicate minerals important properties that make them useful in many types of important technologies and applications. Both crystalline and amorphous forms of silica has traditionally, and is currently, a fundamental material that helps leads the front of developing new technologies that results in the advancement of the humans.

2.4.3 Crystalline versus amorphous silica

The tectosilicate mineral class is defined as the crystallization of SiO_4 tetrahedra that constructs a three-dimensional framework. The sharing of oxygen ions that result in the linking of SiO_4 tetrahedra, give a ratio of Si : O of 1 : 2. There are at least nine distinct polymorphs of SiO_2 (**Table 2**). Stishovite and coesite are high pressure, high temperature polymorphs of SiO_2 often associated with meteor impacts. Coesite is also found in ultrahigh pressure metamorphic rocks. The other SiO_2 polymorphs can be categorized into three primary classes. They are the low quartz, low tridymite, and low cristobalite. Low quartz exhibits the lowest crystal symmetry and most dense crystal structure while the crystal symmetry increases and density decreases with low tridymite and low cristobalite. Low cristobalite has the highest symmetry and least compact crystal structure.

Table 2. Polymorphs of SiO₂. Data obtained from Ref. 19

Name	Crystal Symmetry	Space Group	Specific Gravity	Refractive Index (Mean)
Stishovite*	Tetragonal	P4 ₂ /mmm	4.35	1.81
Coesite	Monoclinic	C2/c	3.01	1.59
Low (α) quartz	Hexagonal	P3 ₂ 21 (or P3 ₁ 21)	2.65	1.55
High (β) quartz	Hexagonal	P6 ₂ 22 (or P6 ₄ 22)	2.53	1.54
Keatite (synthetic)	Tetragonal	P4 ₁ 2 ₁ 2 (or P4 ₃ 2 ₁ 2)	2.50	1.52
Low (α) tridymite	Monoclinic or Orthorhombic	C2/c (or Cc)	2.26	1.47
High (β) tridymite	Hexagonal	P6 ₃ /mmc	2.22	1.47
Low (α) cristobalite	Tetragonal	P4 ₁ 2 ₁ 2 (or P4 ₃ 2 ₁ 2)	2.32	1.48
High (β) cristobalite	Isometric	Fd3m	2.20	1.48

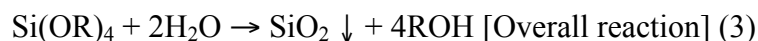
While the importance of crystalline SiO₂ is important on many levels, amorphous silica is also of great interest. This following will outline the synthesis and properties of porous amorphous silica. Two approaches are chiefly used in the synthesis of synthetic amorphous SiO₂ particles.

One approach in the synthesis of SiO₂ particles through the Stöber method.²⁰ This approach typically uses a low molecular mass alcohol, such as ethanol and methanol, in the presence of ammonia and water. Water hydrolyzes TEOS molecules and ammonia base-catalyzes the nucleation and growth of SiO₂ particles that range in size from 5 nm to 2 μm. There are two primary growth mechanisms proposed for the growth of SiO₂ particles synthesized through the Stöber approach, the monomer addition model and the controlled aggregation models. The monomer addition model is based on the assumption that the nucleation of SiO₂ nucleation occurs by exceeding the supersaturation limit of intermediate monomers and the growth of SiO₂ nuclei occurs by the addition of silicic acid monomers.²¹ The controlled aggregation model separates the stages of nucleation and growth of SiO₂

particles, where there is a fast nucleation event of SiO₂ particles then growth subsequently occurs by the collision of the SiO₂ nuclei.^{22,23} There is some disagreement on which model correctly describes the mechanism of SiO₂ particle growth and there are several studies have attempted to elucidate these details of the Stöber approach.²⁴⁻²⁷

Another approach for synthesizing colloidal amorphous SiO₂ particles is through a reverse microemulsions. The reverse microemulsion method is often preferred over the Stöber method for synthesizing SiO₂ particles that are smaller than 100 nm, since it allows for better control in the size distribution of the particles. A reverse microemulsion is defined as small water droplets, typically less than 100 nm in diameter, suspended in an oil. The mixture is thermodynamically stabilized with a surfactant and, sometimes, a cosurfactant. Ionic or nonionic surfactants can be employed to stabilize reverse microemulsion however, nonionic surfactants have traditionally been used to prevent counterion interactions.²⁸ The growth of SiO₂ particles form within the reverse micelle where hydrolyzed TEOS monomers are condensed using an acid or a base catalyst.²⁹ Due to the strong confinement, reverse micelles act as small nanoscale reaction vessels where chemical reactions can be performed.³⁰⁻³² This is particularly useful in SiO₂ nanoparticle syntheses since functional composite particles can synthesized with a diverse range of functionalities and morphological characteristics.³³ The reaction scheme for this process to form amorphous SiO₂ is shown below.³⁴





Where R is the ethyl group $-\text{C}_2\text{H}_5$.

2.4.5 The surface chemistry of silica

Since silica is used to as a composite material with colloidal nanoparticles, the surface chemistry of the silica is important for efforts to functionalize the silica surfaces. There are several different types of groups, describing the bonding of Si and O, that can form on the surface of colloidal silica particles (**Figure 5**).¹⁹ The groups are single silanols, silanediols, silanetriols, vicinal silanols, vicinal silandiol, vicinal terminals, and siloxanes. Silanol groups are formed during the condensation polymerization of $\text{Si}(\text{OH})_4$ which then polymerizes to form $\equiv \text{Si}-\text{OH}$ on the surface. Vicinal groups are bridged OH groups that are hydrogen bonded to other group types. Siloxanes are strictly Si linked together by O, or $\equiv \text{Si}-\text{O}-\text{Si} \equiv$ bridges, where the oxygen atoms lie on the surface. The hydrophilicity of colloidal silica arises from the OH groups acting as centers for molecular adsorption during interactions with species capable of forming hydrogen bonds with the OH groups. A decrease in the number of OH groups on the surface results in more hydrophobic properties.³⁵

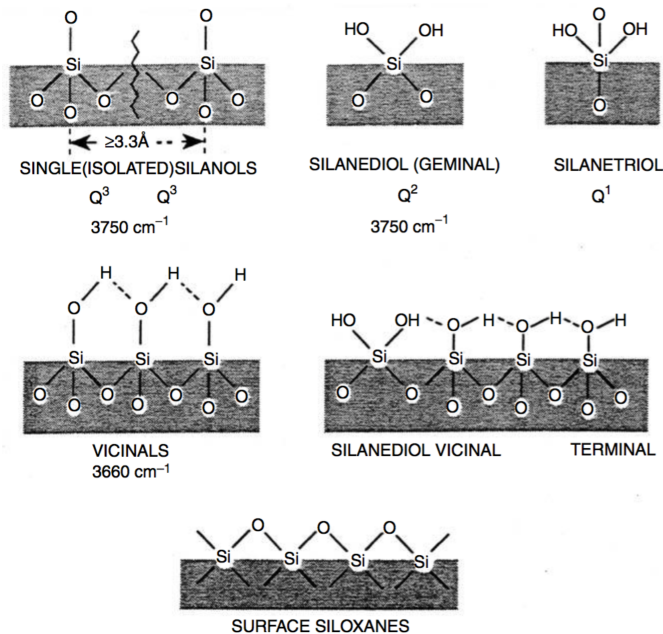


Figure 5. Types of silanol and siloxane bridges found in colloidal silica particles that includes infrared spectroscopy data of 3750 cm^{-1} and 3660 cm^{-1} that represent single and vicinal groups, respectively. Q^n is used in NMR analyses where n indicates the number of bridging oxygens bound to a single Si. Figure is from Ref. 35

Due to the nature of silicon atoms to form silanols, vacinals, and siloxane bridges, silica has become a very resourceful material that can be modified by chemical and thermal treatments.³⁶⁻³⁹ Silica is commonly modified with organic molecules through reactions with the siloxane or silanol groups. Reactions with siloxanes occur by nucleophilic substitution at the Si and reactions with the silanols occur by reacting with the hydroxyl groups. There are three main methods in which organic functional groups are attached to the silica surface (**Figure 6**).⁴⁰ This first method is through reacting an aliphatic alcohol with the silanol groups of the silica gel (**Figure 6a**). The second method is through reaction between organosilanes or organic molecules and silica surface groups (**Figure 6b**). The third method

is through the chlorination of the silica surface followed by reaction of the Si–Cl with an appropriate functional molecule/reactant (**Figure 6c**) or through the incorporation of functional groups *via* sol–gel methodology followed by postmodification, if necessary (**Figure 6d**).⁴⁰

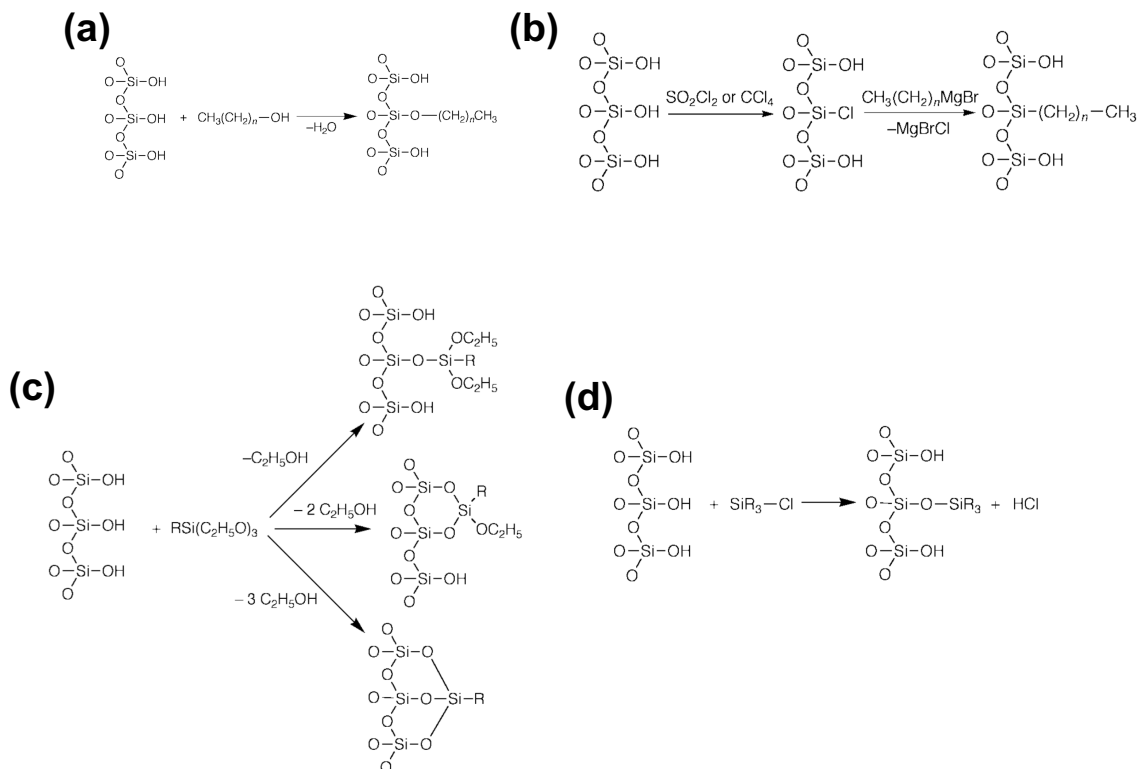


Figure 6. Silica gel modification schemes using (a) long chain aliphatic alcohols, (b) triethoxysilane, (c) chlorosilane, and (d) chlorination of silica surface and subsequent modification with Grignard reagent. Figure is from Ref. 40

The chemical and physical properties of silica make it a versatile material for combining with NPs. The use of silica is specifically discussed in chapters 4, 5, 6, 7, 8.3, and 8.5. Through the discussion of the thesis, it is evident that amorphous silica can be

incorporated into many different materials and that can be applied to a wide range of applications.

2.5 References

1. Jesus, M.; Grazu, V., *Nanobiotechnology: Inorganic Nanoparticles Vs Organic Nanoparticles*. Elsevier: 2012; Vol. 4.
2. Huang, J.; Mulfort, K. L.; Du, P.; Chen, L. X., *Journal of the American Chemical Society* **2012**, 134, (40), 16472-16475.
3. Kim, S.; Fisher, B.; Eisler, H.-J.; Bawendi, M., *Journal of the American Chemical Society* **2003**, 125, (38), 11466-11467.
4. Lifshitz, E.; Brumer, M.; Kigel, A.; Sashchiuk, A.; Bashouti, M.; Sirota, M.; Galun, E.; Burshtein, Z.; Le Quang, A. Q.; Ledoux-Rak, I.; Zyss, J., *The Journal of Physical Chemistry B* **2006**, 110, (50), 25356-25365.
5. Peng, X.; Schlamp, M. C.; Kadavanich, A. V.; Alivisatos, A. P., *Journal of the American Chemical Society* **1997**, 119, (30), 7019-7029.
6. Vasudevan, D.; Gaddam, R. R.; Trinchì, A.; Cole, I., *Journal of Alloys and Compounds* **2015**, 636, 395-404.
7. Corrias, A.; Conca, E.; Cibin, G.; Mountjoy, G.; Gianolio, D.; De Donato, F.; Manna, L.; Casula, M. F., *The Journal of Physical Chemistry C* **2015**, 119, (28), 16338-16348.
8. Carbone, L.; Nobile, C.; De Giorgi, M.; Sala, F. D.; Morello, G.; Pompa, P.; Hytch, M.; Snoeck, E.; Fiore, A.; Franchini, I. R.; Nadasan, M.; Silvestre, A. F.; Chiodo, L.; Kudera, S.; Cingolani, R.; Krahne, R.; Manna, L., *Nano Letters* **2007**, 7, (10), 2942-2950.
9. Bertoni, G.; Grillo, V.; Brescia, R.; Ke, X.; Bals, S.; Catellani, A.; Li, H.; Manna, L., *ACS Nano* **2012**, 6, (7), 6453-6461.

10. Peng, X.; Manna, L.; Yang, W.; Wickham, J.; Scher, E.; Kadavanich, A.; Alivisatos, A. P., *Nature* **2000**, 404, (6773), 59-61.
11. Talapin, D. V.; Nelson, J. H.; Shevchenko, E. V.; Aloni, S.; Sadtler, B.; Alivisatos, A. P., *Nano Letters* **2007**, 7, (10), 2951-2959.
12. Huang, J.; Kovalenko, M. V.; Talapin, D. V., *Journal of the American Chemical Society* **2010**, 132, (45), 15866-15868.
13. Chauhan, H.; Kumar, Y.; Deka, S., *Nanoscale* **2014**, 6, (17), 10347-10354.
14. Sitt, A.; Hadar, I.; Banin, U., *Nano Today* **2013**, 8, (5), 494-513.
15. She, C.; Demortière, A.; Shevchenko, E. V.; Pelton, M., *The Journal of Physical Chemistry Letters* **2011**, 2, (12), 1469-1475.
16. Hu, J.; Li, L.-s.; Yang, W.; Manna, L.; Wang, L.-w.; Alivisatos, A. P., *Science* **2001**, 292, (5524), 2060-2063.
17. Sitt, A.; Salant, A.; Menagen, G.; Banin, U., *Nano Letters* **2011**, 11, (5), 2054-2060.
18. Blatt, H.; Tracy, R.; Owens, B., *Petrology: igneous, sedimentary, and metamorphic*. Macmillan: 2006.
19. Klein, C.; Hurlbut, C. S.; Dana, J. D., *The 22nd edition of the manual of mineral science: (after James D. Dana)*. J. Wiley: 2002.
20. Stöber, W.; Fink, A.; Bohn, E., *Journal of Colloid and Interface Science* **1968**, 26, (1), 62-69.
21. Look, J.-L.; Bogush, G. H.; Zukoski, C. F., *Faraday Discussions of the Chemical Society* **1990**, 90, (0), 345-357.

22. Green, D. L.; Lin, J. S.; Lam, Y.-F.; Hu, M. Z. C.; Schaefer, D. W.; Harris, M. T., *Journal of Colloid and Interface Science* **2003**, 266, (2), 346-358.
23. Nozawa, K.; Gailhanou, H.; Raison, L.; Panizza, P.; Ushiki, H.; Sellier, E.; Delville, J. P.; Delville, M. H., *Langmuir* **2005**, 21, (4), 1516-1523.
24. Matsoukas, T.; Gulari, E., *Journal of Colloid and Interface Science* **1989**, 132, (1), 13-21.
25. Van Blaaderen, A.; Van Geest, J.; Vrij, A., *Journal of Colloid and Interface Science* **1992**, 154, (2), 481-501.
26. Lee, K.; Sathyagal, A. N.; McCormick, A. V., *Colloids and Surfaces A: Physicochemical and Engineering Aspects* **1998**, 144, (1-3), 115-125.
27. Masalov, V. M.; Sukhinina, N. S.; Kudrenko, E. A.; Emelchenko, G. A., *Nanotechnology* **2011**, 22, (27), 275718.
28. López-Quintela, M. A.; Tojo, C.; Blanco, M. C.; García Rio, L.; Leis, J. R., *Current Opinion in Colloid & Interface Science* **2004**, 9, (3-4), 264-278.
29. Wang, J.; Sugawara-Narutaki, A.; Fukao, M.; Yokoi, T.; Shimojima, A.; Okubo, T., *ACS Applied Materials & Interfaces* **2011**, 3, (5), 1538-1544.
30. Eggers, D. K.; Blanch, H. W., *Bioprocess Engineering* **1988**, 3, (2), 83-91.
31. Carvalho, C. M. L.; Cabral, J. M. S., *Biochimie* **2000**, 82, (11), 1063-1085.
32. Uskoković, V.; Drogenik, M., *Advances in Colloid and Interface Science* **2007**, 133, (1), 23-34.
33. Guerrero-Martinez, A.; Perez-Juste, J.; Liz-Marzan, L., *Advanced Materials* **2010**, 22, (11), 1182-1195.

34. Chang, C.-L.; Fogler, H. S., *Langmuir* **1997**, 13, (13), 3295-3307.
35. Bergna, H. E.; Roberts, W. O., *Colloidal silica: fundamentals and applications*. CRC Press: 2005; Vol. 131.
36. Bagwe, R. P.; Hilliard, L. R.; Tan, W., *Langmuir* **2006**, 22, (9), 4357-4362.
37. Cascarini de Torre, L. E.; Flores, E. S.; Bottani, E. J., *Langmuir* **2000**, 16, (4), 1896-1901.
38. Goworek, J.; Borówka, A.; Kusak, R., *Colloids and Surfaces A: Physicochemical and Engineering Aspects* **1999**, 157, (1-3), 127-135.
39. Maus, M.; Englehardt, H., *Journal of Chromatography A* **1986**, 371, 235-242.
40. Price, P. M.; Clark, J. H.; Macquarrie, D. J., *Journal of the Chemical Society, Dalton Transactions* **2000**, (2), 101-110.

Chapter 3: Nanoparticle Conversion Chemistry: Kirkendall Effect, Galvanic Exchange, and Anion Exchange

The following material was published in *Nanoscale* (Vol. 6, No. 21, pp. 12159-13256, 2014) as “Nanoparticle conversion chemistry: Kirkendall effect, galvanic exchange, and anion exchange” by Bryan D. Anderson and Joseph B. Tracy. Anderson’s contribution to the research included a review of published literature in the field, compiling literature, and writing the manuscript.

3.1 Motivation

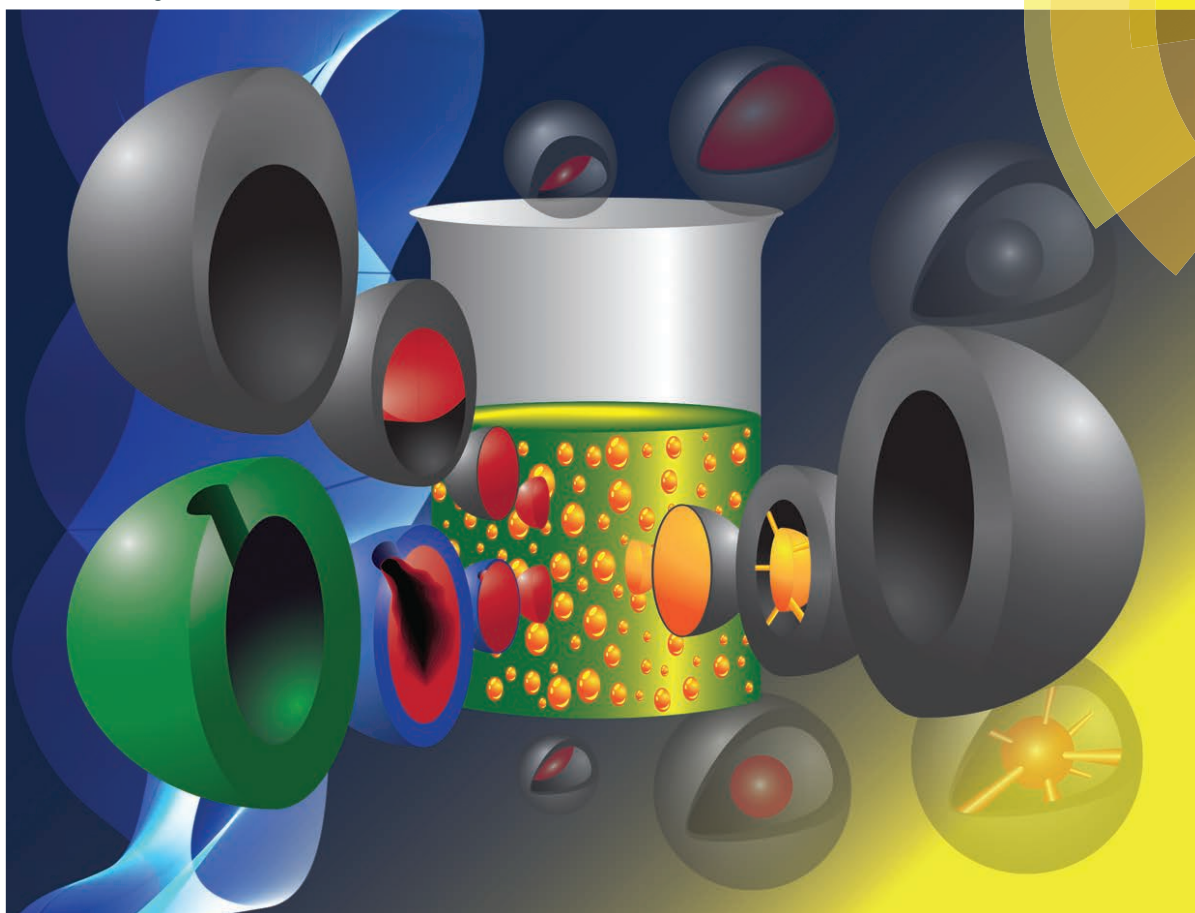
As a means to elucidate methods of obtaining NPs with tailored morphologies, chemical techniques for chemically modifying NPs was reviewed. Fabricating NPs with tailored morphologies and chemistries through conversion chemistry can have a large impacts on fundamental understandings on how NPs undergo various types of chemical reactions that can extend into many disciplines and applications. The three classes of conversion chemical reactions that are of interest are the Kirkendall effect, galvanic exchange, and anion exchange.

We reviewed methods of chemically converting template NPs through the Kirkendall effect, galvanic exchange, and anion exchange reactions. When the template NPs undergo chemical reactions, structural changes can also occur. Understanding mechanisms of the reactions, controlling the chemistry and morphology of reacting NPs, and insights for future applications were discussed in the review.

3.2 Manuscript Reprint

Nanoscale

www.rsc.org/nanoscale



ISSN 2040-3364



REVIEW ARTICLE
Bryan D. Anderson and Joseph B. Tracy
Nanoparticle conversion chemistry: Kirkendall effect, galvanic exchange,
and anion exchange



Cite this: *Nanoscale*, 2014, 6, 12195

Nanoparticle conversion chemistry: Kirkendall effect, galvanic exchange, and anion exchange

Bryan D. Anderson and Joseph B. Tracy*

Conversion chemistry is a rapidly maturing field, where chemical conversion of template nanoparticles (NPs) into new compositions is often accompanied by morphological changes, such as void formation. The principles and examples of three major classes of conversion chemical reactions are reviewed: the Kirkendall effect for metal NPs, galvanic exchange, and anion exchange, each of which can result in void formation in NPs. These reactions can be used to obtain complex structures that may not be attainable by other methods. During each kind of conversion chemical reaction, NPs undergo distinct chemical and morphological changes, and insights into the mechanisms of these reactions will allow for improved fine control and prediction of the structures of intermediates and products. Conversion of metal NPs into oxides, phosphides, sulphides, and selenides often occurs through the Kirkendall effect, where outward diffusion of metal atoms from the core is faster than inward diffusion of reactive species, resulting in void formation. In galvanic exchange reactions, metal NPs react with noble metal salts, where a redox reaction favours reduction and deposition of the noble metal (alloying) and oxidation and dissolution of the template metal (dealloying). In anion exchange reactions, addition of certain kinds of anions to solutions containing metal compound NPs drives anion exchange, which often results in significant morphological changes due to the large size of anions compared to cations. Conversion chemistry thus allows for the formation of NPs with complex compositions and structures, for which numerous applications are anticipated arising from their novel catalytic, electronic, optical, magnetic, and electrochemical properties.

Received 15th April 2014,
Accepted 7th June 2014

DOI: 10.1039/c4nr02025a

www.rsc.org/nanoscale

1. Introduction

Conversion chemistry is a versatile approach for the templated chemical conversion of nanoparticles (NPs) of one composition into another, which is often accompanied by morpho-

Department of Materials Science and Engineering, North Carolina State University, Raleigh, NC 27695, USA. E-mail: jbracy@ncsu.edu



Bryan D. Anderson

Bryan D. Anderson is a fourth year Ph.D. student in Prof. Tracy's research group in the Department of Materials Science and Engineering at North Carolina State University. After receiving his B.S. in Geology from NC State, he worked as a geologist for Unimin Corporation, where he conducted industrial mineral exploration, and for URS Corporation, where he worked on environmental remediation of contaminated soil and groundwater. In addition to nanoparticle conversion chemistry, his research interests include the synthesis and self-assembly of multifunctional nanoparticles.



Joseph B. Tracy

Joseph B. Tracy is an Associate Professor in the Department of Materials Science and Engineering at North Carolina State University. He received his B.S. in Chemistry from the University of California, Santa Barbara, and his Ph.D. from MIT in Physical Chemistry, followed by postdoctoral research at the University of North Carolina, Chapel Hill. He joined NC State in 2007, where his research interests include the synthesis, conversion chemistry, self-assembly, and applications of magnetic, metal, and semiconductor nanoparticles. In 2011, he received an NSF CAREER award.

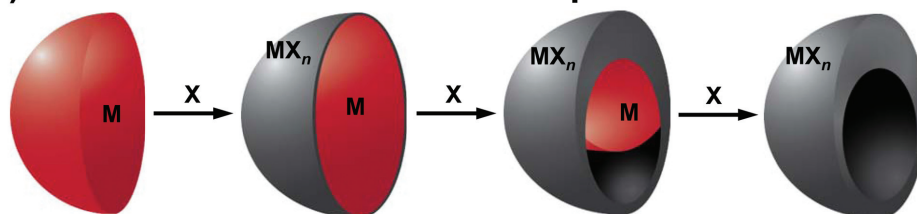
logical changes or nanostructural transformations, such as void formation.^{1–3} A common set of reaction mechanisms governing NP conversion chemistry is reviewed here. Introducing reactive species to preformed NPs drives morphological changes that are determined by the interaction between chemical reactions and diffusion of atomic species or charge carriers throughout the NP.⁴ Many conversion chemical reactions occur autocatalytically, where the reaction occurs at one or a small number of reaction sites in the NP. The number and distribution of these reaction sites is important for determining the nanostructural evolution.

This review is focused chiefly on understanding and controlling conversion chemical reactions and the accompanying morphological changes in NPs. As the field matures, emphasis will increasingly shift toward controlling conversion chemistry and optimizing it for applications. The particular classes of

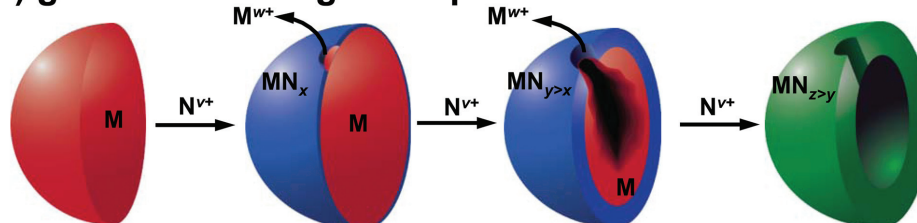
conversion chemical reactions discussed in this review include the Kirkendall effect during reactions of metal NPs, galvanic exchange, and anion exchange, which is often accompanied by the Kirkendall effect (Scheme 1).

A common type of conversion chemical reaction is alloying or compounding of atomic species through a diffusion couple, which often results in porous structures.^{5–8} Void formation can occur within NPs when species from the NP core diffuse outward more quickly than inward diffusion of reactive species, causing the reaction to occur on or near the NP surface. Void formation as a result of the imbalance of diffusion rates is a manifestation of the Kirkendall effect (Scheme 1a). While void formation is well known in metallurgy as leading to mechanical failure at interfaces between materials, void formation on the nanoscale can be well controlled due to geometrical confine-

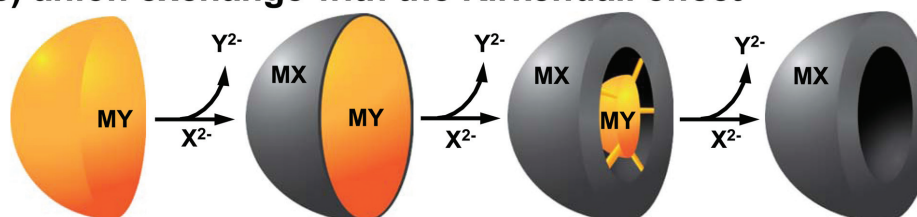
(a) Kirkendall effect for metal nanoparticles



(b) galvanic exchange with pinhole dissolution



(c) anion exchange with the Kirkendall effect



Scheme 1 Graphical depictions of examples of NP conversion chemistry. (a) Kirkendall effect: during the reaction of the metal (M) with reactive species X to form MX_n , void formation occurs. (b) Galvanic exchange: reduction of ions (N^{v+}) of a more noble metal (N) drives oxidation of a less noble metal (M), which dissolves into solution (M^{w+}) through pinholes formed in the shell. (c) Anion exchange: during the reaction of a metal compound (MY) with a reactive anion (X^{2-}), anions (Y^{2-}) are released to form MX. Void formation through the Kirkendall effect can occur when cations diffuse outward to react with the reactive anions.

ment of diffusion.^{9–12} The Kirkendall effect in nanostructures has garnered significant attention because of its frequent occurrence and the possibility to obtain uniquely tailored compositions and structures.¹³ Our review of the Kirkendall effect in metal NPs is focused on how to obtain compositional and morphological control during reactions of metal NPs.

Chemical transformation of NPs *via* galvanic exchange (also known as transmetalation) is another versatile and promising method for creating designer NPs with tailored morphologies, thereby altering their physical properties (Scheme 1b).^{14–17} Galvanic exchange is driven by the difference in reduction potentials between two metals.¹⁸ After synthesizing a nanostructure of the less noble metal, a solution containing cations of a more noble element (lower reduction potential) is added. The less noble metal NP serves as a sacrificial template, from which some portion of the metal is oxidized and transferred into solution concurrently with reduction and deposition of the more noble metal. Au, Pt, and Pd salts have often been chosen as the more noble metals.¹⁹ During galvanic exchange reactions, the structure and composition of the products are further affected by the interaction between the more and less noble metals. Initially, alloy shells usually grow on the less noble metal NP.²⁰ As galvanic exchange proceeds, dealloying may also occur, where the less noble metal is removed from the alloy. Alloying and dealloying drive morphological changes (often into hollow nanostructures, which sometimes appear as nanoframes). The final stage of dealloying can lead to breakup of the nanostructure, which is often avoided by stopping galvanic exchange reactions before completion.

In anion exchange reactions, anions in the template NPs are extracted and replaced through addition of another kind of anion. Cation exchange is a more common kind of ion exchange reaction, where the cations are replaced. The smaller ionic radius of cations than anions facilitates diffusion while conserving the morphology of the template NP.^{21,22} Partial cation and partial anion exchange can promote the fabrication of heterostructured or hybrid NPs with tailored structures and properties.^{23,24} Cation exchange has recently been extensively reviewed elsewhere and is not further discussed here. We refer the interested reader to these other review articles.^{25,26}

The size and morphology of NPs can be controlled through several mechanisms, including Ostwald ripening.^{27–30} While Ostwald ripening is not accompanied by a conversion chemical reaction (and thus is not covered here in significant detail), it can have an important role in the coalescence of voids, shape changes, and phase transformations in nanostructures.^{31,32} A recent review discusses advances in the synthesis of SnO₂, TiO₂, Fe₂O₃, Co₃O₄, and complex metal oxide hollow NPs through Ostwald ripening.²

2. Mechanisms and examples of nanoparticle oxidation

A. Introduction to oxidation

Oxidation is a common NP conversion chemical reaction.^{33–36} Oxidation of NPs involves a process similar to oxidation of

bulk metals, where a thin oxide layer forms on the metal surface, followed by simultaneous outward diffusion of metal ions through the oxide scale and inward diffusion of oxygen into the NP.^{5,37,38} Metal ions often diffuse outward more quickly than oxygen diffuses inward, which is consistent with the larger ionic radius of anions than cations. The balance of diffusion rates determines the structure of the oxidized product. More complex structures, rather than simply incorporating oxygen in the initial structure wherever the metal is present, can emerge when outward diffusion of the metal is significant.³⁹ Several theories used to describe the initial stages of oxidation of bulk metals can also be applied to explain nanostructural changes in NPs that accompany oxidation.^{40–42} The oxidation conditions and template NP composition, size, and shape give rise to different regimes of oxidation behaviour and determine the composition and structure of intermediates and the final product, such as whether voids form and how they are arranged.⁴³

If inward diffusion of oxidizing species into NPs is faster than outward diffusion of metal cations, then the NP shape (neglecting a change in volume to accommodate oxygen incorporation) is typically preserved. Such behaviour is often observed during the initial stages of oxidation. At intermediate stages of oxidation, core/shell structures are often observed, for which several examples are known.^{7,13,33,34,36,43–69} The Kirkendall effect, where outward diffusion of the metal is faster than inward diffusion of oxygen, can drive substantial morphological changes during NP oxidation (Fig. 1).

B. Cabrera–Mott (CM) theory of oxidation and formation of thin oxide films

Cabrera–Mott (CM) theory is one of the first physical rather than phenomenological models to describe diffusion of metal ions and oxygen during oxidation.⁷⁰ CM theory was initially developed to model oxidation of a flat slab of material rather than a curved NP but nevertheless provides a good description of the onset of metal NP oxidation. More recent modifications to CM theory take into account spherical NP geometries along with core and shell volume changes during oxidation.^{71,72} Auge *et al.* have also included a parameter for the influence of surface-bound stabilizing ligands for modelling oxidation of colloidal NPs.⁷³

CM theory describes the first stage of oxidation, where oxygen disassociates and adsorbs onto the surface of the metal, forming a thin metal oxide layer. Adsorption of oxygen creates surface states below the Fermi energy of the metal.⁷⁴ Electron tunnelling into the surface states results in an electric field within the oxide that lowers the activation energy for diffusion of metal cations, which then commences.⁷¹ The electric field is critical for driving migration of metal cations, which is initially fast because the electric field depends inversely on the oxide layer thickness (Scheme 2). As the oxide layer grows thicker, the electric field decreases, which reduces the rate of migration and slows further oxidation. The self-limiting nature of the CM mechanism of oxidation results in very slow oxidation of thicker films, and other oxidation mechanisms become predominant, provided the temperature is sufficiently

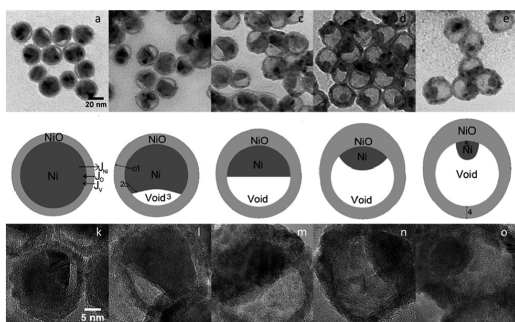
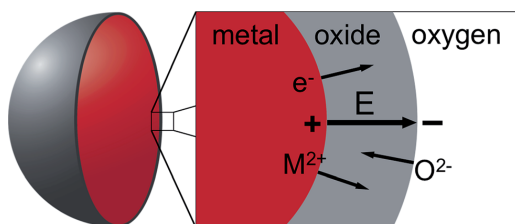


Fig. 1 TEM and corresponding graphical depictions of morphological changes through the Kirkendall effect during the oxidation of 26 nm diameter Ni NPs under ambient atmosphere at 300 °C for (a and k) 90, (b and l) 120, (c and m) 150, (d and n) 180, and (e and o) 210 min. Formation of a single void at the core/shell interface causes asymmetrical outward diffusion of Ni, resulting in a non-uniform NiO shell thickness. Reprinted with permission from ref. 43. © 2010 American Chemical Society.



Scheme 2 Graphical depiction of the initial stages of oxidation of a metal NP according to the Cabrera–Mott model, resulting in a thin metal oxide layer. An electric field generated in the metal oxide layer drives diffusion of ions and flow of electrons through the oxide layer.

high. In CM theory, electron tunnelling is rapid, and diffusion of metal cations from the metal/oxide interface to the oxide/solution or oxide/gas interface is assumed to be rate determining. CM theory without modifications is only valid for thin oxide layers (<3 nm) and relies upon several assumptions that limit its scope. For example, CM theory does not take grain boundaries into account and assumes the defect concentration remains constant throughout the entire oxidation process. More recent modifications to CM theory overcome these limitations, but the original CM theory remains useful for explaining and predicting the initial stage of NP oxidation.

C. Comparison of Cabrera–Mott theory with experiment

CM theory has been used extensively to explain low-temperature oxidation kinetics of metal NPs. Yoon *et al.*³⁶ investigated oxidation of elemental Fe NPs. Oxide shells formed non-linearly with time in air at room temperature. Understanding and controlling NP oxidation kinetics is important because physical properties (magnetic properties, in this example) depend on both the structure and composition of the iron

oxide formed.^{49,75} As expected, the magnetization decreased as the oxide thickness increased. Oxidation kinetics did not depend on the NP size; rather, oxide shells formed on different NP sizes with the same initial thickness of 2.2 nm (Fig. 2).³⁶ An earlier study reported a similar result of an initial oxide thickness of ~3 nm for oxidation of different sizes of Fe NPs under ambient conditions.⁴⁹ Therefore, the mechanism of initial oxidation does not depend on size. NPs with diameters below 8 nm were completely oxidized and usually contained a single void in the centre. Sizes larger than 10 nm, however, formed core/shell NPs containing an α -Fe core with a shell consisting of either Fe_3O_4 or $\gamma\text{-Fe}_2\text{O}_3$. In the core/shell NPs, multiple voids formed at the core/shell interface. While the oxide formation rate in Fe NPs substantially slows as the oxide shell thickness increases, the rate and extent of NP oxidation can be accelerated by raising the temperature.⁷ Oxidation of metals is thermodynamically favourable but kinetically hindered. It should be noted that $\Delta S^\circ < 0$ for oxidation, since gaseous oxygen is consumed and is the most significant contribution to entropy. Consequently, raising the temperature makes ΔG° for oxidation more positive.

Size-independent oxidation of Co NPs has also been confirmed.⁷⁶ Co NPs with diameters below 5 nm were immediately completely oxidized and reshaped into hollow shells through the Kirkendall effect. Moreover, oxidation of Co NPs under ambient atmosphere and temperature exhibits a logarithmic dependence on time, as predicted by CM theory.⁷⁶

Colloidal NPs are typically stabilized in solution by organic ligands, which can inhibit oxidation and alter the oxidation kinetics and the structure of the products. Doan *et al.* com-

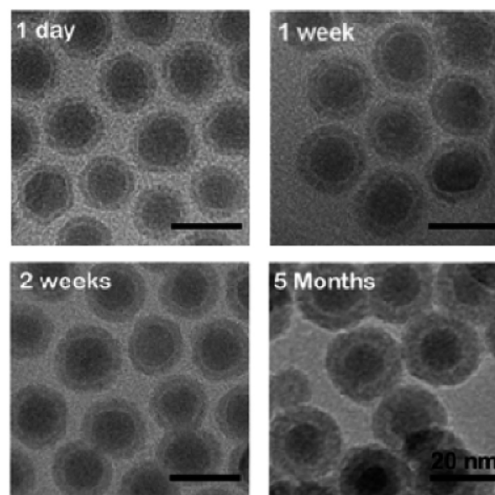


Fig. 2 TEM images showing the formation of thin oxide shells on Fe NPs in air at room temperature. After rapid formation of the initial thin oxide, the oxidation rate slows by several orders of magnitude. Reprinted with permission from ref. 36. © 2013 WILEY-VCH Verlag GmbH & Co. KGaA, Weinheim.

pared the oxidation of Co NPs stabilized by amines and carboxylic acids by measuring the oxygen consumption.⁷⁶ For tridodecylamine-stabilized Co NPs, an oxide thickness of 0.8 nm was obtained after 3000 s of oxidation. In other experiments, tridodecylamine was replaced with carboxylic acids of varying chain lengths *via* ligand exchange. The oxide shell thickness on the carboxylic acid-stabilized NPs after 3000 s of oxidation was 1.2 nm. After 6 months of exposure to atmospheric oxygen, tridodecylamine- and carboxylic acid-stabilized Co NPs formed Co/CoO core/shell and hollow CoO NPs, respectively. Promotion of oxidation by carboxylic acid ligands was attributed to carboxylate anions formed on the NP surface, which enhanced the electric field associated with oxidation through the CM mechanism and allowed for a greater flux of Co(ii). The functional group appears to have a more pronounced effect than steric effects that could restrict O₂ from reaching the NP surface, since a bulky tertiary amine would less effectively block access to the core than an unbranched carboxylic acid. It should also be noted that the TEM electron beam can drive oxidation of Co NPs into CoO, where carboxylic acid ligands are believed to serve as the source for O²⁻. Such electron-beam driven oxidation also alters the subsequent oxidation behaviour under ambient atmosphere.³⁴

NP oxidation can be problematic for air-sensitive NP core materials, where there is interest in controlling the extent of oxidation or completely avoiding it. Self-assembly of ligand-stabilized Ag and Co NPs into close-packed monolayers has been shown to inhibit oxidation.^{77–80} Yang *et al.* investigated the oxidation of Co NPs supported on TEM grids, where they compared dilute dispersions with close-packed assemblies. Dilute dispersions of Co NPs completely oxidized into hollow CoO NPs, but close-packed arrays partially oxidized into Co/CoO core/shell NPs.⁸¹ Another study demonstrated control over void formation by creating metal core/alloy shell Fe/Fe_xCr_{1-x} NPs.⁸² Upon oxidation, the NPs were transformed into Fe/M₃O₄ (M = Fe, Cr) core/shell NPs. Depending on the initial Fe_xCr_{1-x} alloy shell thickness, the Kirkendall effect was minimized or prevented. NPs with thin alloy shells, however, still formed voids.

A study by Nakamura *et al.* on the low-temperature oxidation of Cu, Al, and Pb NPs provided insights into the mechanisms of NP oxidation.⁸³ A critical diameter was observed for oxidation of Cu and Al NPs at or near room temperature. For NPs smaller than the critical diameter, a single void was formed through the Kirkendall effect in the completely oxidized product. Al NPs had a critical diameter of 8 nm, and the Al₂O₃ shell thickness was 1.5 nm. In another study by Nakamura *et al.*, Zn NPs exhibited a critical diameter of 20 nm.⁵³ The critical diameter for Cu NPs is in the range of 10–40 nm.⁵³ The Kirkendall effect was not observed during oxidation of Pb NPs, but oxidation to PbO was complete. They concluded that CM theory applies to the low-temperature oxidation of Cu, Al, and Pb NPs, while different mechanisms determine the extent of void formation during oxidation in each of type of NP.⁸³ While the initial oxidation of Cu and Al is consistent with CM theory, the slower self-diffusion of Al than Cu causes Al NPs to

more clearly demonstrate the limiting behaviour of CM theory, when the electric field is diminished as the oxide shell grows. Beyond initial oxidation and at sufficiently high temperatures, oxidation proceeds according to other diffusion mechanisms.

D. Theories for high-temperature oxidation through lattice diffusion – from bulk metals to nanoparticles

While oxidation reactions are common, the mechanisms of NP oxidation remain incompletely understood. Tunnelling and the electric field described by CM theory are only viable for thin oxide layers. Other oxidation mechanisms must be considered to properly describe the further and complete oxidation of metal NPs. Jia *et al.* found that the room-temperature oxidation kinetics of Co NPs proceeded according to a logarithmic rate expression at thicknesses, where CM theory would no longer apply.⁸⁴ While the initial stage of oxidation described by CM theory has been quantitatively compared with experiment, most comparisons for subsequent oxidation with experiment are phenomenological rather than quantitative.

Wagner theory was originally developed to describe high-temperature oxidation of bulk metals beyond the thin layers described by CM theory.⁸⁵ During oxide scale growth, Wagner theory assumes the oxide scale is dense, continuous, and conformal with the underlying metal surface. Thermodynamic equilibrium throughout the oxide layer and at the metal/oxide and oxide/oxygen interfaces is also assumed. Lattice diffusion of ions and charges across the neutral oxide layer is presumed to be the rate-limiting step, which gives a parabolic rate expression for oxide growth.^{86,87}

NP oxidation is more accurately described by several other theories and additional modifications to CM theory. Valensi–Carter's shrinking core model for isothermal high-temperature oxidation of spherical particles takes into account the spherical geometry, resulting in a more accurate rate law for oxidation.^{88–91} Fromhold and Cook have modified CM theory to arrive at a more general theory of planar thick oxide film growth using a coupled-current approach that accounts for diffusion of ions and charge carriers in the presence of large surface charges and large space charges within the oxide layer. The growth kinetics of metal oxide films can be modeled by accounting for all of the ionic and electronic diffusion currents.⁹² CM theory's single-current model represents the zero-space-charge, high electric-field limit of Fromhold and Cook's theory. Twenty years later, Fromhold developed a model for the oxidation of spherical metal NPs in the low space-charge limit using the coupled current approach for oxide thicknesses below 100 nm.⁹³ In contrast, CM theory describes formation of thin (<10 nm), planar metal oxide layers. Since NP reaction rates and activation energies depend on size and shape, Fromhold's model of nanoscale oxide formation is more accurate but also more complex than CM theory. An experimental study used Fromhold's theory and Valensi–Carter's shrinking core model to understand oxidation kinetics of Ni NPs; the activation energy for NP oxidation decreases with size.⁹⁴ More recently, other modifications of CM theory for spherical NPs have been developed.^{71–73,95}

E. Void instability: reductive transformations and high-temperature collapse

Conducting successive conversion chemical reactions on NPs can be envisioned to create complex structures. Pairing oxidation with reduction by vacuum, H_2 , or other reducing atmospheres^{62,65,66,96} allows investigations of the “reversibility” of the oxidation process with respect to the intermediate and final structures, as well as the conversion mechanism. Moreover, if sintering between NPs can be avoided during oxidation and reduction, then cyclic oxidation–reduction reactions can be performed.

Ha *et al.* demonstrated a cyclic chemical and morphological transformation between Mn_3O_4/SiO_2 core/shell NPs with small metal oxide (PtO, PdO, NiO) NPs embedded in the SiO_2 shell and hollow $MnO-SiO_2$ NPs with small embedded metal NPs (Pt, Pd, Ni), which is obtained by heating under H_2 (Fig. 3).⁹⁷ $Mn(III)$ is reduced to $Mn(II)$ and diffuses into the SiO_2 shell. Subsequent oxidation in air at elevated temperature converted the NPs back into their former structure, and the NPs were reversibly cycled between the two structures by toggling between reducing and oxidizing conditions. The use of SiO_2 shells was effective at preventing sintering among the NPs, provided that excessively high temperatures were not used.

Medford *et al.* investigated the size-dependent reduction of hollow/porous NiO NPs of several sizes with H_2 at 350 °C that had been obtained from solid Ni NPs through the Kirkendall effect.⁶⁶ The nanostructures and distribution of Ni and NiO before, during, and after reduction depend on the size of the template NPs. Small hollow NiO NPs (obtained from solid Ni NPs with diameters of 12 nm) were found to have a single Ni nucleation site inside the hollow cavity at the void/NiO interface. As reduction proceeded, Ni was deposited inside the void. The NiO shells are expected to have some porosity, which would allow H_2 to diffuse through the shells. Chenna *et al.* investigated the reduction of NiO nanoshells supported on

larger SiO_2 NPs and similarly observed the growth of single Ni grains that nucleated on the inside of the NiO nanoshells at the NiO/ SiO_2 interface.^{62,65} Medford *et al.* also studied the reduction of larger NiO NPs, for which multiple Ni grains nucleated and served as reduction sites.⁶⁶ For example, during the reduction of hollow NiO NPs formed from Ni NPs initially of diameter 24 nm, multiple Ni grains formed within the NiO shell rather than on its surface, which is a type of structure that was not obtained during the initial oxidation procedure. As reduction progressed in the larger NPs, Ni grains grew, and then Ni/NiO NPs eventually collapsed.

Sadasivan *et al.* investigated the cyclic reduction-oxidation-reduction of cube-shaped Co_3O_4 NPs with sizes of 3, 6, 11, and 29 nm.⁶⁸ During the first reduction reaction with H_2 at 500 °C, conversion into spherical Co NPs occurred. Upon subsequent oxidation, the 3 and 6 nm samples were completely oxidized into solid CoO and/or Co_3O_4 NPs, while the 11 nm sample transformed into hollow Co_3O_4 NPs. The 29 nm sample formed Co/ Co_3O_4 core/shell NPs with a shell thickness of 3 nm. Higher temperatures were required to completely convert the 29 nm sample into hollow Co_3O_4 NPs. During the second reduction step, the 11 nm NPs were reduced to form Co/ Co_3O_4 core/shell NPs, though the shell might have formed later, when the specimen was transferred into the TEM. The 29 nm hollow Co_3O_4 NPs fragmented into smaller NPs during the second reduction reaction.

Nakamura *et al.* investigated the reduction of hollow NiO and Cu_2O NPs by annealing under vacuum (5×10^{-5} Pa).⁹⁶ The voids collapsed as the reduced metal nucleated and grew. Hollow Cu_2O and NiO NPs underwent void collapse at 473 K and 623 K, respectively.

Many of the studies discussed in this section thus far have used chemical reduction to drive morphological changes in NPs, including void collapse. Voids may also shrink in volume or collapse entirely in the absence of chemical reduction if hollow or porous nanostructures are heated to sufficiently high temperatures. Nakamura *et al.* also observed void shrinkage and collapse in hollow metal oxide NPs (for oxides of Fe, Ni, and Cu) while annealing in air, which would maintain an oxidizing atmosphere.^{96,98} Void collapse is driven by vacancy diffusion to the nanostructure surface, which lowers the surface energy. The Gibbs–Thomson effect explains the mechanism of outward vacancy diffusion and void collapse in hollow NPs.^{99–102}

In the same study discussed above, Nakamura *et al.* also observed shrinkage and void collapse of hollow CuO and NiO NPs when heating under air at higher temperatures of 673 K and 923 K, respectively.⁹⁶ Hollow CuO NPs were first obtained from oxidation of hollow Cu_2O NPs at 573 K, while maintaining their morphology. High-temperature annealing and collapse of Fe_3O_4 , NiO, and CuO nanotubes under air was also reported.^{98,103} The morphologies of hollow NPs and nanowires during void collapse resembled each other, but several significant details strongly depended on the composition. During the transformation of hollow Fe_3O_4 NPs or nanowires into $\gamma-Fe_2O_3$ through annealing, multiple small voids formed within the

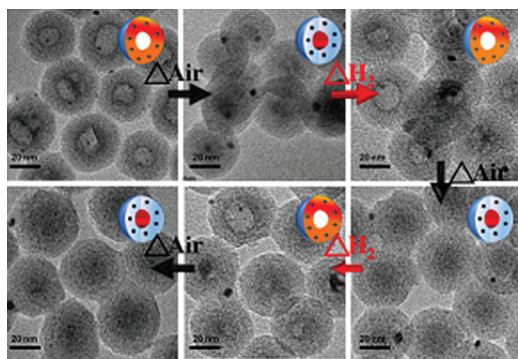


Fig. 3 Cyclic transformations of hollow $MnO-SiO_2$ NPs with small embedded Pt NPs into Mn_3O_4/SiO_2 core/shell NPs with small PtO NPs embedded in the shell by heating in air. Subsequent heating with H_2 drives the reverse reaction. Reprinted with permission from ref. 97. © 2013 American Chemical Society.

shell, which was attributed to outward diffusion of vacancies from the central void.⁹⁸

3. Nanoparticle phosphidation

Metal phosphide NPs can be obtained through reactions of metal NPs with reactive P-containing species. This section reviews recent advances in the synthesis of metal phosphide NPs.

A. Controlling void formation by adjusting reaction conditions

While a common set of principles underpins the nanostructural transformations that accompany NP conversion chemistry, precise compositional and structural control remain challenging. Conversion chemical reactions have been controlled by varying the reactant concentrations, sequence and method of addition, temperature, and time, such that phase-pure products with controlled composition and morphology have been obtained for some systems. However, obtaining precise synthetic control remains challenging, and the reaction conditions need to be optimized for each system to account for different precursor chemistries, different nucleation and growth behaviours, and different products, especially where compounds of several compositions are available for some systems. Metal phosphide NPs have novel physical properties and have also served as a useful model system for understanding conversion chemistry.

Muthuswamy *et al.* investigated the conversion of Fe NPs into phase-pure Fe₂P NPs.¹⁰⁴ Phase control was accomplished by conducting a series of reactions of Fe NPs with *n*-trioctylphosphine (TOP). TOP has been shown to serve as a P precursor for converting several kinds of metal NPs into metal phosphides.^{105,106} The phase of the Fe_xP product was controlled by adjusting the reaction times, precursor concentrations, and sequence of addition: phase-pure Fe₂P nanorods were favoured with Fe NPs were reacted with TOP for short durations. As the reaction times were extended, the Fe₂P nanorods were incompletely converted into phases further enriched in P. Void formation through the Kirkendall effect was observed during partial conversion into FeP NPs. While phase-pure Fe₂P NPs were obtained at short reaction times, phase-pure FeP NPs could not be obtained, even through prolonged heating. This inability to reach phase-pure FeP was attributed to formation of a FeP shell on the Fe₂P cores that inhibited further inward diffusion of P and outward diffusion of Fe. For synthesizing phase-pure FeP NPs, Fe NPs were combined with TOP that had been preheated to a high temperature. All of the FeP NPs produced in this manner had hollow cores, indicating formation *via* the Kirkendall effect.

Several studies have investigated control over the phase, size, and morphology of Ni_xP_y NPs. In the bulk, at least 8 phases of Ni_xP_y are known (Ni₃P, Ni₅P₂, Ni₁₂P₅, Ni₂P, Ni₅P₄, NiP, NiP₂, and NiP₃).¹⁰⁷ Chiang *et al.* and Henkes *et al.* independently showed that TOP serves as a P precursor during the

formation of Ni₂P NPs.^{108,109} While they observed void formation in some experiments and solid NPs in others, how to control the morphology was incompletely understood. Wang *et al.* later demonstrated control over the formation or absence of voids by adjusting the P:Ni precursor molar ratio but obtained mixed Ni₂P/Ni₁₂P₅ (Ni_xP_y) compositions.⁴ For P:Ni ≤ 3, Ni NPs were first obtained at 240 °C, which converted into hollow Ni_xP_y NPs at 300 °C *via* the Kirkendall effect. For P:Ni ≥ 9, amorphous Ni_xP_y NPs resulted at 240 °C, which converted into solid, crystalline Ni_xP_y NPs at 300 °C. Muthuswamy *et al.*¹¹⁰ incorporated these concepts to obtain control over the NP composition. Phase-pure Ni₁₂P₅ and Ni₂P NPs were synthesized while adjusting parameters that determined the extent or absence of void formation. Ni₂P was favoured for higher temperatures (~300–350 °C), longer reaction times, and higher concentrations of TOP (Fig. 4).¹¹⁰ The Kirkendall effect was also observed during formation of hollow Ni₂P NPs from large (~32 nm) Ni NPs. Smaller sizes (~15 nm) did not undergo void formation during conversion into Ni₂P, which might arise from differences in the crystallinity of the different sizes. Compositional control was obtained by varying the amount of oleylamine. Large amounts yielded the more Ni-rich Ni₁₂P₅ phase, but also inhibited void formation, often resulting in solid Ni₁₂P₅ NPs. Muthuswamy *et al.* have also reported that Ni NPs can be converted into Ni₂P in a stepwise fashion, with Ni₁₂P₅ NPs as the intermediate.¹¹¹

B. Effects of precursor reactivity

Precursors with different reactivity can also be used to control the morphology of the product NPs. Carencio *et al.* investigated the reaction of Ni, Cu, Fe, and Pd NPs with white phosphorous (P₄) to form metal phosphide NPs.¹¹² The higher reactivity of P₄ allowed for lower reaction temperatures, which is beneficial for large-scale production of NPs. Adjusting the reaction conditions including the meta 1:P ratio, temperature, and reaction duration resulted in different compositions, extents of crystallinity (amorphous *vs.* crystalline), and morphologies (*e.g.*, solid, hollow, core/shell, and phase segregated). Ni and Fe NP templates yielded amorphous Ni₂P and FeP NPs at the lowest reaction temperatures. At higher reaction temperatures,

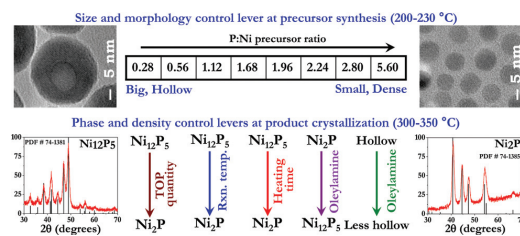


Fig. 4 Overview with inset TEM and XRD measurements of the chemical levers that control the composition, size, and morphology of Ni_xP_y NPs. Low P:Ni precursor ratios resulted in large, hollow NPs, while higher P:Ni precursor ratios gave small, solid NPs. Reprinted with permission from ref. 110. © 2011 American Chemical Society.

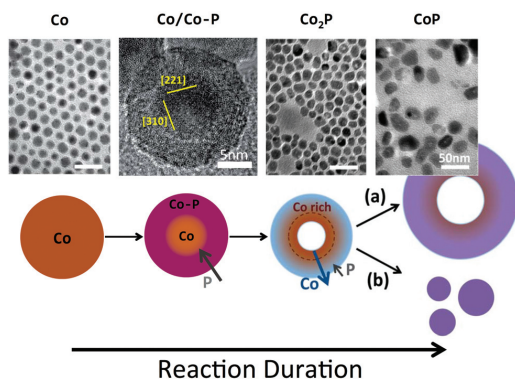


Fig. 5 Successive phosphidation reactions of Co NPs with TOP at elevated temperature. After formation of an amorphous Co-P shell, outward diffusion of Co results in hollow, crystalline Co_2P NPs. Further phosphidation into CoP can occur through two mechanisms: (a) the void size and outer diameter increase as a result of further outward diffusion of Co through the Kirkendall effect. (b) Fragmentation into smaller solid NPs, which may then grow into larger sizes through Ostwald ripening. Reprinted with permission from ref. 115. © 2011 Royal Society of Chemistry.

the NPs became crystalline and had hollow cores as a result of the Kirkendall effect. Use of P_4 to obtain Fe-rich phases of Fe_xP_y was also investigated by increasing the precursor Fe : P_4 molar ratio. Double-shelled $\text{Fe}_2\text{P}(\text{interior})/\text{Fe}_x\text{O}_y(\text{exterior})$ NPs with a central void were obtained when the ratio was increased to 16 Fe : P_4 .

C. Observation of intermediates

For some systems, a better understanding of the void formation process remains elusive, in part due to limited ability to observe intermediate stages before completion of the conversion reaction. While core/void/shell intermediates have been frequently observed for oxidation, many fewer intermediates are known during phosphidation. Ha *et al.* investigated the stepwise conversion of ϵ -Co (a metastable cubic structure commonly observed in Co NPs^{113,114}) NPs into Co_2P and then into CoP NPs by reacting ϵ -Co NPs with TOP (Fig. 5).¹¹⁵ During the conversion of ϵ -Co into Co_2P , inward diffusion of P atoms is initially faster than outward diffusion of Co. When a Co_2P shell crystallizes, however, outward diffusion of Co becomes more favourable, driving void formation. No additional voids were observed during conversion of Co_2P into CoP NPs, but the average size increased, which is suggestive of ripening. In a related study, Ha *et al.* investigated the oxidation of ϵ -Co NPs into CoO, followed by subsequent oxidation into Co_3O_4 NPs with air at 200 °C.³³ Conversion into hollow CoO NPs was complete after 30 minutes. After another 1.5 hours, CoO NPs were completely converted into Co_3O_4 NPs through outward diffusion of Co(II), resulting in enrichment in O. Both studies were accompanied by theory to better understand conversion mechanisms at the atomic scale.

4. Conversion into metal chalcogenides using Cd template nanoparticles

Hollow metal chalcogenide NPs are of interest for their optical, magnetic, and electrochemical properties.^{116–118} Precise morphological control of metal chalcogenide NPs obtained through conversion chemical reactions of metal NPs is highly desirable. Ibáñez *et al.* investigated the morphological changes that occur when large (~300 nm diameter) spherical Cd NP templates react with O_2 , elemental sulphur dissolved in *o*-dichlorobenzene (DCB:S), or with complexes of TOP and elemental sulphur, selenium, or tellurium (TOP:S, TOP:Se, and TOP:Te, respectively).¹¹⁹ The Cd template NPs were completely converted into CdO during the reaction with O_2 , but no voids formed, suggesting that oxide anions diffused more quickly than Cd(II) (Fig. 6a). In the reaction with TOP:Se (TOP:Te), CdSe(Te) formed at both the shell/solution and Cd/CdSe(Te) core/shell interfaces (Fig. 6d and e). The shell thickness and crystallinity of the products were found to depend upon the relative chalcogenide and Cd NP concentrations.

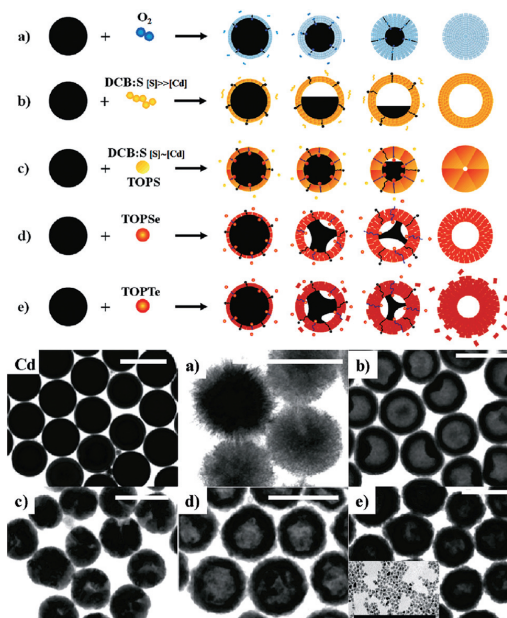


Fig. 6 Graphical representations and corresponding TEM images of the products for several conversion chemical reactions of large Cd NPs: (a) oxidation gives urchin-shaped CdO NPs, (b) a large excess of S in dichlorobenzene (DCB:S) produces hollow CdS NPs with high inner : outer radius ratios, (c) smaller amounts of DCB:S or use of TOP:S drive formation of hollow CdS NPs with low inner : outer radius ratios, (d) TOP:Se produces hollow CdSe NPs, and (e) TOP:Te produces hollow CdTe NPs, as well as (e, inset) smaller solid CdTe NPs. All scale bars are 500 nm except for (e, inset), which is 100 nm. Reprinted with permission from ref. 119. © 2011 American Chemical Society.

The amount of DCB:S allowed to react with Cd NPs was also varied. Large amounts of DCB:S (excess S) gave small crystal grain sizes and a large inner:outer radius ratio, which is close to the theoretical limit of nearly complete CdS shell growth at the shell/solution interface (Fig. 6b). Under these reaction conditions, outward Cd diffusion is much faster than inward S diffusion. The small grain size results from the fast nucleation of CdS grains at the CdS shell/solution interface. Smaller amounts of DCB:S gave reduced CdS nucleation rates, yielding larger crystal grain sizes and a small inner-to-outer radius ratio (Fig. 6c). The final structure is determined by the competition of conversion at the inner Cd/CdS core/shell interface and the outer CdS shell/solution interface. At high DCB:S concentrations, conversion occurs preferentially at the CdS shell/solution interface and is diffusion limited. At lower DCB:S concentrations, diffusion to the inner Cd/CdS core/shell interface becomes significant, and conversion is reaction limited. Hence, lower DCB:S concentrations promoted CdS growth at both the core/shell and shell/solution interfaces. The extent of void formation can also be controlled by adjusting the precursor reactivity. Hollow CdS NPs with a smaller inner diameter were also obtained when using TOP:S (Fig. 6c) in place of a small amount of DCB:S, because TOP:S is less reactive than DCB:S.

5. Morphological considerations during the Kirkendall effect

A. Core and void geometry

Formation of voids together with remaining unreacted metal cores is well known as an intermediate for conversion chemical reactions of metal NPs that proceed through the Kirkendall effect. Analysis of the intermediate core/shell NPs gives greater insight into the Kirkendall effect. The metal core is usually attached to the shell in a symmetrical manner, such as being suspended by filaments, or in an asymmetrical manner, where the metal shares a common interface with part of the shell. In some instances, however, solid NP cores can be detached from the shell and completely surrounded by void space, giving the appearance of a “yolk/shell” NP with a floating yolk or a “nanorattle.” These possible morphologies are depicted in Fig. 7. There is often insufficient information to unambiguously assign the morphology from TEM images because of resolution and contrast limits and the two-dimensional image provided by conventional TEM (unless tomography is performed). In many instances, the morphology can nevertheless be assigned with reasonable confidence.

The earliest examples of the Kirkendall effect in NPs showed several filaments connecting unreacted Co cores to the shells of CoSe or Co₉S₈ products.^{13,51} Metal atoms diffuse along these filaments toward the shell by surface diffusion.¹²⁰ In this conversion mechanism, a string of voids appears at the core/shell interface. The voids may become connected in three dimensions as they grow. As the reaction proceeds, the void space increases, and the filaments grow longer and thinner. In

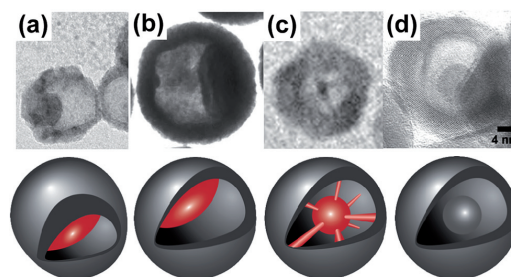


Fig. 7 (a–d) TEM images and graphical schematics below for different morphologies of NPs during or after conversion chemical reactions, where void formation occurs through the Kirkendall effect. (a) Ni/NiO core/shell NP, where the core is asymmetrically positioned on the inside of the shell, resulting in non-uniform shell thickness, (b) Cd/CdS core/shell NP, where the core is asymmetrically positioned on the inside of the uniformly thick shell, (c) Co/CoSe core/shell NP, where the core is suspended symmetrically within the void space by filaments extending from the core to the shell, and (d) Ni₂P yolk/shell NP displaying a core completely separated from the shell that floats freely within the void space. (a, b and d) reprinted with permission from ref. 43, 122 and 105. © 2010, 2008, 2007 American Chemical Society. (c) Reprinted with permission from ref. 13. © 2004 American Association for the Advancement of Science.

two-dimensional images, the filaments appear to divide the void space into multiple voids, but if they are thin filaments, they may simply penetrate through a single void space, in which the core is suspended (Fig. 7c). When the reaction is complete, the core and filaments have vanished because they have been incorporated into the shell.¹²¹ This symmetrical conversion mechanism usually gives a symmetrical NP with uniform shell thickness because the core has diffused into all parts of the shell at the same rate.

In other systems, the core may be anchored to the inside of the shell in an asymmetrical manner, where there is a single void, and the core maintains an interface adjacent to one part of the inside of the shell (Fig. 7a and b). In some systems, such asymmetric placement of the core results in non-uniform shell thickness,⁴³ but in other instances, the shell thickness can remain uniform.^{119,122} This asymmetrical conversion mechanism may be attributed to the reduction in the surface energy when a single void forms, as compared with multiple voids and filaments for the symmetrical mechanism. Therefore, systems where filaments would exhibit particularly high surface energy might instead form an asymmetrical core and void, but kinetics are also critically important; diffusion must be fast enough on the time scale of the reaction to allow for reduction of the surface energy by effectively collapsing multiple smaller voids into a larger single void. Nakamura *et al.* discussed the differences in the symmetrical oxidation of Cu NPs and the asymmetrical oxidation of Ni NPs.⁹⁶ Railsback *et al.* investigated the size-dependent oxidation of Ni NPs and showed that small sizes (9 nm) form approximately symmetrical shells, yet partially oxidized intermediates show off-centre voids.⁴³ For these small sizes, most of the reaction occurs

symmetrically through inward diffusion of oxygen before the Kirkendall effect drives asymmetrical void formation. For larger (26 nm) Ni NPs, asymmetry in the product is more prominent because the larger size causes a high proportion of the overall oxidation reaction to occur asymmetrically through the Kirkendall effect. The morphology becomes asymmetrical once a void forms at the core/shell interface. Multiple voids form at the core/shell interface in larger (96 nm) Ni NPs because one void is no longer sufficient to serve as the source for vacancy diffusion throughout the NP.

Asymmetrical void formation also accompanies sulfidation of Cd NPs and oxidation of Bi NPs. During partial sulfidation of Cd NPs, asymmetric Cd/CdS core/shell intermediates with homogeneous shell thicknesses formed.¹²² A recent study investigated oxidation of Bi NPs into Bi₂O₃, where Bi/Bi₂O₃ core/shell NP intermediates were observed using a liquid cell for TEM.⁶⁷ Two distinct behaviours were observed, which resulted in nonuniform shell thickness: (1) after the initial stage of oxidation, a single Bi core was asymmetrically positioned on the inside of the Bi₂O₃ shell. Upon complete oxidation, the part of the Bi₂O₃ shell that had been nearest to the Bi core was thicker than the section furthest from the core. (2) During oxidation, Bi exhibited liquid-like behaviour inside the void. In some NPs, the Bi core split into multiple Bi clusters. Upon complete oxidation, the Bi₂O₃ shell was locally thicker, where these Bi clusters had been deposited on the inside.

Yolk/shell structures with floating cores are the least well understood morphology obtained through the Kirkendall effect (Fig. 7d). We recently proposed that a yolk/shell structure may form from a core initially symmetrically connected to the shell through multiple filaments (Fig. 7c), if the filaments break before the core is completely consumed, causing the core to be left free-floating within the NP.¹²³ The yolk can still convert into the product, but without a clear outward diffusion path for metal atoms, inward diffusion may be favoured.¹²⁰ Henkes *et al.* reported yolk/shell structures for conversion of large Ni NPs into Ni₂P.¹⁰⁵ Sarac *et al.* have observed similar results for the conversion of Ni₃C_{1-x} NPs into Ni₁₂P₅.¹²³ In both studies, XRD measurements showed single-phase products, indicating the absence of Ni; therefore, the floating core has been converted into the same material as the shell. Henkes *et al.* obtained yolk/shell Ni₂P NPs, where some of the yolks were solid and others were hollow,¹⁰⁵ which suggests that the Kirkendall effect occurred again during the reaction of the yolk inside the outer shell.

B. Anisotropically shaped nanoparticles and assemblies

NP shape is another important lever for controlling diffusion and the Kirkendall effect. There is significant interest in anisotropically-shaped, hollow NPs. Before considering anisotropic shapes, we discuss the use of self-assembly to form chains of multifunctional magnetic metal NPs, which can be converted into nanowires. Such chaining is an example of “colloidal polymerization” of NPs, where each NP is analogous to a monomer that undergoes polymerization.^{124,125} Combining conversion chemistry with NP self-assembly will also extend

the capabilities of conversion chemistry to fabricate complex structures from NP assemblies.¹²⁶

Kim *et al.* prepared Co₃O₄ nanowires with Au inclusions by combining the Kirkendall effect with the attractive magnetic interactions of Co-based NPs.¹²⁷ Au/Co core/shell NPs, ~22 nm in diameter and capped with polystyrene, were first synthesized. The size and Co content of these NPs cause them to spontaneously assemble into chains (even in the absence of an applied magnetic field), which were then oxidized and calcined into Au/Co₃O₄ nanowires. After annealing in air at 400 °C, the chains consisted of hollow Co₃O₄ NPs containing Au within the void spaces (Fig. 8). Different morphologies were obtained from annealing in air at higher temperatures (500–700 °C), where voids collapsed or were reduced in volume, and Au NPs migrated to the surface of Co₃O₄.¹²⁸ As discussed in Section 2E, Nakamura *et al.* also observed collapse of hollow metal oxide nanostructures at high temperatures.^{96,98,103} Keng *et al.* also obtained Co₃O₄ nanowires

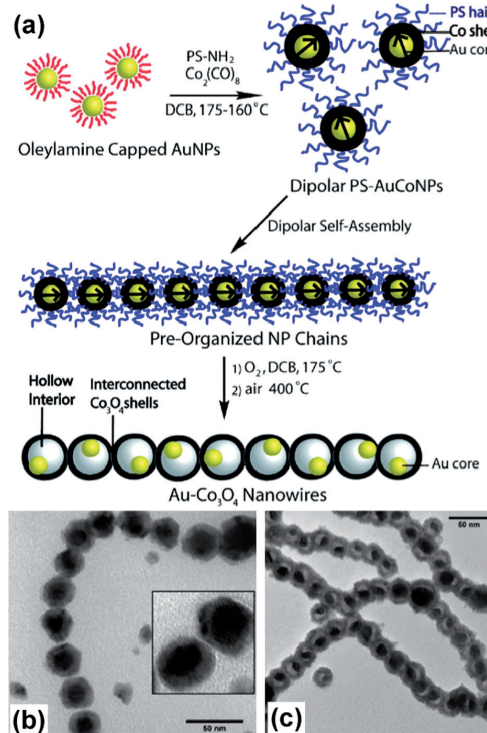


Fig. 8 (a) Graphical schematic showing the process for synthesizing Au/Co core/shell NPs, assembling them into chains, and converting them into Au/Co₃O₄ nanowires. TEM images of chained (b) Au/Co core/shell NPs and (c) Au/Co₃O₄ core/shell NPs, where Au is located asymmetrically within the voids formed during oxidation of Co into Co₃O₄. Reprinted with permission from ref. 127. © 2010 American Chemical Society.

decorated with Pt, PtO, or PtO₂ by oxidizing chains of Co NPs decorated with smaller Pt NPs.¹²⁹

De Trizio *et al.* reported two methods for synthesizing Cu₃P hexagonal nanoplatelets.¹³⁰ In one method, spherical Cu NP templates were converted into Cu₃P hexagonal nanoplatelets by adding TOP. Intermediate Cu–Cu₃P NPs were obtained, which had a Janus morphology. In the second method, Cu₃P hexagonal nanoplatelets were synthesized directly from molecular precursors, suggesting a strong energetic preference for this structure.

Ren *et al.* investigated the oxidation of Ni nanowires of diameter 80 nm.¹³¹ At 400–450 °C (low-temperature oxidation regime), oxidation was driven primarily by the electric field gradient from adsorption of oxygen on the nanowire surface, characteristic of CM theory. In the low-temperature regime, NiO nanotubes with a uniform wall thickness formed, where there were alternating regions of solid Ni and void space running along the length of the nanotube. The quasi-periodic void arrangement likely served to reduce the surface energy in comparison with the possibility of many smaller voids. This result is consistent with the oxidation of spherical Ni NPs, where single voids are commonly observed at intermediate stages of oxidation rather than multiple voids.^{43,66,96} In this low-temperature regime, oxidation became self-limiting when the tubular NiO shell reached a thickness of ~10–12 nm because the weaker electric field at greater thicknesses was insufficient to drive further oxidation. A related study on the oxidation of Cu nanowires reported a similar morphology during partial conversion into CuO nanotubes.¹³²

Subsequent heating of Ni nanowires at 650 °C (high-temperature regime) gave complete oxidation of the Ni nanowire templates, where the Ni segments within the NiO nanotubes diffused out through the sidewalls and were deposited as NiO on the outer surface.¹³¹ The sidewalls of the completely oxidized product had quasi-periodic variations in thickness and outer diameter because they were thicker in the regions that had been adjacent to the Ni segments at lower temperatures.

Conical NPs are also of interest for their distinct asymmetry. Jeong *et al.* fabricated SnO_x nanocone arrays supported on glass or Si by oxidizing Sn islands that had been deposited by electron beam evaporation.¹³³ Oxidation was conducted at elevated temperatures (~220–450 °C) under different O₂ partial pressures (*P*_{O₂}). For *P*_{O₂} ≤ 100 ppm, solid SnO_x nanocones formed. In this regime, the Sn islands melted, and oxidation occurred first at the base and then through the volume of each island, giving solid nanocone products. At *P*_{O₂} > 100 ppm, SnO_x hollow nanoislands formed. A SnO_x shell quickly formed, and oxidation was accompanied by the Kirkendall effect, resulting in hollow SnO_x nanoislands. Varying the reaction conditions can profoundly affect the structure of the products.

Sun *et al.* fabricated hollow ZnS nanoneedles *via* the Kirkendall effect driven by anion exchange (Section 8), but this study is discussed here because of the anisotropic shape of the NPs.¹³⁴ Solid ZnO nanocones were converted into hollow ZnS nanoneedles through a reaction with thioacetamide. The conical shape of the ZnO template NP imparted control over the location and shape of the void. At low reaction temperatures,

multiple voids formed at the core/shell interface, leaving several bridges of material located between the ZnO core and the ZnS shell. At higher reaction temperatures, faster diffusion allowed coalescence of the smaller voids into a larger void at the apex of the nanocones. As sulfidation proceeded, the void grew away from the apex and toward the base of the nanocone, until the final ZnS product had an open-ended base with access to the interior, thus completing conversion into a nanoneedle.

C. Void formation through selective etching of multimetal nanoparticles

There have been several reports of void formation in multimetal NPs containing Pt mixed with transition metals,¹³⁵ where the transition metal is removed through selective etching. These NPs can be used as catalysts for the oxygen reduction reaction (ORR) in proton exchange membrane fuel cells (PEMFCs). PEMFCs operate at low temperature (~70 °C) and near ambient pressure. The chemical, structural, and catalytic properties of Pt₃Co NPs incorporated into PEMFCs were recently investigated.^{136,137} In a typical setup, carbon-supported Pt and Pt₃Co NPs are loaded onto anodic and cathodic membranes, respectively. Humidified air is fed into the cathode, and dry H₂ is fed into the anode. After running a stack of PEMFCs at constant current density (typically for times longer than one month), a NP sample can be collected from the cathode for analysis. The Co portion of the NP can be leached away, leaving a Pt-enriched nanostructure behind, which may be facilitated if the Kirkendall drives outward diffusion of Co toward the NP surface. For example, monocrySTALLINE Pt₃Co NPs were converted into four different NP morphologies, hollow Pt, solid Pt, hollow Pt–Co, and Pt/Co core/shell NPs.¹³⁸ Another study reported similar behaviour, where Pt₃Ni polyhedra were converted into Pt₃Ni nanoframes with Pt-enriched surfaces.¹³⁹

The mechanism for dissolving Co or Ni has yet to be fully clarified. If Co or Ni diffuses to the NP surface prior to removal through oxidative etching, the remaining nanostructure can be significantly enriched in Pt. In this case, void formation would be driven by the Kirkendall effect. Alternatively, formation of pinholes could allow for more direct dissolution, which was recently modelled for core/shell NPs containing transition metal cores.¹⁴⁰ In this model, fluctuations of the NP shape can cause frequent opening and closing of pinholes in the Pt-rich shell, which allows for reactive species to penetrate into and to etch the NP core from within. Additional studies are needed to further discern the mechanism of Co or Ni removal. For example, more detailed observations of intermediate stages of void formation and compositional changes in the Pt-rich shell may help to determine the mechanism.¹⁴¹

6. Void formation through solid-state diffusion couples

While the Kirkendall effect has commonly been observed for reactions of metal NPs with non-metals, reactive metals can

also react with metal NPs. Jana *et al.* reported formation of hollow intermetallic NiZn_x NPs through the reaction of Ni NPs with diethylzinc at 250 °C.¹⁴² Deposition of Zn drove outward diffusion of Ni, forming NiZn_x. Galvanic exchange (Section 7) was ruled out as a possible conversion mechanism.

Anumol *et al.* conducted *in situ* TEM studies of the formation of hollow intermetallic PtBi NPs.¹⁴³ A solution containing H₂PtCl₆ and Bi(acetate)₃ was microwave heated at 100 °C. Initially, small Pt NPs grew and formed larger aggregates (Fig. 9b). Bi₂O₃ sheets formed and encapsulated the aggregates of Pt NPs (Fig. 9c). Small Bi NPs formed within the Bi₂O₃ sheets (Fig. 9d). Pt then diffused outward, resulting in hollow or porous PtBi NPs (Fig. 9e). These results were attributed to outward diffusion of Pt driven by the high surface energy of the small Pt NPs within the aggregates. The Kirkendall effect was not suspected because Pt has slower self-diffusion than Bi, though the diffusion rates of Pt and Bi in PtBi were not discussed.

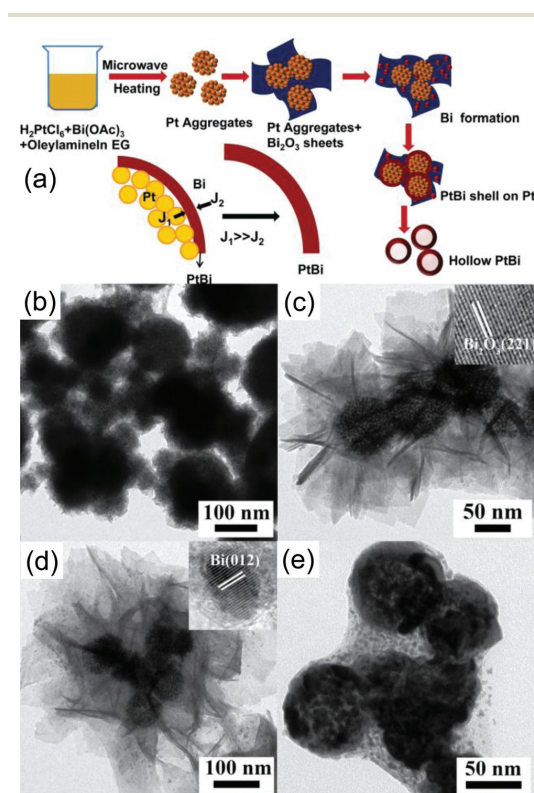


Fig. 9 (a) Graphical schematic depicting the stepwise formation of hollow PtBi NPs and TEM images showing (b) aggregates of Pt NPs, (c) Bi₂O₃ sheets surrounding the Pt NP aggregates, (d) Bi NPs formed within the Bi₂O₃ sheets, and (e) hollow or porous PtBi NPs. Reprinted with permission from ref. 143. © 2013 WILEY-VCH Verlag GmbH & Co. KGaA, Weinheim.

7. Recent advances in galvanic exchange reactions

Galvanic exchange reactions are commonly employed for obtaining NPs with complex morphologies, particularly for hollow nanostructures of controlled compositions and porosity. This section is focused on the most recent developments and understanding in controlling galvanic exchange reactions. We also direct the reader to a recent review on galvanic exchange.¹⁴⁴

Galvanic exchange reactions rely on the different reduction potentials of two elemental metals, which combine to give a favourable redox reaction. Atoms of a more easily oxidized metal (having a lower reduction potential) in the template NP oxidize and dissolve into solution, thus sacrificing the template NP (Scheme 1b). Ions of a more noble metal (having a higher reduction potential) are simultaneously reduced onto the template NP. Galvanic exchange reactions begin with deposition of the more noble metal and an alloying process, where it is alloyed into the template NPs. As deposition and alloying of the more noble metal proceeds, dissolution of the less noble metal can drive the pinhole formation. Pinholes serve as sites, where template metal atoms oxidize and dissolve into solution. Electron tunnelling allows pinholes to form in the locations where they are most stable; the pinholes do not have to form adjacent to where the more noble metal is reduced and deposited onto the NP. The resulting cavity expands toward the centre of the NP, causing dissolution from the inside out. Dealloying becomes the predominant process as the reaction continues, which is exemplified by selective oxidation and dissolution of the template metal. Dealloying can result in fragmentation, collapse, or breakup of the converted NP shell or frame.^{145,146} In order to avoid the destructive effects of dealloying, galvanic exchange reactions often are not run to completion. Enrichment of the more noble metal through galvanic exchange drives both alloying and dealloying; the distinction is that alloying describes initial formation of pinholes and larger voids, while dealloying is a more local effect, where the remaining less noble metal atoms are removed.

Since noble metals have high reduction potentials, galvanic exchange reactions are often conducted using noble metal salts, where common products are Au, Pd, and Pt. Ag nanostructures have often been used as sacrificial templates for galvanic exchange reactions, and Cu, Al, Ni, and Co have also been demonstrated as template materials.^{147–151} Structures commonly obtained through galvanic exchange include NPs, nanocages, nanorods, nanotubes, nanorattles, nanoframes, and nanobowls.^{14,19,152–159}

A. Controlling the final morphology of galvanic exchange products

The morphology of galvanic exchange products depends on the size and shape of the template NPs and can also be controlled by adjusting the reaction conditions. Galvanic exchange reactions are often conducted in aqueous solutions. Zhang *et al.* conducted a series of galvanic exchange reactions on Ag

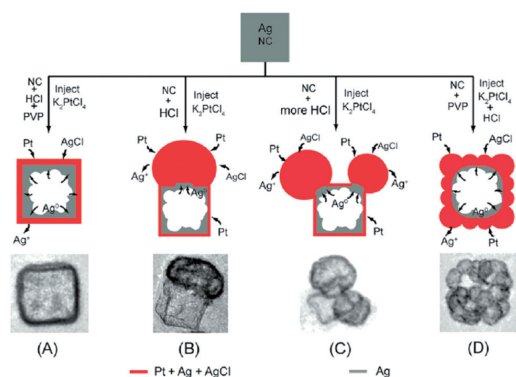


Fig. 10 Graphical schematic and TEM images for galvanic exchange reactions of Ag NPs with K_2PtCl_4 in the presence of HCl under different reaction conditions, resulting in (a) nanoboxes, (b) heterodimers, (c) multimers, and (d) popcorn-shaped NPs. Reprinted with permission from ref. 160. © 2012 American Chemical Society.

nanocubes to form PtAg bimetallic NPs of various morphologies through reactions with K_2PtCl_4 (Fig. 10).¹⁶⁰ Pt was deposited onto the surfaces of Ag nanocubes while Ag^+ ions formed $AgCl_{(s)}$. HCl and polyvinylpyrrolidone (PVP) were also added to impart morphological control over the PtAg products. HCl regulated the reaction kinetics by facilitating precipitation of $AgCl_{(s)}$ onto the NP surface, which served as a nucleation site for deposition of Pt. At low HCl concentrations, $AgCl_{(s)}$ was limited to one nucleation site (typically one of the corners or sides of the Ag nanocubes). At higher HCl concentrations, $AgCl_{(s)}$ formed more quickly and at multiple sites. In work by González *et al.*, addition of ascorbic acid was shown to prevent $AgCl$ deposition and allowed access to another reaction regime, where sequential galvanic exchange and the Kirkendall effect yielded hollow AgAu NPs with double-walled and other complex morphologies.¹⁶¹

AgAu is a common system for galvanic exchange, where solid Ag NPs are converted into hollow or cage-like AgAu alloy NPs, whose morphology is dictated by the shape of the Ag template NPs. Chien *et al.* have performed a subsequent ripening step on hollow AgAu alloy NPs to fill the void spaces while preserving the overall shape, thus allowing conversion of Ag NPs of various shapes (*e.g.*, nanoplates, nanodecahedrons, nanorods, nanoprisms, nanospheres, and thin films of thickness <10 nm– 5 μ m) into solid Au NPs of the same shape as the Ag template NP.¹⁶² Use of ascorbic acid (AA) and cetyltrimethylammonium bromide (CTAB) in conjunction with $HAuCl_4$ is necessary to preserve the morphology of the initial Ag template NP. Complexation of CTAB with Au(III) is thought to mediate the reduction rate, imparting kinetic control over Au deposition into the hollowed AgAu NPs. AA controls deposition of Au; as a mild reducing reagent, it may provide an alternative route for reduction to galvanic exchange.¹⁶³

Pradhan *et al.* synthesized highly branched Au nanoflowers resembling carnations, which have sharp tips created through

galvanic exchange.¹⁶⁴ Galvanic exchange was performed on Cu NPs embedded in negatively-charged polystyrene beads, where formation of sharp Au tips rather than flat layers was attributed to a polarization effect between $Cu(0)$ and $AuCl_4^-$ that directed deposition into tips. Such sharp Au tips are of special interest for surface enhanced Raman scattering (SERS).¹⁶⁵

B. Galvanic exchange reactions in organic solvents

Karvianto *et al.* investigated the size dependence of galvanic exchange of Ag NPs in solutions of octadecene, oleylamine, and toluene through addition of $HAuCl_4$.¹⁶⁶ Larger (~ 43 nm) Ag NPs converted into hollow AgAu alloy NPs, and smaller (~ 20 nm) Ag NPs first formed hollow AgAu alloy NPs, followed by dealloying and void collapse. Octadecene and oleylamine were thought to sterically hinder diffusion of $HAuCl_4$ to the surface of the template NPs, resulting in formation of hollow AgAu alloy NPs, whose shell thickness was proportional to the concentration of $HAuCl_4$. After nearly complete oxidation of Ag with $HAuCl_4$, oleylamine likely reduces $HAuCl_4$, driving deposition of Au and alloying into the NPs as the $HAuCl_4$ concentration is increased. Therefore, to the extent that oleylamine drives reduction of $HAuCl_4$, dealloying of Ag^+ into solution would also be suppressed. Oleylamine may also dissolve $AgCl_{(s)}$, preventing its deposition onto the NP surface. The smaller Ag NPs shrank in size during galvanic exchange in oleylamine, but the larger NPs grew because oleylamine also drove reduction of Au^+ and its deposition onto the NPs. This example highlights the significance of size in galvanic exchange and reduction reactions.

More recently, Polavarapu and Liz-Marzán developed a method for synthesizing Ag nanocubes and converting them into AgAu nanocages in *o*-dichlorobenzene/toluene mixtures by adding $HAuCl_4$ and using oleylamine as a ligand and reducing agent.¹⁶⁷ Since oleylamine can serve as a reducing agent, Au can also be deposited onto Ag NPs¹⁶⁸ or Ag onto Au NPs¹⁶⁹ by reduction rather than galvanic exchange, giving AgAu alloy NPs after annealing.

The crystallinity and morphology of galvanic exchange products are often determined by the crystallinity of the template NPs.^{20,170} Therefore, levers that control the crystallinity and morphology of the template NPs (such as solvents, ligands, reagent concentrations, and temperature) can be critically important for determining the outcome of galvanic exchange reactions.^{171,172}

C. Templates of different compositions

Reactions of Ag template NPs with Au or Pt salts for galvanic exchange reactions have been popular due to the ability to readily obtain Ag NPs of different sizes and shapes. The nobility of Au and Pt also provides significant thermodynamic driving force for galvanic exchange reactions. This section discusses other kinds of template NPs and metal salts that have been employed in galvanic exchange reactions.

Niu *et al.* investigated galvanic replacement of highly reactive Mg and Zn template NPs with Ag^+ , $AuCl_4^-$, Cu^{2+} , and Sn^{2+} oxidants to form porous Ag, Au, Cu, and Sn NPs.¹⁷³ Special measures are required to prevent or control oxidation of such

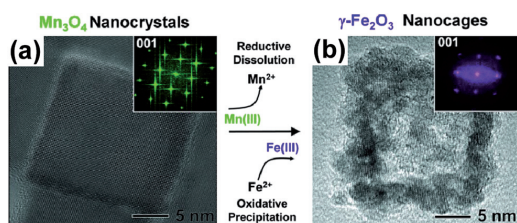


Fig. 11 TEM images showing galvanic exchange in oxide NPs: (a) starting Mn_3O_4 nanocubes and (b) the $\gamma\text{-Fe}_2\text{O}_3$ nanocage product. Reprinted with permission from ref. 181. © 2013 American Association for the Advancement of Science.

reactive template NPs. Spherical Al NPs have been shown to serve as templates for galvanic exchange reactions forming Co, In, Fe, Au, Ag, Cu, Pt, Pd, and Pb porous nanostructures.^{150,151} Cu NPs have also been used as template NPs in galvanic exchange reactions. Jin *et al.* investigated the galvanic conversion of Pd/Cu core/shell nanocubes into Pd/ $\text{M}_x\text{Cu}_{1-x}$ ($\text{M} = \text{Au}$, Pd, and Pt) yolk/shell nanocages.^{174,175} Cu nanocubes and nanowires have also been converted into hollow $\text{Au}_x\text{Cu}_{1-x}$ nanocubes and nanotubes with porous sidewalls, respectively.¹⁷⁶ Mohl *et al.* converted Cu nanowires into CuPd and CuPt bimetallic nanotubes through reactions with Pd and Pt salts.¹⁵⁷ Other template materials include Ni and Co NPs, which can be converted into hollow noble metal nanorods or NPs.^{177–180}

Oh *et al.* recently reported galvanic exchange reactions on Mn_3O_4 nanocubes using $\text{Fe}(\text{ClO}_4)_2$.¹⁸¹ $\text{Fe}(\text{II})$ oxidized to $\text{Fe}(\text{III})$ and was deposited onto the Mn_3O_4 nanocubes as $\gamma\text{-Fe}_2\text{O}_3$. Meanwhile, $\text{Mn}(\text{III})$ in Mn_3O_4 simultaneously dissolved into solution as it was reduced to Mn^{2+} , yielding $\gamma\text{-Fe}_2\text{O}_3$ nanocages (Fig. 11). The Kirkendall effect and cation exchange were ruled out as possible conversion mechanisms because the reaction was conducted at a relatively low temperature (90 °C), at which diffusion of Mn and Fe would be slow. At low $\text{Fe}(\text{ClO}_4)_2$ concentrations, the Mn_3O_4 core partially dissolved, and a hole began to form in the centre of the solid Mn_3O_4 NP. At higher $\text{Fe}(\text{ClO}_4)_2$ concentrations, reductive dissolution of Mn_3O_4 continued from the interior of the NP, and $\gamma\text{-Fe}_2\text{O}_3$ was deposited first onto the exterior and then inside of the template nanocubes, forming nanocages. This method allows for nearly complete conversion of solid Mn_3O_4 NPs into hollow $\gamma\text{-Fe}_2\text{O}_3$ NPs. In the same study, galvanic replacement reactions of Co_3O_4 and Mn_3O_4 nanocubes with SnCl_2 produced hollow or porous $\text{Co}_3\text{O}_4/\text{SnO}_2$ and $\text{Mn}_3\text{O}_4/\text{SnO}_2$ nanocages, respectively.

8. Anion exchange

Anion exchange is a growing subfield of conversion chemistry, where anions within multicomponent NPs are exchanged (Scheme 1c). During anion exchange, NPs often undergo morphological changes through the Kirkendall effect. Anions generally diffuse more slowly than cations due to the larger size of

anions. Slow anion diffusion often requires longer reaction times and higher temperatures than cation exchange. The slow reaction kinetics of anion exchange can be advantageous for obtaining control over reaction intermediates with partial anion exchange.¹⁸² In cation exchange, the smaller cations can often diffuse readily through the template NP, which preserves the anion sublattice. Consequently, cation exchange is often templated by the anion sublattice, which leaves the NP morphology unchanged. During anion exchange, however, diffusion of cations is often promoted, thereby disrupting the cation sublattice and causing major morphological changes. Cation exchange has recently been comprehensively reviewed elsewhere.^{26,183} Therefore, anion exchange is reviewed here.

In principle, a thermodynamic framework can be constructed for anion exchange that is similar to cation exchange, where the Gibbs free energy for cation exchange reactions is determined by the Gibbs free energies of formation for the compounds and the reduction potentials of the cations.²⁵ Adapting this framework to anion exchange is challenging, because the incoming anions are usually obtained through decomposition or activation of molecular precursors, and the outgoing anions often undergo further reactions, such as O^{2-} into OH^- . Therefore, the source of incoming anions and the successive reactions of outgoing ions are important for determining thermodynamic spontaneity. The law of mass action may also be used to drive reactions forward that would not be favourable in their standard states by increasing the concentration of some reagents, as is known for cation exchange.¹⁸⁴ For example, metal oxides generally have more negative Gibbs free energies of formation than the corresponding sulphides,⁴¹ but reactions associated with the anions and the concentrations can tip the energy balance to make sulfidation of oxides favourable.^{185–188} Indeed, metal oxides are attractive templates for anion exchange reactions due to their stability (as compared with reduced metals, which are susceptible to oxidation), provided that they are not too stable to undergo anion exchange. There are also examples, however, of metal oxides failing to undergo anion exchange.^{109,187,189}

Park *et al.* reported anion exchange of solid, monocrystalline ZnO NPs into hollow, monocrystalline ZnS NPs.⁶ In the case of partial anion exchange, hollow ZnO/ZnS core/shell NPs were obtained. ZnO bridges connected the ZnO core to the ZnS shell, while maintaining an epitaxial interface, despite large lattice mismatch (Fig. 12). Huang *et al.* also observed epitaxial growth of ZnS on monocrystalline ZnO nanorod arrays.¹⁹⁰ The hexagonal cross-section of the ZnO nanorods was preserved, with minor warping, to produce monocrystalline ZnS nanorods. In another study, addition of ammonium sulfide ($(\text{NH}_4)_2\text{S}$) to hollow CoO NPs at 70 °C drove formation of hollow, amorphous Co-S NPs.¹⁹¹ The high reactivity of $(\text{NH}_4)_2\text{S}$ allowed for low-temperature anion exchange. Subsequent annealing at 200 °C drove formation of hollow, polycrystalline Co_3S_4 NPs with larger void spaces, indicating further outward diffusion of Co.

Anion exchange has also been demonstrated in Sn-based nanostructures. Cai *et al.* performed a stepwise reaction, successively transforming Zn_2SnO_4 nanooctahedra into SnO_2 and

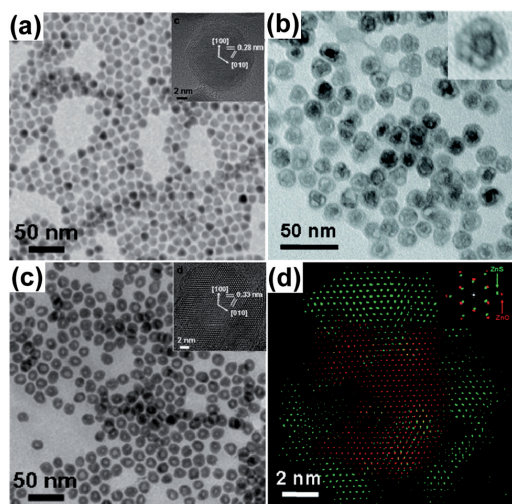


Fig. 12 TEM images acquired at different stages of anion exchange of ZnO NPs with hexamethyldisilathiane, resulting in ZnS NPs: (a) solid ZnO NPs with HRTEM inset, (b) partial anion exchange products, ZnO/ZnS core/shell NPs with prominent voids formed through the Kirkendall effect, and (c) hollow ZnS NPs obtained after complete anion exchange with HRTEM inset. (d) Reconstructed image from fast Fourier transform (FFT) spots showing heteroepitaxial growth of ZnS onto ZnO during partial anion exchange. Alignment of the spots in the inset FFT confirms epitaxy. Reprinted with permission from ref. 6. © 2009 American Chemical Society.

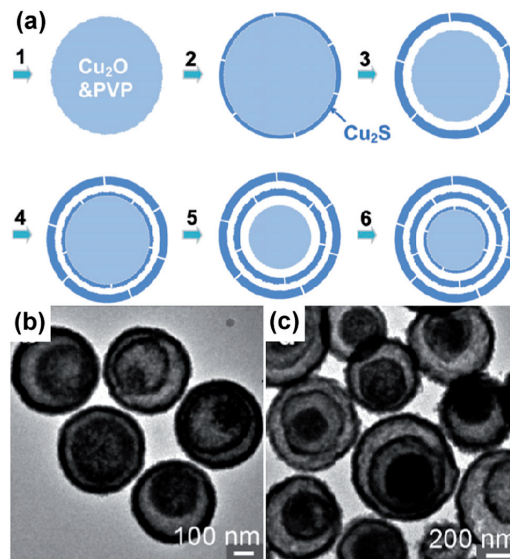


Fig. 13 (a) Graphical schematic depicting stepwise formation of multi-shelled Cu_2S hollow NPs through anion exchange at 220 °C. TEM images of (b) double-shelled NPs and (c) a mixture of double- and triple-shelled NPs. Reprinted with permission from ref. 188. © 2012 WILEY-VCH Verlag GmbH & Co. KGaA, Weinheim.

then into SnS_2 using ethylenediaminetetraacetic acid to extract Zn^{2+} and thioacetamide as a sulphur precursor.¹⁹² Sines *et al.* reported anion exchange reactions in the conversion of monocrystalline SnSe nanosheets into SnTe .¹⁹³ SnTe grew epitaxially on the SnSe nanosheets, accompanied by void formation. The porous product consisted of a pattern of SnTe nanocubes and nanobars with specific crystal orientations separated by void space. Anion exchange has also been demonstrated in the conversion of nanosheets of Co_3O_4 into CoS , NiO into NiS , and WO_3 into WS_2 .^{194,195}

The examples discussed thus far have involved anion exchange of inorganic template nanostructures into metal compounds. There is also interest in using organic–inorganic hybrid nanomaterials as starting materials for anion exchange reactions. For example, Xiong *et al.* conducted anion exchange on solid $\text{Cu}_2\text{O}/\text{PVP}$ (PVP = polyvinylpyrrolidone) hybrid NPs (PVP NPs containing crystallites of Cu_2O) through a reaction with thiourea, converting them into hollow, concentric multi-shelled Cu_2S NPs.¹⁸⁸ PVP slowed diffusion of thiourea to the Cu_2O NP surface and allowed outward diffusion of Cu to drive formation of a Cu_2S shell surrounding the hybrid core. Formation of multiple Cu_2S shells was attributed to densification of Cu_2S during the anion exchange reaction (Fig. 13). Multi-shelled Cu_2S NPs were synthesized with control over the number and thickness of the Cu_2S shells by adjusting the reaction conditions, precursor concentrations, and capping agents.

Organic–inorganic templates containing organic rather than elemental metal cations may be particularly suitable for anion exchange because the larger size of organic cations may facilitate anion diffusion. Two studies reported anion exchange of $(\text{Fe}_{18}\text{S}_{25})(\text{TETAH})_{14}$ (TETAH = protonated triethylenetetramine) layered nanoribbons, sheets of $\text{Fe}_{18}\text{S}_{25}$ separated by TETAH.^{196,197} $(\text{Fe}_{18}\text{S}_{25})(\text{TETAH})_{14}$ thermally decomposes into Fe_{7-8} nanowires under an argon atmosphere due to desulfurization and loss of TETAH.¹⁹⁶ Thermal decomposition in air resulted in porous $\alpha\text{-Fe}_2\text{O}_3$ nanorods.¹⁹⁶ TOP has been demonstrated to extract Se and S from metal chalcogenide NPs by forming TOP:Se and TOP:S complexes.¹⁹⁸ TOP can also release P and drive phosphidation, as described in Section 3. The reaction of $(\text{Fe}_{18}\text{S}_{25})(\text{TETAH})_{14}$ nanosheets with TOP yielded porous FeP nanosheets.¹⁹⁷ The porosity of the FeP nanosheets was attributed to release of stress from lattice mismatch and dissolution of TETAH rather than the Kirkendall effect. $\text{MoO}_3\text{-EDA}$ (EDA = ethylenediamine) nanowires have been reported to undergo anion exchange with L-cysteine to form hierarchical nanosheet-based MoS_2 nanotubes, where the nanotube walls were composed of MoS_2 nanosheets.¹⁹⁹ Elevated reaction temperatures drove dissolution of EDA and decomposition of L-cysteine, which simultaneously donated S^{2-} and consumed O^{2-} .

Anion exchange accompanied by the Kirkendall effect has been observed in several rare-earth-based NPs, where the large cation size may help facilitate anion exchange. Rare-earth-based NPs exhibit unique optical and magnetic properties, which are appealing to combine with hollow

morphologies.^{200–208} Zhang *et al.* reported the Kirkendall effect during anion exchange reactions of solid Y_2O_3 NPs with NaF and HF into hollow $\alpha\text{-NaYF}_4$.²⁰⁹ Hollow LaF_3 , LaCO_3F , and GdF_3 NPs have also been obtained through anion exchange.^{210,211} Hollow GdPO_4 NPs were synthesized through anion exchange of solid Gd(OH)CO_3 NPs with $\text{NH}_4\text{H}_2\text{PO}_4$, which served as the PO_4^{3-} precursor.^{212,213} Reactions of Y(OH)CO_3 and Gd(OH)CO_3 NPs with NH_4VO_3 gave hollow YVO_4 and GdVO_4 NPs.^{203,214} Hollow $\text{Yb(OH)CO}_3/\text{YbPO}_4$ core/shell NPs were also synthesized from solid Yb(OH)CO_3 template NPs and $\text{NH}_4\text{H}_2\text{PO}_4$.²⁰⁰ Some general trends should be noted about anion exchange reactions on rare-earth-based template NPs: The product NPs typically have an urchin-like morphology, where the NP surface is rough. Conversion intermediates usually have symmetrical core/shell structures, where the core is suspended by filaments that serve as diffusion pathways to consume the core (Section 5).

While most studies of anion exchange have utilized metal oxide, organic–inorganic hybrid, or rare-earth-based template NPs, anion exchange of metal chalcogenide semiconductor NPs has also been reported. For example, partial anion exchange of spherical wurtzite (w)-CdS NPs has been demonstrated. Phase-segregated w-CdS/zb-CdTe heterodimers (zb = zinc blende) formed through a reaction with TOP:Te.¹⁸² Epitaxial growth of zb-CdTe from w-CdS NPs coupled with type-II band alignment allows for oriented separation and transfer of charge carriers in the heterodimer during photoexcitation.²¹⁵ Minimal anion exchange occurred, however, when TOP:Se was added to CdS NPs at elevated temperature, which was attributed to the stronger affinity of TOP for Se than Te.¹⁸²

9. Selective conversion chemical reactions in multicomponent nanoparticles

NPs containing multiple chemically distinct domains can undergo selective conversion chemical reactions, where only one or some of the domains react with a particular reagent. Such selective conversion reactions can be used to tailor the composition and morphology of heterostructured NPs. For example, when noble metal/transition metal core/shell NPs undergo the Kirkendall effect, voids form at the noble metal/transition metal compound interface. In the seminal work by Yin *et al.* on the Kirkendall effect in NPs, Pt/Co core/shell NPs were oxidized into Pt/CoO core/shell NPs.¹³ The Pt cores retained their catalytic activity for ethylene hydrogenation reactions, which indicated that the CoO shell was sufficiently porous to allow transport of the reactants and products. In another study, elemental Fe was deposited onto Au NPs, which were oxidized to form Au/iron oxide core/shell NPs.²¹⁶ FePt/Co core/shell NPs have also been converted into FePt/CoS₂ core/shell NPs by adding elemental sulphur.²¹⁷

Multistep synthesis of colloidal NPs is conceptually analogous to total synthesis of complex molecules from simple

building blocks, where a vast toolbox of reactions can give complex structures.²¹⁸ Buck *et al.* have outlined a total synthesis approach for constructing heterostructured NPs.²¹⁹ For example, heterotrimers were formed by crosslinking two kinds of NPs with a third bridging material, while heterotetramers were obtained from heterogeneous nucleation and growth of an additional compositionally distinct domain onto heterotrimers. They also reported sulphur-mediated formation of hetero-oligomers through selective coupling of Au domains between pairs of Au–Pt–Fe₃O₄ heterotrimers.

Hill *et al.* deposited Co onto the tips of Pt-tipped CdSe/CdS core/shell quantum dot nanorods (QDNRs) through a multi-step synthesis.²²⁰ Co NP growth at the tips of QDNRs was assisted by Pt nuclei that had been deposited on the tips in a previous step. Bubbling O₂ through the solution at elevated temperature allowed for selective oxidation of Co, resulting in hollow CoO NPs through the Kirkendall effect, while leaving the Pt, CdSe, and CdS domains of the heterostructured NP unconverted.

Bradley *et al.* investigated conversion chemical reactions of Pt–Fe₃O₄ heterodimer NPs with Pb(acac)₂ (acac = acetylacetonate) and Sn(acac)₂.²²¹ Both metal salts selectively converted the Pt domain into intermetallic PtPb or a Pt₃Sn alloy, yielding PtPb–Fe₃O₄ or Pt₃Sn–Fe₃O₄ heterodimer NPs. Furthermore, PtPb–Fe₃O₄ NPs assembled into flowerlike structures through an aging process, where the surfaces of the PtPb domains fused together with the Fe₃O₄ lobes extending outward. Although the conversion mechanism in this study appears to be selective deposition and reaction with the Pt domain rather than galvanic exchange (due to the nobility of Pt), this study demonstrates the potential for performing such selective reactions.

In another demonstration of site-selective conversion chemistry, Read *et al.* deposited Ag NPs onto the Ge portion of

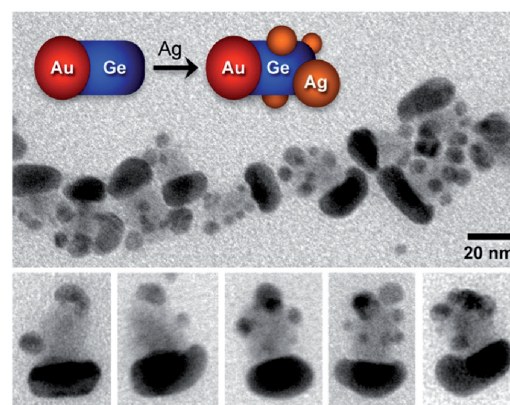


Fig. 14 TEM images of Au–Ge–(Ag)_n NPs. Multiple Ag NPs were deposited onto the Ge domains through a selective galvanic exchange reaction, where the Au domains remained unperturbed. Lower panels display individual Au–Ge–(Ag)_n NPs. Reprinted with permission from ref. 222. © 2013 American Chemical Society.

Au–Ge heterodimer NPs through galvanic exchange.²²² The Au–Ge–(Ag)_n NP product featured single domains of Au and Ge and multiple smaller domains of Ag (Fig. 14), which did not undergo alloying with Au.

10. Concluding remarks and vision

NP conversion chemistry is a maturing field, where there are rich opportunities to better understand conversion chemical reaction mechanisms, as well as to explore more complex reactions and materials. Elements or compounds that have not been explored as NP core materials may undergo conversion chemical reactions, and previously unexplored reagents may allow access to new regimes of conversion chemistry. Of the classes of conversion chemical reactions discussed, the least is known about anion exchange. There is a need to better understand the mechanism of the Kirkendall effect during anion exchange, which will allow for improved morphological control. Simulations will give a deeper, more detailed understanding of the mechanisms of conversion chemical reactions, and advanced characterization techniques will facilitate atomic-scale understanding. While several examples of controlling the composition, morphology, and crystallinity of the products have been discussed, improved control is still needed in many conversion chemical reactions. Simultaneously with gaining better understandings and improving control over conversion chemical reactions, there are plentiful opportunities to use NPs synthesized through conversion chemistry in a host of applications.

Three main approaches are anticipated for creating more complex materials through conversion chemistry: (1) use of more complex starting NPs, such as multicomponent NPs, (2) conducting more complex reactions, either using more complex molecular chemistry, or by performing sequential reactions, and (3) combining conversion chemistry with other bottom-up or top-down methods of patterning materials, such as self-assembly or lithography, where the structure will affect the properties of individual NPs and the larger structure.

Some examples of combining assembly or patterning with conversion chemistry illustrate the potential of this approach for creating novel materials. In two studies already discussed, self-assembled chains of Au/Co core/shell NPs were converted into chains of Au/Co₃O₄ core/shell NPs,¹²⁸ and aligned arrays of Cu nanowires were converted into CuO nanotubes.¹³² In another recent study, films of CdSe NPs were converted into films of PbSe, Cu₂Se, or Ag₂Se NPs.²²³ Conversion chemical reactions can also be conducted prior to assembly, as demonstrated in a recent study, where triangular Ag nanoplatelets were converted into AuAg, PdAg, or PtAg alloy nanoshells, which were then assembled into hydrogels, followed by supercritical drying.²²⁴ The aerogel products exhibited porosity on two length scales, within the nanoshells, and in the spaces between NPs.

Conversion chemistry gives access to a wide range of metal alloy and metal oxide, sulphide, selenide, and phosphide NPs

with complex architectures, including heterostructures, which may be difficult or impossible to obtain using other fabrication techniques. These materials are of interest for a broad range of applications because of their novel catalytic, electronic, optical, magnetic, and electrochemical properties, which enable applications in energy, biomedicine, and sensing.

Applications in energy²²⁵ include electrocatalytic and photocatalytic fuel cells, which utilize the hydrogen evolution reaction (HER),¹⁹⁷ oxygen reduction reaction (ORR),^{226–228} and methanol oxidation reaction (MOR).^{160,229,230} Hollow NPs obtained through conversion chemistry are also of interest for Li-ion battery technology.^{64,231} Multicomponent porous NPs are attractive for applications in catalysis, where the large surface area and alloying noble metals with non-noble metals can both increase catalytic activity and reduce cost.^{232,233}

Conversion chemistry is useful for biomedical applications because it can alter the functional properties of materials (such as the surface plasmon resonance of hollow metal nanostructures^{159,234–238}) and can control the shape and porosity of materials, which are also known to affect their behaviour and uptake into biological systems.^{239–242} NPs synthesized through conversion chemical reactions have potential for use in cancer therapy,²¹⁷ drug delivery,^{200,203,210,211,213,243} imaging,^{244,245} and biosensing.²⁴⁶ Recent developments in the conversion chemistry of rare-earth-based NPs (Section 8) make them potentially useful for drug delivery using pores created through anion exchange reactions, while allowing for simultaneous optical and/or magnetic tracking.^{247,248}

Gas sensing is another important application of hollow NPs. Controlling the composition and porosity of hollow NPs can enhance their sensing performance. For example, SnO₂ nanotubes doped with Ag₂O NPs have significantly faster response and recovery times for sensing ethanol and butanone than the Ag/C/SnO₂ core/shell/shell nanocables from which they were obtained through the Kirkendall effect.²⁴⁹ In another study, porous Fe₂O₃ NPs were more sensitive than solid Fe₂O₃ NPs for detecting CO, H₂, NH₃, and vapours from liquefied petroleum gas.²⁵⁰

Acknowledgements

This work was supported by the National Science Foundation (DMR-1056653).

References

- 1 J. Liu, S. Z. Qiao, J. S. Chen, X. W. Lou, X. Xing and G. Q. Lu, *Chem. Commun.*, 2011, **47**, 12578.
- 2 Z. Wang, L. Zhou and X. W. David Lou, *Adv. Mater.*, 2012, **24**, 1903.
- 3 H. You, S. Yang, B. Ding and H. Yang, *Chem. Soc. Rev.*, 2013, **42**, 2880.

- 4 J. Wang, A. C. Johnston-Peck and J. B. Tracy, *Chem. Mater.*, 2009, **21**, 4462.
- 5 S. Peng and S. Sun, *Angew. Chem., Int. Ed.*, 2007, **46**, 4155.
- 6 J. Park, H. Zheng, Y. Jun and A. P. Alivisatos, *J. Am. Chem. Soc.*, 2009, **131**, 13943.
- 7 A. Cabot, V. F. Puentes, E. Shevchenko, Y. Yin, L. Balcells, M. a. Marcus, S. M. Hughes and A. P. Alivisatos, *J. Am. Chem. Soc.*, 2007, **129**, 10358.
- 8 Y. Yang, R. Bin Yang, H. J. Fan, R. Scholz, Z. Huang, A. Berger, Y. Qin, M. Knez and U. Gösele, *Angew. Chem., Int. Ed.*, 2010, **49**, 1442.
- 9 F. Aldinger, *Acta Metall.*, 1974, **22**, 923.
- 10 A. Kumar, M. Nasrallah and D. L. Douglass, *Oxid. Met.*, 1974, **8**, 227.
- 11 Z. L. Cui, L. F. Dong and Z. K. Zhang, *Nanostruct. Mater.*, 1995, **5**, 829.
- 12 D. Potoczna-Petru and L. Krajczyk, *J. Mater. Sci. Lett.*, 1995, **14**, 1294.
- 13 Y. Yin, R. M. Rioux, C. K. Erdonmez, S. Hughes, G. A. Somorjai and A. P. Alivisatos, *Science*, 2004, **304**, 711.
- 14 J. Chen, B. Wiley, J. McLellan, Y. Xiong, Z.-Y. Li and Y. Xia, *Nano Lett.*, 2005, **5**, 2058.
- 15 X. Gong, Y. Yang and S. Huang, *J. Phys. Chem. C*, 2010, **114**, 18073.
- 16 Y. Sun and Y. Xia, *Nano Lett.*, 2003, **3**, 1569.
- 17 J. Zeng, Q. Zhang, J. Chen and Y. Xia, *Nano Lett.*, 2010, **10**, 30.
- 18 L. Au, X. Lu and Y. Xia, *Adv. Mater.*, 2008, **20**, 2517.
- 19 J. Chen, J. M. McLellan, A. Siekkinen, Y. Xiong, Z.-Y. Li and Y. Xia, *J. Am. Chem. Soc.*, 2006, **128**, 14776.
- 20 M. H. Kim, X. Lu, B. Wiley, E. P. Lee and Y. Xia, *J. Phys. Chem. C*, 2008, **112**, 7872.
- 21 H. Li, M. Zanella, A. Genovese, M. Povia, A. Falqui, C. Giannini and L. Manna, *Nano Lett.*, 2011, **11**, 4964.
- 22 U. Jeong, Y. Xia and Y. Yin, *Chem. Phys. Lett.*, 2005, **416**, 246.
- 23 P. H. C. Camargo, Y. H. Lee, U. Jeong, Z. Zou and Y. Xia, *Langmuir*, 2007, **23**, 2985.
- 24 H. Cheng, B. Huang, X. Qin, X. Zhang and Y. Dai, *Chem. Commun.*, 2012, **48**, 97.
- 25 B. J. Beberwyck, Y. Surendranath and A. P. Alivisatos, *J. Phys. Chem. C*, 2013, **117**, 19759.
- 26 J. B. Rivest and P. K. Jain, *Chem. Soc. Rev.*, 2013, **42**, 89.
- 27 W.-S. Wang, L. Zhen, C.-Y. Xu, L. Yang and W.-Z. Shao, *J. Phys. Chem. C*, 2008, **112**, 19390.
- 28 S. Chen, X. Zhang, X. Hou, Q. Zhou and W. Tan, *Cryst. Growth Des.*, 2010, **10**, 1257.
- 29 S. Mahesh, A. Gopal, R. Thirumalai and A. Ajayaghosh, *J. Am. Chem. Soc.*, 2012, **134**, 7227.
- 30 C. L. Kuo and K. C. Hwang, *Chem. Mater.*, 2013, **25**, 365.
- 31 Y. Sun and Y. Wang, *Nano Lett.*, 2011, **11**, 4386.
- 32 K. Ding, Z. Miao, B. Hu, G. An, Z. Sun, B. Han and Z. Liu, *Langmuir*, 2010, **26**, 10294.
- 33 D.-H. Ha, L. M. Moreau, S. Honrao, R. G. Hennig and R. D. Robinson, *J. Phys. Chem. C*, 2013, **117**, 14303.
- 34 Z. Yang, M. Walls, I. Lisiecki and M. Pileni, *Chem. Mater.*, 2013, **25**, 2372.
- 35 A. C. Johnston-Peck, J. Wang and J. B. Tracy, *ACS Nano*, 2009, **3**, 1077.
- 36 T.-J. Yoon, H. Shao, R. Weissleder and H. Lee, *Part. Part. Syst. Charact.*, 2013, **30**, 667.
- 37 A. Brückman, *Corros. Sci.*, 1967, **7**, 51.
- 38 N. Birks, G. H. Meier, and F. S. Pettit, *Introduction to the High-Temperature Oxidation of Metals*, Cambridge University Press, Cambridge, UK, 2nd edn, 2006.
- 39 R. Nakamura, J.-G. Lee, D. Tokozakura, H. Mori and H. Nakajima, *Mater. Lett.*, 2007, **61**, 1060.
- 40 P. Kofstad, *High-Temperature Oxidation of Metals*, Wiley, New York, 1966.
- 41 P. Kofstad, *High Temperature Corrosion*, Elsevier Applied Science, London, 1988.
- 42 M. Schütze, *Protective Oxide Scales and Their Breakdown*, Wiley, Chichester, 1997.
- 43 J. G. Railsback, A. C. Johnston-Peck, J. Wang and J. B. Tracy, *ACS Nano*, 2010, **4**, 1913.
- 44 M. Verelst, T. O. Ely, C. Amiens, E. Snoeck, P. Lecante, A. Mosset, M. Respaud, J. M. Broto and B. Chaudret, *Chem. Mater.*, 1999, **11**, 2702.
- 45 X.-C. Sun and X.-L. Dong, *Mater. Res. Bull.*, 2002, **37**, 991.
- 46 V. Skumryev, S. Stoyanov, Y. Zhang, G. Hadjipanayis, D. Givord and J. Nogués, *Nature*, 2003, **423**, 850.
- 47 R. K. Zheng, *J. Appl. Phys.*, 2004, **95**, 5244.
- 48 K. Sakiyama, K. Koga, T. Seto, M. Hirasawa and T. Orii, *J. Phys. Chem. B*, 2004, **108**, 523.
- 49 C. M. Wang, D. R. Baer, L. E. Thomas, J. E. Amonette, J. Antony, Y. Qiang and G. Duscher, *J. Appl. Phys.*, 2005, **98**, 094308.
- 50 J. Tracy, D. Weiss, D. Dinega and M. Bawendi, *Phys. Rev. B: Condens. Matter Mater. Phys.*, 2005, **72**, 064404.
- 51 Y. Yin, C. K. Erdonmez, A. Cabot, S. Hughes and A. P. Alivisatos, *Adv. Funct. Mater.*, 2006, **16**, 1389.
- 52 I. S. Lee, N. Lee, J. Park, B. H. Kim, Y.-W. Yi, T. Kim, T. K. Kim, I. H. Lee, S. R. Paik and T. Hyeon, *J. Am. Chem. Soc.*, 2006, **128**, 10658.
- 53 R. Nakamura, J.-G. Lee, D. Tokozakura, H. Mori and H. Nakajima, *Mater. Lett.*, 2007, **61**, 1060.
- 54 Y. Gao, D. Shindo, Y. Bao and K. Krishnan, *Appl. Phys. Lett.*, 2007, **90**, 233105.
- 55 S. Inderhees, J. Borchers, K. Green, M. Kim, K. Sun, G. Strycker and M. Aronson, *Phys. Rev. Lett.*, 2008, **101**, 117202.
- 56 K. Yamamoto, S. A. Majetich, M. R. McCartney, M. Sachan, S. Yamamuro and T. Hirayama, *Appl. Phys. Lett.*, 2008, **93**, 082502.
- 57 P. A. Chernavskii, G. V. Pankina, V. I. Zaikovskii, N. V. Peskov and P. Afanasiev, *J. Phys. Chem. C*, 2008, **112**, 9573.
- 58 X. Zheng, S. Yuan, Z. Tian, S. Yin, J. He, K. Liu and L. Liu, *Chem. Mater.*, 2009, **21**, 4839.
- 59 Q. Ong, A. Wei and X.-M. Lin, *Phys. Rev. B: Condens. Matter Mater. Phys.*, 2009, **80**, 134418.

- 60 L.-I. Hung, C.-K. Tsung, W. Huang and P. Yang, *Adv. Mater.*, 2010, **22**, 1910.
- 61 L. Zhang, P. Hu, X. Zhao, R. Tian, R. Zou and D. Xia, *J. Mater. Chem.*, 2011, **21**, 18279.
- 62 S. Chenna, R. Banerjee and P. A. Crozier, *ChemCatChem*, 2011, **3**, 1051.
- 63 S. Jia, C.-H. Hsia and D. H. Son, *J. Phys. Chem. C*, 2011, **115**, 92.
- 64 B. Koo, H. Xiong, M. D. Slater, V. B. Prakapenka, M. Balasubramanian, P. Podsiadlo, C. S. Johnson, T. Rajh and E. V. Shevchenko, *Nano Lett.*, 2012, **12**, 2429.
- 65 S. Chenna and P. A. Crozier, *Micron*, 2012, **43**, 1188.
- 66 J. A. Medford, A. C. Johnston-Peck and J. B. Tracy, *Nanoscale*, 2013, **5**, 155.
- 67 K.-Y. Niu, J. Park, H. Zheng and A. P. Alivisatos, *Nano Lett.*, 2013, **13**, 5715.
- 68 S. Sadasivan, R. M. Bellabarba and R. P. Tooze, *Nanoscale*, 2013, **5**, 11139.
- 69 K. Kravchyk, L. Protesescu, M. I. Bodnarchuk, F. Krumeich, M. Yarema, M. Walter, C. Guntlin and M. V. Kovalenko, *J. Am. Chem. Soc.*, 2013, **135**, 4199.
- 70 N. Cabrera and N. F. Mott, *Rep. Prog. Phys.*, 1949, **12**, 163.
- 71 V. P. Zhdanov and B. Kasemo, *Chem. Phys. Lett.*, 2008, **452**, 285.
- 72 A. Ermoline and E. L. Dreizin, *Chem. Phys. Lett.*, 2011, **505**, 47.
- 73 A. Auge, A. Weddemann, B. Vogel, F. Wittbracht and A. Hütten, *Appl. Phys. Lett.*, 2010, **96**, 093111.
- 74 A. Fromhold and E. Cook, *Phys. Rev.*, 1967, **163**, 650.
- 75 Y. Hwang, S. Angappane, J. Park, K. An, T. Hyeon and J.-G. Park, *Curr. Appl. Phys.*, 2012, **12**, 808.
- 76 N. Doan, K. Kontturi and C. Johans, *J. Colloid Interface Sci.*, 2010, **350**, 126.
- 77 I. Lisiecki, M. Walls, D. Parker and M. P. Pileni, *Langmuir*, 2008, **24**, 4295.
- 78 E. Klecha, D. Ingers, M. Walls and M. P. Pileni, *Langmuir*, 2009, **25**, 2824.
- 79 I. Lisiecki, S. Turner, S. Bals, M. P. Pileni and G. Van Tendeloo, *Chem. Mater.*, 2009, **21**, 2335.
- 80 E. Klecha, I. Arfaoui, J. Richardi, D. Ingers and M.-P. Pileni, *Phys. Chem. Chem. Phys.*, 2011, **13**, 2953.
- 81 Z. Yang, I. Lisiecki, M. Walls and M.-P. Pileni, *ACS Nano*, 2013, **7**, 1342.
- 82 W. Wu and M. M. Maye, *Small*, 2014, **10**, 271.
- 83 R. Nakamura, D. Tokozakura, H. Nakajima, J.-G. Lee and H. Mori, *J. Appl. Phys.*, 2007, **101**, 074303.
- 84 S. Jia, C.-H. Hsia and D. H. Son, *J. Phys. Chem. C*, 2011, **115**, 92.
- 85 C. Wagner, *Z. Phys. Chem.*, 1933, **21**, 25.
- 86 K. Fueki and J. B. Wagner, *J. Electrochem. Soc.*, 1965, **112**, 384.
- 87 F. Gesmundo and F. Viani, *Corros. Sci.*, 1978, **18**, 217.
- 88 G. Valensi, *C. R. Acad. Sci. Paris*, 1936, **202**, 309.
- 89 G. Valensi, *Compt. Rend.*, 1936, **202**, 309.
- 90 R. E. Carter, *J. Chem. Phys.*, 1961, **35**, 1137.
- 91 R. E. Carter, *J. Chem. Phys.*, 1961, **34**, 2010.
- 92 A. Fromhold and E. Cook, *Phys. Rev.*, 1968, **175**, 877.
- 93 A. T. Fromhold, *J. Phys. Chem. Solids*, 1988, **49**, 1159.
- 94 L. Zhou, A. Rai, N. Piekiel, X. Ma and M. R. Zachariah, *J. Phys. Chem. C*, 2008, **112**, 16209.
- 95 B. J. Henz, T. Hawa and M. R. Zachariah, *J. Appl. Phys.*, 2010, **107**, 024901.
- 96 R. Nakamura, D. Tokozakura, J.-G. Lee, H. Mori and H. Nakajima, *Acta Mater.*, 2008, **56**, 5276.
- 97 T.-L. Ha, J. G. Kim, S. M. Kim and I. S. Lee, *J. Am. Chem. Soc.*, 2013, **135**, 1378.
- 98 R. Nakamura, G. Matsubayashi, H. Tsuchiya, S. Fujimoto and H. Nakajima, *Acta Mater.*, 2009, **57**, 4261.
- 99 K. N. Tu and U. Gösele, *Appl. Phys. Lett.*, 2005, **86**, 093111.
- 100 A. M. Gusak, T. V. Zaporozhets, K. N. Tu and U. Gösele, *Philos. Mag.*, 2005, **85**, 4445.
- 101 A. V. Evteev, E. V. Levchenko, I. V. Belova and G. E. Murch, *Philos. Mag.*, 2007, **87**, 3787.
- 102 A. V. Evteev, E. V. Levchenko, I. V. Belova and G. E. Murch, *Philos. Mag.*, 2008, **88**, 1525.
- 103 R. Nakamura, G. Matsubayashi, H. Tsuchiya, S. Fujimoto and H. Nakajima, *Acta Mater.*, 2009, **57**, 5046.
- 104 E. Muthuswamy, P. R. Kharel, G. Lawes and S. L. Brock, *ACS Nano*, 2009, **3**, 2383.
- 105 A. E. Henkes, Y. Vasquez and R. E. Schaak, *J. Am. Chem. Soc.*, 2007, **129**, 1896.
- 106 A. E. Henkes and R. E. Schaak, *Inorg. Chem.*, 2008, **47**, 671.
- 107 A. Earnshaw and N. Greenwood, *Chemistry of the Elements*, Elsevier Butterworth-Heinemann, Oxford, 2nd edn, 1997.
- 108 R.-K. Chiang and R.-T. Chiang, *Inorg. Chem.*, 2007, **46**, 369.
- 109 A. E. Henkes and R. E. Schaak, *Chem. Mater.*, 2007, **19**, 4234.
- 110 E. Muthuswamy, G. H. L. Savithra and S. L. Brock, *ACS Nano*, 2011, **5**, 2402.
- 111 E. Muthuswamy and S. L. Brock, *Chem. Commun.*, 2011, **47**, 12334.
- 112 S. Carencu, Y. Hu, I. Florea, O. Ersen, C. Boissière, N. Mézailles and C. Sanchez, *Chem. Mater.*, 2012, **24**, 4134.
- 113 D. P. Dinega and M. G. Bawendi, *Angew. Chem., Int. Ed.*, 1999, **38**, 1788.
- 114 S. Sun and C. B. Murray, *J. Appl. Phys.*, 1999, **85**, 4325.
- 115 D.-H. Ha, L. M. Moreau, C. R. Bealing, H. Zhang, R. G. Hennig and R. D. Robinson, *J. Mater. Chem.*, 2011, **21**, 11498.
- 116 Z. Wang, L. Pan, H. Hu and S. Zhao, *CrystEngComm*, 2010, **12**, 1899.
- 117 S. Gullapalli, J. M. Grider, H. G. Bagaria, K.-S. Lee, M. Cho, V. L. Colvin, G. E. Jabbour and M. S. Wong, *Nanotechnology*, 2012, **23**, 495605.
- 118 G. Xiao, Y. Zeng, Y. Jiang, J. Ning, W. Zheng, B. Liu, X. Chen, G. Zou and B. Zou, *Small*, 2013, **9**, 793.
- 119 M. Ibáñez, J. Fan, W. Li, D. Cadavid, R. Nafria, A. Carrete and A. Cabot, *Chem. Mater.*, 2011, **23**, 3095.

- 120 H. J. Fan, M. Knez, R. Scholz, D. Hesse, K. Nielsch, M. Zacharias and U. Gösele, *Nano Lett.*, 2007, **7**, 993.
- 121 X. Liang, X. Wang, Y. Zhuang, B. Xu, S. Kuang and Y. Li, *J. Am. Chem. Soc.*, 2008, **130**, 2736.
- 122 A. Cabot, R. K. Smith, Y. Yin, H. Zheng, B. M. Reinhard, H. Liu and A. P. Alivisatos, *ACS Nano*, 2008, **2**, 1452.
- 123 M. F. Sarac, W.-C. Wu and J. B. Tracy, *Chem. Mater.*, 2014, **26**, 3057.
- 124 Z. Nie, A. Petukhova and E. Kumacheva, *Nat. Nanotechnol.*, 2010, **5**, 15.
- 125 L. J. Hill and J. Pyun, *ACS Appl. Mater. Interfaces*, 2014, **6**, 6022.
- 126 J. B. Tracy and T. M. Crawford, *MRS Bull.*, 2013, **38**, 915.
- 127 B. Y. Kim, I.-B. Shim, Z. O. Araci, S. S. Saavedra, O. L. a. Monti, N. R. Armstrong, R. Sahoo, D. N. Srivastava and J. Pyun, *J. Am. Chem. Soc.*, 2010, **132**, 3234.
- 128 B. Y. Kim, S.-H. Yu, H. S. Kim, D.-C. Lee, I.-B. Shim, S. E. Derosa, Y.-E. Sung and J. Pyun, *J. Mater. Chem.*, 2011, **21**, 14163.
- 129 P. Y. Keng, M. M. Bull, I. Shim, K. G. Nebesny, N. R. Armstrong, Y. Sung, K. Char and J. Pyun, *Chem. Mater.*, 2011, **23**, 1120.
- 130 L. De Trizio, A. Figuerola, L. Manna, A. Genovese, C. George, R. Brescia, Z. Saghi, R. Simonutti, M. Van Huis and A. Falqui, *ACS Nano*, 2012, **6**, 32.
- 131 Y. Ren, W. K. Chim, S. Y. Chiam, J. Q. Huang, C. Pi and J. S. Pan, *Adv. Funct. Mater.*, 2010, **20**, 3336.
- 132 A.-A. El Mel, M. Buffière, P.-Y. Tessier, S. Konstantinidis, W. Xu, K. Du, I. Wathuthanthri, C.-H. Choi, C. Bittencourt and R. Snyders, *Small*, 2013, **9**, 2838.
- 133 S. Jeong, M. T. McDowell and Y. Cui, *ACS Nano*, 2011, **5**, 5800.
- 134 H. Sun, Y. Chen, X. Wang, Y. Xie, W. Li and X. Zhang, *J. Nanopart. Res.*, 2011, **13**, 97.
- 135 S.-B. Wang, W. Zhu, J. Ke, J. Gu, A.-X. Yin, Y.-W. Zhang and C.-H. Yan, *Chem. Commun.*, 2013, **49**, 7168.
- 136 C. E. Carlton, S. Chen, P. J. Ferreira, L. F. Allard and Y. Shao-Horn, *J. Phys. Chem. Lett.*, 2012, **3**, 161.
- 137 L. Dubau, F. Maillard, M. Chatenet, J. André and E. Rossinot, *Electrochim. Acta*, 2010, **56**, 776.
- 138 L. Dubau, J. Durst, F. Maillard, L. Guétaz, M. Chatenet, J. André and E. Rossinot, *Electrochim. Acta*, 2011, **56**, 10658.
- 139 C. Chen, Y. Kang, Z. Huo, Z. Zhu, W. Huang, H. L. Xin, J. D. Snyder, D. Li, J. A. Herron, M. Mavrikakis, M. Chi, K. L. More, Y. Li, N. M. Markovic, G. A. Somorjai, P. Yang and V. R. Stamenkovic, *Science*, 2014, **343**, 1339.
- 140 J. Erlebacher and D. Margetis, *Phys. Rev. Lett.*, 2014, **112**, 155505.
- 141 M. Lopez-Haro, L. Dubau, L. Guétaz, P. Bayle-Guillemaud, M. Chatenet, J. André, N. Caqué, E. Rossinot and F. Maillard, *Appl. Catal., B*, 2014, **152–153**, 300.
- 142 S. Jana, J. W. Chang and R. M. Rioux, *Nano Lett.*, 2013, **13**, 3618.
- 143 E. A. Anumol, C. Nethravathi and N. Ravishankar, *Part. Part. Syst. Charact.*, 2013, **30**, 590.
- 144 X. Xia, Y. Wang, A. Ruditskiy and Y. Xia, *Adv. Mater.*, 2013, **25**, 6313.
- 145 Y. Sun and Y. Xia, *Nano Lett.*, 2003, **3**, 1569.
- 146 Q. Zhang, J. Xie, J. Y. Lee, J. Zhang and C. Boothroyd, *Small*, 2008, **4**, 1067.
- 147 V. Bansal, H. Jani, J. Du Plessis, P. J. Coloe and S. K. Bhargava, *Adv. Mater.*, 2008, **20**, 717.
- 148 M. Mohl, A. Kumar, A. L. M. Reddy, A. Kukovecz, Z. Konya, I. Kiricsi, R. Vajtai and P. M. Ajayan, *J. Phys. Chem. C*, 2010, **114**, 389.
- 149 I. Najdovski, A. P. O'Mullane and S. K. Bhargava, *Electrochem. Commun.*, 2010, **12**, 1535.
- 150 Q. Cui, Y. Sha, J. Chen and Z. Gu, *J. Nanopart. Res.*, 2011, **13**, 4785.
- 151 M. Clay, Q. Cui, Y. Sha, J. Chen, A. J. Rondinone, Z. Wu, J. Chen and Z. Gu, *Mater. Lett.*, 2012, **88**, 143.
- 152 Y. Sun, B. Wiley, Z.-Y. Li and Y. Xia, *J. Am. Chem. Soc.*, 2004, **126**, 9399.
- 153 X. Lu, L. Au, J. McLellan, Z.-Y. Li, M. Marquez and Y. Xia, *Nano Lett.*, 2007, **7**, 1764.
- 154 X. Teng, Q. Wang, P. Liu, W. Han, A. I. Frenkel, W. Wen, N. Marinkovic, J. C. Hanson and J. A. Rodriguez, *J. Am. Chem. Soc.*, 2008, **130**, 1093.
- 155 M. H. Kim, X. Lu, B. Wiley, E. P. Lee and Y. Xia, *J. Phys. Chem. C*, 2008, **112**, 7872.
- 156 J. Zeng, Q. Zhang, J. Chen and Y. Xia, *Nano Lett.*, 2010, **10**, 30.
- 157 M. Mohl, D. Dobo, A. Kukovecz, Z. Konya, K. Kordas, J. Wei, R. Vajtai and P. M. Ajayan, *J. Phys. Chem. C*, 2011, **115**, 9403.
- 158 Y. Ridelman, G. Singh, R. Popovitz-Biro, S. G. Wolf, S. Das and R. Klajn, *Small*, 2012, **8**, 654.
- 159 D. Wan, X. Xia, Y. Wang and Y. Xia, *Small*, 2013, **9**, 3111.
- 160 W. Zhang, J. Yang and X. Lu, *ACS Nano*, 2012, **6**, 7397.
- 161 E. González, J. Arbiol and V. F. Puntes, *Science*, 2011, **334**, 1377.
- 162 Y.-H. Chien, M.-F. Tsai, V. Shanmugam, K. Sardar, C.-L. Huang and C.-S. Yeh, *Nanoscale*, 2013, **5**, 3863.
- 163 K. A. Kozek, K. M. Kozek, W.-C. Wu, S. R. Mishra and J. B. Tracy, *Chem. Mater.*, 2013, **25**, 4537.
- 164 M. Pradhan, J. Chowdhury, S. Sarkar, A. K. Sinha and T. Pal, *J. Phys. Chem. C*, 2012, **116**, 24301.
- 165 G. McNay, D. Eustace, W. E. Smith, K. Faulds and D. Graham, *Appl. Spectrosc.*, 2011, **65**, 825.
- 166 Karvianto and G. M. Chow, *J. Nanopart. Res.*, 2012, **14**, 1186.
- 167 L. Polavarapu and L. M. Liz-Marzán, *Nanoscale*, 2013, **5**, 4355.
- 168 C. Wang, S. Peng, R. Chan and S. Sun, *Small*, 2009, **5**, 567.
- 169 M. S. Shore, J. Wang, A. C. Johnston-Peck, A. L. Oldenburg and J. B. Tracy, *Small*, 2011, **7**, 230.
- 170 Y. Sun, B. T. Mayers and Y. Xia, *Nano Lett.*, 2002, **2**, 481.
- 171 Y. Yin, C. Erdonmez, S. Aloni and A. P. Alivisatos, *J. Am. Chem. Soc.*, 2006, **128**, 12671.
- 172 X. Lu, H.-Y. Tuan, J. Chen, Z.-Y. Li, B. A. Korgel and Y. Xia, *J. Am. Chem. Soc.*, 2007, **129**, 1733.

- 173 K.-Y. Niu, S. A. Kulnich, J. Yang, A. L. Zhu and X.-W. Du, *Chem.-Eur. J.*, 2012, **18**, 4234.
- 174 M. Jin, H. Zhang, J. Wang, X. Zhong, N. Lu, Z. Li, Z. Xie, M. J. Kim and Y. Xia, *ACS Nano*, 2012, **6**, 2566.
- 175 S. Xie, M. Jin, J. Tao, Y. Wang, Z. Xie, Y. Zhu and Y. Xia, *Chem.-Eur. J.*, 2012, **18**, 14974.
- 176 M. Jin, G. He, H. Zhang, J. Zeng, Z. Xie and Y. Xia, *Angew. Chem., Int. Ed.*, 2011, **50**, 10560.
- 177 H.-P. Liang, L.-J. Wan, C.-L. Bai and L. Jiang, *J. Phys. Chem. B*, 2005, **109**, 7795.
- 178 A. M. Schwartzberg, T. Y. Olson, C. E. Talley and J. Z. Zhang, *J. Phys. Chem. B*, 2006, **110**, 19935.
- 179 M. Chen and L. Gao, *Inorg. Chem.*, 2006, **45**, 5145.
- 180 M. Mohl, A. Kumar, A. L. M. Reddy, A. Kukovecz, Z. Konya, I. Kiricsi, R. Vajtai and P. M. Ajayan, *J. Phys. Chem. C*, 2010, **114**, 389.
- 181 M. H. Oh, T. Yu, S.-H. Yu, B. Lim, K.-T. Ko, M.-G. Willinger, D.-H. Seo, B. H. Kim, M. G. Cho, J.-H. Park, K. Kang, Y.-E. Sung, N. Pinna and T. Hyeon, *Science*, 2013, **340**, 964.
- 182 M. Saruyama, Y.-G. So, K. Kimoto, S. Taguchi, Y. Kanemitsu and T. Teranishi, *J. Am. Chem. Soc.*, 2011, **133**, 17598.
- 183 B. J. Beberwyck and A. P. Alivisatos, *J. Am. Chem. Soc.*, 2012, **134**, 19977.
- 184 D. H. Son, S. M. Hughes, Y. Yin and A. P. Alivisatos, *Science*, 2004, **306**, 1009.
- 185 Y. Feldman, E. Wasserman, D. J. Srolovitz and R. Tenne, *Science*, 1995, **267**, 222.
- 186 Y. Feldman, G. L. Frey, M. Homyonfer, V. Lyakhovitskaya, L. Margulis, H. Cohen, G. Hodes, J. L. Hutchison and R. Tenne, *J. Am. Chem. Soc.*, 1996, **118**, 5362.
- 187 E. Muthuswamy and S. L. Brock, *J. Am. Chem. Soc.*, 2010, **132**, 15849.
- 188 S. Xiong and H. C. Zeng, *Angew. Chem., Int. Ed.*, 2012, **51**, 949.
- 189 J. Gopalakrishnan, S. Pandey and K. K. Rangan, *Chem. Mater.*, 1997, **9**, 2113.
- 190 X. Huang, M. Wang, M. Willinger, L. Shao, D. S. Su and X. Meng, *ACS Nano*, 2012, **6**, 7333.
- 191 H. Zhang, L. V. Solomon, D.-H. Ha, S. Honrao, R. G. Hennig and R. D. Robinson, *Dalton Trans.*, 2013, **42**, 12596.
- 192 P. Cai, D.-K. Ma, Q.-C. Liu, S.-M. Zhou, W. Chen and S.-M. Huang, *J. Mater. Chem. A*, 2013, **1**, 5217.
- 193 I. T. Sines, D. D. Vaughn, A. J. Bicchii, C. E. Kingsley, E. J. Popczun and R. E. Schaak, *Chem. Mater.*, 2012, **24**, 3088.
- 194 X. Xia, C. Zhu, J. Luo, Z. Zeng, C. Guan, C. F. Ng, H. Zhang and H. J. Fan, *Small*, 2014, **10**, 766.
- 195 Z. Wu, B. Fang, A. Bonakdarpour, A. Sun, D. P. Wilkinson and D. Wang, *Appl. Catal., B*, 2012, **125**, 59.
- 196 Z. Zang, H.-B. Yao, Y. Zhou, W. Yao and S. Yu, *Chem. Mater.*, 2008, **20**, 4749.
- 197 Y. Xu, R. Wu, J. Zhang, Y. Shi and B. Zhang, *Chem. Commun.*, 2013, **49**, 6656.
- 198 I. T. Sines and R. E. Schaak, *J. Am. Chem. Soc.*, 2011, **133**, 1294.
- 199 S. Zhuo, Y. Xu, W. Zhao, J. Zhang and B. Zhang, *Angew. Chem., Int. Ed.*, 2013, **52**, 8602.
- 200 Z. Xu, P. Ma, C. Li, Z. Hou, X. Zhai, S. Huang and J. Lin, *Biomaterials*, 2011, **32**, 4161.
- 201 G. Tian, Z. Gu, X. Liu, L. Zhou, W. Yin, L. Yan, S. Jin, W. Ren, G. Xing, S. Li and Y. Zhao, *J. Phys. Chem. C*, 2011, **115**, 23790.
- 202 T. Grzyb, A. Gruszczyka, R. J. Wiglusz, Z. Śniadecki, B. Idzikowski and S. Lis, *J. Mater. Chem.*, 2012, **22**, 22989.
- 203 X. Kang, D. Yang, P. Ma, Y. Dai, M. Shang, D. Geng, Z. Cheng and J. Lin, *Langmuir*, 2013, **29**, 1286.
- 204 L. Zhang, H. Jiu, Y. Fu, Y. Sun, P. Chen, Y. Li and S. Ma, *Mater. Lett.*, 2013, **101**, 47.
- 205 Y. Gao, M. Fan, Q. Fang and W. Han, *New J. Chem.*, 2013, **37**, 670.
- 206 X. Kang, D. Yang, Y. Dai, M. Shang, Z. Cheng, X. Zhang, H. Lian, P. Ma and J. Lin, *Nanoscale*, 2013, **5**, 253.
- 207 J. Zhang, Y. Wang, L. Guo and P. Dong, *Dalton Trans.*, 2013, **42**, 3542.
- 208 D. Chen, L. Lei, J. Xu, A. Yang and Y. Wang, *Nanotechnology*, 2013, **24**, 085708.
- 209 F. Zhang, Y. Shi, X. Sun, D. Zhao and G. D. Stucky, *Chem. Mater.*, 2009, **21**, 5237.
- 210 R. Lv, S. Gai, Y. Dai, F. He, N. Niu and P. Yang, *Inorg. Chem.*, 2014, **53**, 998.
- 211 R. Lv, S. Gai, Y. Dai, N. Niu, F. He and P. Yang, *ACS Appl. Mater. Interfaces*, 2013, **5**, 10806.
- 212 L. Zhang, M. Yin, H. You, M. Yang, Y. Song and Y. Huang, *Inorg. Chem.*, 2011, **50**, 10608.
- 213 Z. Xu, Y. Cao, C. Li, P. Ma, X. Zhai, S. Huang, X. Kang, M. Shang, D. Yang, Y. Dai and J. Lin, *J. Mater. Chem.*, 2011, **21**, 3686.
- 214 J. Zhang, Y. Wang, Z. Xu, H. Zhang, P. Dong, L. Guo, F. Li, S. Xin and W. Zeng, *J. Mater. Chem. B*, 2013, **1**, 330.
- 215 T. Teranishi and M. Sakamoto, *J. Phys. Chem. Lett.*, 2013, **4**, 2867.
- 216 E. V. Shevchenko, M. I. Bodnarchuk, M. V. Kovalenko, D. V. Talapin, R. K. Smith, S. Aloni, W. Heiss and A. P. Alivisatos, *Adv. Mater.*, 2008, **20**, 4323.
- 217 J. Gao, G. Liang, B. Zhang, Y. Kuang, X. Zhang and B. Xu, *J. Am. Chem. Soc.*, 2007, **129**, 1428.
- 218 R. E. Schaak and M. E. Williams, *ACS Nano*, 2012, **6**, 8492.
- 219 M. R. Buck, J. F. Bondi and R. E. Schaak, *Nat. Chem.*, 2012, **4**, 37.
- 220 L. J. Hill, M. M. Bull, Y. Sung, A. G. Simmonds, P. T. Dirlam, N. E. Richey, S. E. DeRosa, I.-B. Shim, D. Guin, P. J. Costanzo, N. Pinna, M.-G. Willinger, W. Vogel, K. Char and J. Pyun, *ACS Nano*, 2012, **6**, 8632.
- 221 M. J. Bradley, A. J. Bicchii and R. E. Schaak, *Chem. Mater.*, 2013, **25**, 1886.
- 222 C. G. Read, A. J. Bicchii and R. E. Schaak, *Chem. Mater.*, 2013, **25**, 4304.

- 223 J. B. Rivest, R. Buonsanti, T. E. Pick, L. Zhu, E. Lim, C. Clavero, E. Schaible, B. A. Helms and D. J. Milliron, *J. Am. Chem. Soc.*, 2013, **135**, 7446.
- 224 K. G. S. Ranmohotti, X. Gao and I. U. Arachchige, *Chem. Mater.*, 2013, **25**, 3528.
- 225 M. Fayette and R. D. Robinson, *J. Mater. Chem. A*, 2014, **2**, 5965.
- 226 S. J. Bae, S. J. Yoo, Y. Lim, S. Kim, Y. Lim, J. Choi, K. S. Nahm, S. J. Hwang, T.-H. Lim, S.-K. Kim and P. Kim, *J. Mater. Chem.*, 2012, **22**, 8820.
- 227 Y. Zhang, C. Ma, Y. Zhu, R. Si, Y. Cai, J. X. Wang and R. R. Adzic, *Catal. Today*, 2013, **202**, 50.
- 228 H.-H. Li, C.-H. Cui, S. Zhao, H.-B. Yao, M.-R. Gao, F.-J. Fan and S.-H. Yu, *Adv. Energy Mater.*, 2012, **2**, 1182.
- 229 B. Y. Xia, H. Bin Wu, X. Wang and X. W. Lou, *J. Am. Chem. Soc.*, 2012, **134**, 13934.
- 230 X. Huang, Y. Chen, E. Zhu, Y. Xu, X. Duan and Y. Huang, *J. Mater. Chem. A*, 2013, **1**, 14449.
- 231 Y. Hu, X. Huang, K. Wang, J. Liu, J. Jiang, R. Ding, X. Ji and X. Li, *J. Solid State Chem.*, 2010, **183**, 662.
- 232 D. A. Cantane, F. E. R. Oliveira, S. F. Santos and F. H. B. Lima, *Appl. Catal., B*, 2013, **136–137**, 351.
- 233 L. Dubau, J. Durst, F. Maillard, L. Guétaz, M. Chatenet, J. André and E. Rossinot, *Electrochim. Acta*, 2011, **56**, 10658.
- 234 S. E. Skrabalak, J. Chen, L. Au, X. Lu, X. Li and Y. Xia, *Adv. Mater.*, 2007, **19**, 3177.
- 235 S. E. Skrabalak, J. Chen, Y. Sun, X. Lu, L. Au, C. M. Copley and Y. Xia, *Acc. Chem. Res.*, 2008, **41**, 1587.
- 236 Y. Xia, W. Li, C. M. Copley, J. Chen, X. Xia, Q. Zhang, M. Yang, E. C. Cho and P. K. Brown, *Acc. Chem. Res.*, 2011, **44**, 914.
- 237 W. Li, P. K. Brown, L. V. Wang and Y. Xia, *Contrast Media Mol. Imaging*, 2011, **6**, 370.
- 238 G. D. Moon, S.-W. Choi, X. Cai, W. Li, E. C. Cho, U. Jeong, L. V. Wang and Y. Xia, *J. Am. Chem. Soc.*, 2011, **133**, 4762.
- 239 J. E. Gagner, M. D. Lopez, J. S. Dordick and R. W. Siegel, *Biomaterials*, 2011, **32**, 7241.
- 240 S. Dasgupta, T. Auth and G. Gompper, *Nano Lett.*, 2014, **14**, 687.
- 241 R. Agarwal, V. Singh, P. Journey, L. Shi, S. V. Sreenivasan and K. Roy, *Proc. Natl. Acad. Sci. U. S. A.*, 2013, **110**, 17247.
- 242 S. Barua, J.-W. Yoo, P. Kolhar, A. Wakankar, Y. R. Gokarn and S. Mitragotri, *Proc. Natl. Acad. Sci. U. S. A.*, 2013, **110**, 3270.
- 243 K. Cheng, S. Peng, C. Xu and S. Sun, *J. Am. Chem. Soc.*, 2009, **131**, 10637.
- 244 J. Gao, G. Liang, J. S. Cheung, Y. Pan, Y. Kuang, F. Zhao, B. Zhang, X. Zhang, E. X. Wu and B. Xu, *J. Am. Chem. Soc.*, 2008, **130**, 11828.
- 245 C. Wang, Y. Wang, L. Xu, X. Shi, X. Li, X. Xu, H. Sun, B. Yang and Q. Lin, *Small*, 2013, **9**, 413.
- 246 H. Zhu, J. Wang and G. Xu, *Cryst. Growth Des.*, 2009, **9**, 633.
- 247 C. Bouzigues, T. Gacoin and A. Alexandrou, *ACS Nano*, 2011, **5**, 8488.
- 248 S. Gai, C. Li, P. Yang and J. Lin, *Chem. Rev.*, 2014, **114**, 2343.
- 249 X. Chen, Z. Guo, W.-H. Xu, H.-B. Yao, M.-Q. Li, J.-H. Liu, X.-J. Huang and S.-H. Yu, *Adv. Funct. Mater.*, 2011, **21**, 2049.
- 250 N. D. Cuong, T. T. Hoa, D. Q. Khieu, N. D. Hoa and N. Van Hieu, *Curr. Appl. Phys.*, 2012, **12**, 1355.

CHAPTER 4: Silica Overcoating of CdSe/CdS Quantum Dot Nanorods with Tunable Morphologies

The following manuscript has been submitted and is under review as “Silica Overcoating of CdSe/CdS Quantum Dot Nanorods with Tunable Morphologies” by Bryan D. Anderson, Wei-Chen Wu, and Joseph B. Tracy. Anderson’s contribution to the research included the research conceptualization, synthesizing all of the nanoparticles and performing experiments, performing microscopic analyses, and performing optical characterization. Wu’s contribution included insightful discussions about terminating SiO₂ growth with PEG-silane.

4.1 Motivation

Our motivation for this study was to encapsulate CdSe/CdS QDNRs with a SiO₂. SiO₂ is a useful material that has a relatively high dielectric constant, is chemically inert, and can serve a layer for further surface modifications. Furthermore, SiO₂ is employed in many other technological applications. These properties make SiO₂ an ideal material for functionalizing the surface of QDNRs. Motivation for this research project is three-fold: (1) To develop nanoparticle composites with environmentally safe materials and materials that can be readily employed in industrial processes, (2) determine pathways that can further improve the synthetic routes for composite NP syntheses, and (3) find synthetic routes that can control NP morphologies. With this motivation, the objective was established to develop a route for depositing silica overcoatings with controlled morphologies onto semiconductor nanoparticles with anisotropic shapes.

4.2 Manuscript Reprint

Silica Overcoating of CdSe/CdS Quantum Dot Nanorods with Controlled Morphologies

Bryan D. Anderson, Wei-Chen Wu, and Joseph B. Tracy*

Department of Materials Science and Engineering, North Carolina State University, Raleigh, North Carolina 27695, United States

Silica, quantum dot nanorods, Igepal CO-520, NP-5, reverse micelle

ABSTRACT: CdSe/CdS quantum dot nanorods (QDNRs) exhibit anisotropic optical properties. Overcoating QDNRs with SiO₂ shells is desirable for protecting the surface of the inorganic core, imparting dispersibility in water, and enabling functionalization with silanes. While several methods have been developed for encapsulating spherical CdSe-based quantum dots in SiO₂, extension of these approaches to QDNRs has been limited. Here, we report a reverse microemulsion approach for controlled deposition of SiO₂ overcoatings with thicknesses of 2-12 nm onto CdSe/CdS QDNRs with aspect ratios up to 19. Addition of poly(ethylene glycol) silane (PEG-silane) during SiO₂ deposition terminates the reaction and allows facile control over the shell thickness, especially for thinner shells. By independently controlling the amounts of tetraethyl orthosilicate (TEOS), ammonium hydroxide (NH₄OH), and water, morphological control is achieved to give uniform SiO₂ shells or heterogeneous deposition onto the ends of QDNRs as lobed structures, which can appear as nano-lollipops (single lobe) or nano-dumbbells (double lobes). Especially for QDNRs of high aspect ratios, we report breakage of the double-lobed structures. The SiO₂ overcoating process causes a reduction in the fluorescence quantum yield of approximately 20%, which we attribute to NH₃ used as a catalyst in this reaction.

INTRODUCTION

There has been significant interest for nearly 20 years in overcoating inorganic nanoparticles (NPs) with SiO₂,¹⁻³ which is biocompatible,⁴ can serve as a spacer^{5,6} or medium for incorporating dye for use in surface-enhanced Raman spectroscopy (SERS),⁷ and enhances the thermal stability of the encapsulated core material.⁸ SiO₂ overcoatings also allow universal functionalization of many different kinds of NP core materials, where silane chemistry can be used to functionalize the outer surface of the NP irrespective of the core material and its surface chemistry.

SiO₂-coated quantum dots are of interest for biomedical applications, where the SiO₂ coating promotes dispersion in water and long-term chemical stability.⁹⁻¹² These properties are particularly useful for sensing and probing and labeling cells and tissue.¹²⁻¹⁵ Composite SiO₂ NPs containing QDs, other NPs, and/or dyes can have novel multifunctional properties.¹⁶⁻²¹ Photonic conversion of SiO₂-encapsulated QDs makes them suitable candidates for employment in optoelectronics, such as displays,²² photodetectors,²³ photovoltaics,²⁴ and lasers.²⁵ For these applications, QDs are often embedded in SiO₂ or polymer matrices.^{22,25} Controlling the spacing between QD cores in films is important for optoelectronic devices²⁶ and may also be accomplished using SiO₂ as a spacer.

In CdSe/CdS core/shell quantum dot nanorods (QDNRs), the heterostructure and anisotropic shape strongly influence the physical properties.²⁷ The CdS shell serves as a passivating layer that inhibits chemical and photochemical degradation of the CdSe core and increases the fluorescence quantum yield (QY). Until recently,²⁸ typical QYs for CdSe/CdS QDNRs have been 70-75% for low aspect ratios (ARs).²⁹ Significant optical

and electronic anisotropy, including polarized optical absorbance and photoluminescence, arise from the anisotropic shape of QDNRs.³⁰⁻³² The large CdS shell serves as an optical antenna, whose high extinction cross section allows for multiphoton adsorption by QDNRs.^{25,33} Spatially-controlled deposition of other inorganic materials onto QDNRs has also been demonstrated.^{34,35} The anisotropic morphology affords unique opportunities for self-assembly, such as forming aligned QDNR arrays, whose physical properties may be observed and exploited on the macroscale.^{36,37}

SiO₂ overcoatings on CdSe/CdS QDNRs (SiO₂-QDNRs) are desired to preserve the long-term optical integrity of the QDNR cores and for use as a template for further surface modification.¹¹ SiO₂ allows QDNRs to disperse in water^{38,39} and provides good chemical stability.⁴⁰ In comparison with spherical QDs, controlling the uniformity and morphology of SiO₂ overcoatings on QDNRs presents a special set of challenges and opportunities. A reverse microemulsion approach using nonionic surfactants, such as polyoxyethylene(5)nonylphenyl ether (Igepal CO-520), has become increasingly common for depositing SiO₂ shells onto different kinds of NPs. The reverse micelles serve as nanoreactors, which aid in controlling the conditions for the NH₃-catalyzed hydrolysis of tetraethyl orthosilicate (TEOS) and condensation of SiO₂ onto the QDNRs.^{2,9,16,41,42} We chose the reverse microemulsion approach for depositing SiO₂ shells onto QDNRs after a preliminary investigation of a modified Stöber method using an additional cetyltrimethylammonium bromide (CTAB) coating as a template for deposition of SiO₂.^{43,44} In our experience, the reverse microemulsion approach is more straight-forward for overcoating QDNRs that are initially stabilized with hydrophobic ligands and gives better control over the

SiO₂ shell morphology than CTAB encapsulation and TEOS addition.

There is a need to better understand and gain improved control over the process of overcoating QDNRs with SiO₂. Here, we report morphological control of the SiO₂ shell on QDNRs by adjusting the relative concentrations of TEOS, water, and Igepal CO-520. Under different conditions, SiO₂ can be deposited uniformly along the entire length of the QDNR or selectively onto the ends, forming either lollipop (single lobe) or dumbbell (double lobe) structures. Under some reaction conditions, SiO₂-QDNRs can undergo controlled crosslinking between their ends. Poly(ethylene glycol) silane (PEG-silane) can also be added to the reaction mixture to terminate deposition of SiO₂, resulting in thin SiO₂ shells.

This study builds on other reports of overcoating anisotropic semiconductor NPs with SiO₂ using a reverse microemulsion approach.⁴⁵⁻⁴⁸ For example, when CdSe/CdS tetrapods were overcoated with SiO₂, the concentration of water controlled the uniformity of the shell; deposition became selective at the vertex of the tetrapod when the water to Igepal CO-520 ratio was decreased.⁴⁵ In the same study, deposition of SiO₂ on the ends of CdSe/CdS QDNRs was also demonstrated, but deposition of uniform shells on QDNRs was not reported.⁴⁵ A more recent report showed morphological control of SiO₂ shells on CdSe/CdS QDNRs by adjusting the reaction conditions, and durations of up to three weeks were required for fully encapsulating QDNRs with high ARs.⁴⁶ The long reaction times also caused more substantial degradation of the optical properties.⁴⁶ We report a method for and mechanistic understanding of the controlled deposition of lobed and uniform SiO₂ overcoatings onto CdSe/CdS QDNRs with ARs up to 19.1 by controlling the water and SiO₂ precursor concentrations. In our approach, all reactions are completed within a 24-hour period. The major advance is decoupling of the amounts of NH₄OH and water used in the reaction to deposit SiO₂ onto QDNRs. In another recent study, different concentrations of a fixed volume of aqueous NH₄OH were employed,⁴⁷ but we show that independently varying the amount of water provides improved morphological control with short (24-hour) reaction times.

EXPERIMENTAL SECTION

Chemicals. Reagents for synthesizing CdSe/CdS QDNRs are reported in the Supporting Information. The synthesis of SiO₂-QDNRs used tetraethyl orthosilicate (TEOS, 99.9%) from Alfa Aesar, cyclohexane (ACS reagent grade) and saturated ammonium hydroxide (NH₄OH; 28-30 % as NH₃, ACS reagent grade) from Macron Fine Chemicals, deionized (DI) water (ACS reagent grade, ASTM Type I, ASTM Type II) from Ricca Chemical Company, polyoxyethylene (5) nonylphenylether (Igepal CO-520, further abbreviated as CO520) from Sigma-Aldrich, and 2-[methoxy(polyethyleneoxy)₉₋₁₂propyl]trimethoxysilane (PEG-silane, 90%) from Gelest. Toluene and methanol (ChromAR) from Macron Fine Chemicals, and anhydrous ethanol (Koptec) from Decon Labs were used for purification of the QDNRs, SiO₂-QDNRs, and PEGylated SiO₂-QDNRs. Tris(2,2'-bipyridyl)dichlororuthenium(II) hexahydrate (Ru(bpy)₃, 99.95% trace metal basis) from Sigma-Aldrich was used as a reference dye for QY measurements.

CdSe/CdS Quantum Dot Nanorod Synthesis. QDNRs were synthesized following the method reported by Hill *et al.*,³⁵ which scaled up the synthesis reported by Carbone *et al.*²⁹ Complete details for the synthesis and purification of CdSe NPs and

CdSe/CdS QDNRs are provided in the Supporting Information. Spherical CdSe NPs were first synthesized and then templated epitaxial, directional growth of anisotropic CdS shells, resulting in QDNRs. The QDNRs were purified and dispersed in cyclohexane at a concentration of 12 mg/mL. The concentration was measured by removing the cyclohexane from a 0.2 mL aliquot of the QDNR solution and weighing the mass of the dried QDNRs. (The dried QDNRs were disposed of and were not used for conducting SiO₂ overcoating studies.) Based on the measurement, cyclohexane was quantitatively added or removed by evaporation to reach the final concentration of 12 mg/mL. This dispersion was used as a stock solution for the SiO₂ overcoating procedure.

SiO₂ Overcoating. The method for depositing SiO₂ onto CdSe/CdS QDNRs was adapted from previous reports on overcoating hydrophobic spherical PbSe quantum dots with SiO₂.⁴⁹ All SiO₂ overcoating reactions were conducted at room temperature in sealed 20 mL scintillation vials covered with Al foil to minimize exposure to light. The amounts of reactants used in each reaction are provided in the Supporting information, Table S1. QDNRs were dispersed in cyclohexane at a concentration of 2 mg/mL. A TEOS solution was prepared by diluting 0.3 mL of TEOS in 4.7 mL of cyclohexane, unless otherwise specified. These proportions gave a 6% v/v solution, but the volumes of TEOS reported in the figure text overlays and captions correspond to the amounts of neat TEOS added, neglecting the volume of cyclohexane. In another vial, CO520 was stirred vigorously with 10 mL of cyclohexane using a magnetic stir bar for 15 minutes at room temperature. The amount of CO520 was varied (1-2 g), depending on the AR of QDNRs. The dispersion of QDNRs in cyclohexane at a concentration of 2 mg/mL was then added, followed by vigorous stirring for an additional 15 minutes. After adding 60-120 μ L of saturated NH₄OH and, for some experiments, variable amounts of DI water, the mixture was stirred vigorously for another 30 minutes. DI water was added to obtain conformal overcoatings rather than lobed SiO₂-QDNRs, which resulted when water was not added beyond that contained in NH₄OH. TEOS solution was then added to the reverse microemulsion to initiate SiO₂ shell growth. The stirring rate was decreased to gentle agitation, and the vials were capped and stored in the dark, while the reaction continued for an additional 24 hours. For obtaining thinner shells or for functionalization with PEG, SiO₂ shell growth could also be terminated early by adding 40 μ L of neat PEG-silane at different times (ranging from 45 minutes to 16 hours after addition of TEOS),⁴⁴ resulting in PEG-SiO₂-QDNRs. After adding PEG-silane and briefly increasing the stirring rate to ensure mixing, the reaction was allowed to continue with gentle stirring until 24 hours had elapsed after the initial addition of TEOS. For purifying the SiO₂-QDNR or PEG-SiO₂-QDNR products, 1-2 mL of ethanol or methanol was added to break up the microemulsion, and the mixture was centrifuged at 14,140 g for up to 20 minutes to sediment the products. The colorless supernatant was discarded, and the (PEG-)SiO₂-QDNRs were redispersed in 2.5 mL of ethanol, methanol, or DI water. To ensure thorough cleaning, the products were twice centrifuged and redispersed in ethanol, methanol, or DI water.

Transmission Electron Microscopy. The SiO₂ shell thickness and the QDNR dimensions were measured by transmission electron microscopy (TEM) using a JEOL 2000FX microscope operated at an accelerating voltage of 200 kV. Samples were prepared by dropcasting onto Cu TEM grids with ultrathin carbon and Formvar supports.

Optical Characterization. Optical absorbance spectra were acquired using an Ocean Optics USB4000-VIS-NIR spectrophotometer. An Ocean Optics USB4000-FL spectrophotometer equipped with a 455 nm LED was used for emission measurements. All spectra were acquired in a 1 cm path length quartz cuvette. Relative QY measurements were acquired for uncoated QDNRs and SiO₂-QDNRs with ARs of 6.0 and 9.1. Aqueous [Ru(bpy)₃]Cl₂•6H₂O with dissolved atmospheric oxygen was used as a reference for QY measurements, for which a QY of 4.0 ± 0.2% has been reported.^{50,51} QYs were measured immediately after completing SiO₂ shell growth and purification. Optical spectra and TEM images for the samples selected for QY measurements are included in the Supporting Information.

RESULTS AND DISCUSSION

Morphological Effects of TEOS and Water Concentration on SiO₂-QDNRs. The concentrations of TEOS and water are key levers for spatially-controlled deposition of SiO₂ onto QDNRs, which was initially investigated for QDNRs with an average length of 46.3 nm and width of 5.8 nm, giving an AR of 8.0 (Figures 1,2). At a low, constant concentration of water (a volume of 42 μL, obtained from adding 60 μL of NH₄OH), lobed SiO₂ coatings were obtained. The amount of TEOS added determined whether single (15 μL) or double lobes (30 μL) resulted. Throughout this paper, the volume of TEOS is specified as neat TEOS, although the experiments were conducted by adding a solution of TEOS dissolved in cyclohexane, for which the amounts are reported in the Supporting information, Table S1. The single and double lobes have respective average diameters of 30.6 nm and 35.1 nm.

The progression from single-lobed to double-lobed SiO₂-QDNRs by adding more TEOS can be attributed to the nucleation and growth of larger numbers of spherical SiO₂ NPs. The TEOS concentration is known to determine the number of nuclei formed for SiO₂ NPs in the same reverse micelle system in the absence of other kinds of presynthesized NPs.⁵² For small amounts of water, CO520 reverse micelles in cyclohexane are too small to encapsulate entire QDNRs.⁵³ Rather, SiO₂ forms in small reverse micelles that preferentially nucleate and grow at the ends of the QDNRs, presumably due to the higher surface energy at the ends. Small amounts of TEOS give single-lobed SiO₂-QDNRs, while additional nucleation caused by larger amounts of TEOS results in double-lobed SiO₂-QDNRs and can also drive formation of excess spherical SiO₂ NPs (Figure 1b). These observations are consistent a related study, where deposition of SiO₂ was reported to be more favorable on the end of the QDNR containing the CdSe seed, which was attributed to crystal asymmetry in the structure of CdSe/CdS QDNRs.⁴⁶

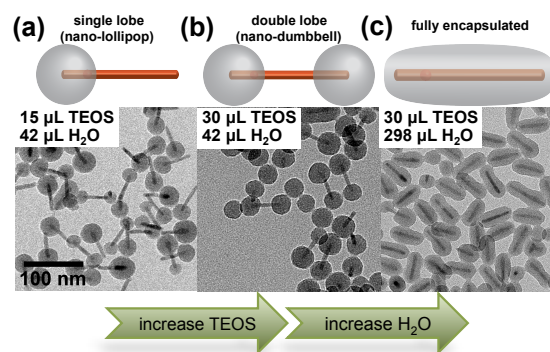


Figure 1. TEM images show morphological control of SiO₂ shells on short CdSe/CdS core/shell QDNRs (AR of 8.0) by varying the amounts of TEOS and water. (a) 15 μL and (b) 30 μL of TEOS give single and double lobes of SiO₂ at the ends of the QDNRs, respectively. (c) Addition of 256 μL of water (giving a total of 298 μL, when combined with 42 μL from NH₄OH) results in fully encapsulated QDNRs.

The uniformity of the SiO₂ shell along the length of the QDNR is determined by the concentration of water, which scales with the amount of water added. Increasing the concentration of water is known to enlarge the reverse micelles,⁵³ and CO520 has been shown to promote formation of cylindrical and lamellar reverse micelles, depending on the water to surfactant ratio.⁵⁴ Adding water likely causes encapsulation of each QDNR within a single reverse micelle, allowing uniform deposition of SiO₂. This is further supported by the observation that full encapsulation of QDNRs of high ARs with SiO₂ requires high water concentrations (see later discussion and Figure 3). In addition to changing the size and shape of the reverse micelles, increased water concentrations also promote shorter SiO₂ growth times by accelerating the rate of hydrolysis of TEOS.⁵⁵

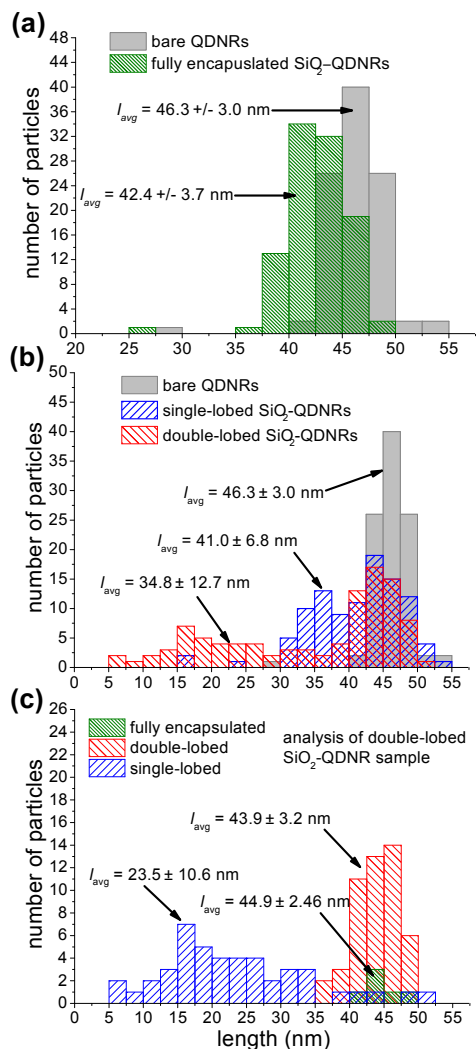


Figure 2. Histograms of length distributions measured by TEM of QDNR cores in the samples presented in Figure 1: (a) fully encapsulated SiO₂-QDNRs, (b) single-lobed and double-lobed SiO₂-QDNRs, and (c) subpopulations of different morphologies within the double-lobed sample.

Etching of QDNR Cores and Breakage of Double-Lobed SiO₂-QDNRs. The distribution of lengths of the QDNR cores before and after SiO₂ overcoating provides important insights about the SiO₂ deposition process. For the fully encapsulated QDNRs and single-lobed samples, the average length after overcoating decreases by 3.9 nm and 5.3 nm, respectively, and the standard deviation in the length more than doubles (Figure 2a,b). The decrease in length and increase in the polydispersity suggest etching of the QDNRs occurs concurrently with SiO₂ deposition. NH₄OH used as a base catalyst for SiO₂ deposition could cause etching.^{56,57}

The length distribution of the double-lobed SiO₂-QDNRs is much broader than for the single-lobed and fully encapsulated SiO₂-QDNRs. To better understand formation of the double-lobed SiO₂-QDNRs, the lengths of each morphology of SiO₂-

QDNR within this sample were tabulated separately (Figure 2c). In addition to double-lobed SiO₂-QDNRs, there is a very small population of fully encapsulated SiO₂-QDNRs and a large number of shorter, single-lobed SiO₂-QDNRs. We attribute these single-lobed SiO₂-QDNRs to the breakage of double-lobed SiO₂-QDNRs during SiO₂ deposition. This explanation is further supported by the absence of short double-lobed SiO₂-QDNRs. Some of the QDNR cores are truncated at the SiO₂/solution interface, and others extend outward from the SiO₂. While the mechanism and timing of breakage are not known, it appears impossible to obtain a pure sample of double-lobed QDNRs due to breakage, though decreasing the AR of the QDNRs or decreasing the size of the SiO₂ lobes may make double-lobed SiO₂-QDNRs less susceptible to breakage.

SiO₂ Overcoating of QDNRs with High ARs. Methods for synthesizing SiO₂-QDNRs with low ARs are well established, but adapting these methods toward uniform SiO₂ overcoating of QDNRs with higher ARs has been challenging.^{45,46} We report morphological control of SiO₂ overcoatings on QDNRs with a high AR of 19.1 by adjusting the amount of water and CO520 (Figure 3). The CO520 concentration was increased to inhibit crosslinking of the QDNRs during overcoating with SiO₂ (see next section). The total amount of water was increased from 298 μL to 576 μL to fully encapsulate QDNRs with lengths of 134.1 nm rather than 46.3 nm. For high-AR QDNRs, low water concentrations still produce lobed structures, but double-lobed structures are more susceptible to breakage during SiO₂ deposition than low-AR QDNRs.

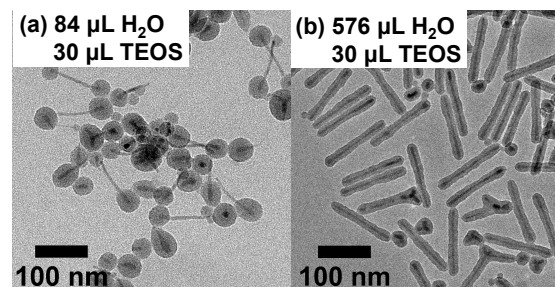


Figure 3. Varying the amount of water during SiO₂ deposition on high-AR QDNRs (initial length of 134.1 nm and AR of 19.1) gives morphological control, shown in TEM images of (a) lobed (84 μL of water) and (b) fully encapsulated SiO₂-QDNRs (576 μL of water).

The amount of TEOS used in the reaction is important for controlling the size of SiO₂ lobes on high-AR SiO₂-QDNRs, which also affects their breakage. For high-AR QDNRs, larger SiO₂ lobes form when increasing the TEOS volume from 30 μL (Figure 3b) to 56.6 μL (Supporting Information, Figure S4). In contrast, for lower-AR QDNRs, increasing the amount of TEOS causes formation of double-lobed SiO₂-QDNRs. The absence of the double-lobed morphology for high-AR QDNRs is again likely caused by a higher rate of breakage, which is consistent with analysis of the QDNR core length distribution (Supporting Information, Figure S5). While double-lobed structures may form during the initial stages of SiO₂ nucleation on the QDNRs, the QDNRs likely break during growth of the SiO₂ lobes. Since breakage occurs after SiO₂ nucleation, the freshly exposed ends of broken QDNRs do not form new SiO₂ lobes, but SiO₂ growth occurs on the preexisting lobes.

Influence of CO520 on SiO₂-QDNR Crosslinking. Decreasing the amount of CO520 causes increased crosslinking between the ends of SiO₂-QDNRs (Figure 4) and does not significantly affect the uniformity of the SiO₂ shells along the length of the QDNRs. Crosslinking at the ends of QDNRs is likely caused by some combination of the high curvature at the ends and the resulting destabilization of the ligand shell on the ends.^{58,59} When reducing the CO520 concentration, CO520 may be deposited preferentially on the sides of the QDNRs, while leaving the ends exposed. The reduced amount of CO520 on the ends of the QDNRs may increase the frequency of interactions between the ends of QDNRs in different reverse micelles. Deposition of SiO₂ encapsulates and preserves the crosslinked network of SiO₂-QDNRs.

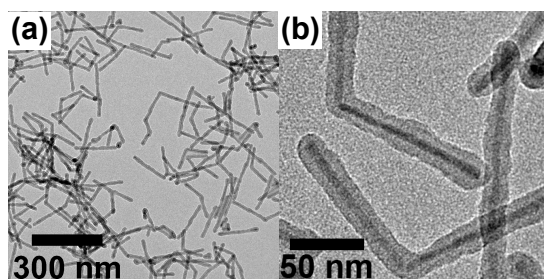


Figure 4. TEM images at (a) low and (b) high magnifications of the same sample of SiO₂-QDNRs prepared with a reduced concentration of CO520, which are crosslinked at their ends.

PEG-Silane Functionalization and SiO₂ Thickness Control. Both thick and thin SiO₂ shells on QDNRs can be beneficial, depending on the application.⁶⁰ Thin SiO₂ shells are useful for maintaining the high AR or for allowing molecular species to more readily diffuse through the shell and interact with the QDNR core. Moreover, SiO₂ shells can serve as spacers with tunable thickness for controlling the distance between the QDNR surface and molecules, other NPs, or surfaces.

One approach for controlling the thickness of ultrathin SiO₂ shells on anisotropic NPs is to reduce the concentrations of TEOS and the base catalyst.^{44,47} Recently, we reported deposition of thin SiO₂ shells through a modified Stöber method on gold nanorods templated by CTAB, which was terminated by adding PEG-silane.⁴⁴ Here, we have added PEG-silane to CdSe/CdS QDNRs in the reverse microemulsion to terminate SiO₂ shell growth. During the typical 24-hour reaction for SiO₂ shell growth, PEG-silane was added at different times after starting SiO₂ shell growth (Figure 5). As expected, addition at earlier times gave thinner shells due to the reduced time for SiO₂ shell growth. Efficient termination of SiO₂ deposition by PEG-silane is attributed to the bulkiness of the PEG moiety, which disrupts crosslinking of the Si-O-Si network. After adding PEG-silane, the mixture becomes slightly cloudy, which may be attributed to increased scattering, if PEG-silane increases the size of the reverse micelles.

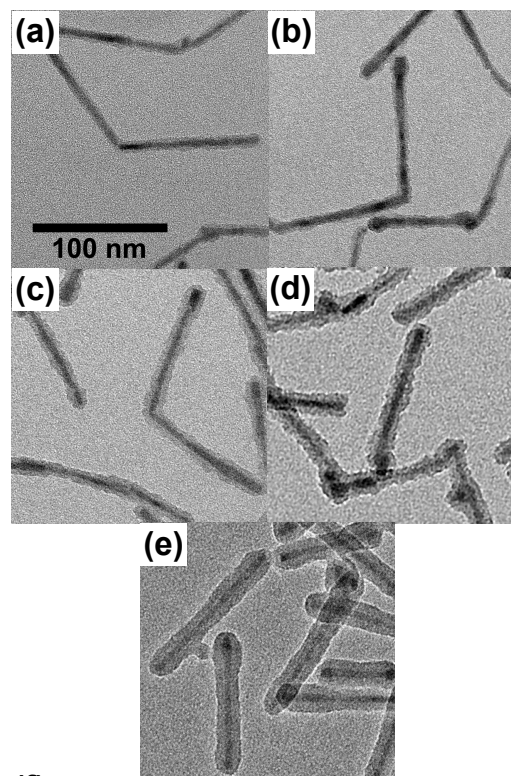


Figure 5. (a-e) Representative TEM images from injection of PEG-silane (a) 1 hour, (b) 3 hours, (c) 10 hours, and (d) 20 hours after addition of TEOS, compared with (e) no injection (24 hours). (f) Dependence of the SiO₂ shell thickness on the PEG-silane injection time. The scale bar in (a) applies to all panels.

The SiO₂ shell growth rate can be measured from the dependence of the shell thickness on the time when PEG-silane was added to the reverse microemulsion. When PEG-silane was added at 1, 3, 10, 16, and 20 hours after adding TEOS, respective SiO₂ shell thicknesses of 1.9, 3.1, 4.2, 5.4, and 7.3 nm were obtained. A SiO₂ shell thickness of 8.2 nm resulted when no PEG-silane was added. The SiO₂ shell thickness has an approximately linear dependence on the time when PEG-silane was added (Figure 5f). In our previous study where deposition of SiO₂ on gold nanorods was terminated by adding PEG-silane,

shell growth occurred quickly initially and then slowed down over time.⁴⁴ In the case of SiO₂-QDNRs, the reverse micelles might slow the reaction by requiring diffusion of TEOS into the reverse micelles from the cyclohexane phase. In contrast, for SiO₂-coated gold nanorods, the reaction was conducted in a common aqueous phase.

Quantum Yield Measurements. The optical properties of QDNRs with ARs of 6.0 and 9.1 were measured before and after SiO₂ overcoating (Figure 6). For an AR of 6.0, the QY decreased from 67.7% before to 48.2% after full SiO₂ encapsulation. For QDNRs with an AR of 9.1, the QY decreased from 55.4% before to 31.2% and 33.9% after full encapsulation and deposition of single lobes, respectively. As expected, the QY is higher for QDNRs of lower AR.²⁹ The ~20% decrease in QY after SiO₂ overcoating is similar to that observed by others after a 1-day duration of SiO₂ shell growth.⁴⁶ Small blueshifts of 1-2 nm were observed in the emission spectra of SiO₂-QDNRs (Supporting Information, Figure S2). Spectral shifts have been observed in other kinds of SiO₂ and QD composite materials and may arise from several factors, including ligand effects if TOPO is displaced by CO520, solvatochromism, the higher refractive index of the SiO₂ shell, and NH₃ etching or oxidation of the CdS shell.^{12,61-63}

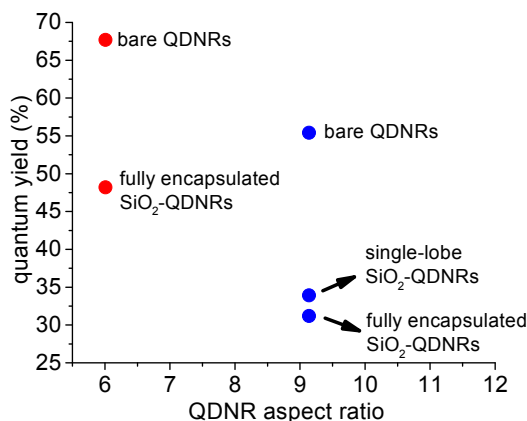


Figure 6. QYs of QDNRs and SiO₂-overcoated QDNRs of different ARs and morphologies.

CONCLUSIONS

Morphological control of SiO₂ overcoatings on CdSe/CdS QDNRs has been demonstrated by independently varying the concentrations of TEOS and water added to reverse micelles. Adding water generally accelerates the rate of SiO₂ deposition and favors full encapsulation rather than lobed structures. This approach may likely be generalized to overcoating other kinds of anisotropically shaped NPs in reverse micelles. Single-lobed, double-lobed, and fully encapsulated SiO₂-QDNRs have been obtained within a 24-hour period. While a typical reduction in QY of ~20% was observed after overcoating, the short reaction duration prevents larger decreases in QY than have been reported for longer reaction times.⁴⁶ Breakage of double-lobed SiO₂-QDNRs was also observed. Addition of PEG-silane provides an additional lever for obtaining thinner the SiO₂ shells by terminating deposition of SiO₂.

ASSOCIATED CONTENT

Supporting Information. Methods for synthesizing CdSe/CdS QDNRs, experimental parameters for all samples of SiO₂-QDNRs, TEM and optical absorbance spectra for selected samples, and length distribution of high-AR SiO₂-QDNRs. This material is available free of charge via the Internet at <http://pubs.acs.org>.

AUTHOR INFORMATION

Corresponding Author

*E-mail: jbracy@ncsu.edu (J.B.T)

ACKNOWLEDGMENTS

This work was supported by the National Science Foundation grant DMR-1056653. The authors acknowledge G. Kalyuzhny (San Diego State University) and J. Bartelme (North Carolina State University) for advice on QDNR synthesis and QY measurements and the use of the Analytical Instrumentation Facility (AIF) at North Carolina State University, which is supported by the State of North Carolina and the National Science Foundation.

REFERENCES

- (1) Liz-Marzán, L. M.; Giersig, M.; Mulvaney, P. Synthesis of Nanosized Gold-Silica Core-Shell Particles. *Langmuir* **1996**, *12*, 4329-4335.
- (2) Guerrero-Martínez, A.; Pérez-Juste, J.; Liz-Marzán, L. Recent Progress on Silica Coating of Nanoparticles and Related Nanomaterials. *Adv. Mater.* **2010**, *22*, 1182-1195.
- (3) Wang, J. S.; Shah, Z. H.; Zhang, S. F.; Lu, R. W. Silica-Based Nanocomposites via Reverse Microemulsions: Classifications, Preparations, and Applications. *Nanoscale* **2014**, *6*, 4418-4437.
- (4) Li, Z.; Barnes, J. C.; Bosoy, A.; Stoddart, J. F.; Zink, J. I. Mesoporous Silica Nanoparticles in Biomedical Applications. *Chem. Soc. Rev.* **2012**, *41*, 2590-2605.
- (5) Wang, H.; Brandl, D. W.; Nordlander, P.; Halas, N. J. Plasmonic Nanostructures: Artificial Molecules. *Acc. Chem. Res.* **2007**, *40*, 53-62.
- (6) Zhang, F.; Braun, G. B.; Shi, Y.; Zhang, Y.; Sun, X.; Reich, N. O.; Zhao, D.; Stucky, G. Fabrication of Ag@SiO₂@Y₂O₃:Er Nanostructures for Bioimaging: Tuning of the Upconversion Fluorescence with Silver Nanoparticles. *J. Am. Chem. Soc.* **2010**, *132*, 2850-2851.
- (7) Brown, L. O.; Doorn, S. K. A Controlled and Reproducible Pathway to Dye-Tagged, Encapsulated Silver Nanoparticles as Substrates for SERS Multiplexing. *Langmuir* **2008**, *24*, 2277-2280.
- (8) Chang, C.-S.; Rothberg, L. J. Plasmon-Enhanced Photoconductivity in Amorphous Silicon Thin Films by Use of Thermally Stable Silica-Coated Gold Nanorods. *Chem. Mater.* **2015**, *27*, 3211-3215.
- (9) Selvan, S. T.; Tan, T. T.; Ying, J. Y. Robust, Non-Cytotoxic, Silica-Coated CdSe Quantum Dots with Efficient Photoluminescence. *Adv. Mater.* **2005**, *17*, 1620-1625.
- (10) Hu, X.; Zrazhevskiy, P.; Gao, X. Encapsulation of Single Quantum Dots with Mesoporous Silica. *Ann. Biomed. Eng.* **2009**, *37*, 1960-1966.
- (11) Zhang, Y.; Wang, M.; Zheng, Y.-G.; Tan, H.; Hsu, B. Y.-W.; Yang, Z.-C.; Wong, S. Y.; Chang, A. Y.-C.; Choolani, M.; Li, X.; Wang, J. PEOlated Micelle/Silica as Dual-Layer Protection of Quantum Dots for Stable and Targeted Bioimaging. *Chem. Mater.* **2013**, *25*, 2976-2985.
- (12) Aubert, T.; Soenen, S. J.; Wassmuth, D.; Cirillo, M.; Van Deun, R.; Braeckmans, K.; Hens, Z. Bright and Stable CdSe/CdS@SiO₂ Nanoparticles Suitable for Long-Term Cell Labeling. *ACS Appl. Mater. Interfaces* **2014**, *6*, 11714-11723.
- (13) Loginova, Y. F.; Dezhurov, S. V.; Zherdeva, V. V.; Kazachkina, N. I.; Wakstein, M. S.; Savitsky, A. P. Biodistribution and Stability of CdSe Core Quantum Dots in Mouse Digestive Tract Following *per os* Administration: Advantages of Double Polymer/Silica Coated Nanocrystals. *Biochem. Biophys. Res. Commun.* **2012**, *419*, 54-59.

- (14) Xiangzhao, A.; Qiang, M.; Xingguang, S. Nanosensor for Dopamine and Glutathione Based on the Quenching and Recovery of the Fluorescence of Silica-Coated Quantum Dots. *Microchim. Acta* **2012**, *180*, 269-277.
- (15) Ma, Y.; Li, Y.; Ma, S.; Zhong, X. Highly Bright Water-Soluble Silica Coated Quantum Dots with Excellent Stability. *J. Mater. Chem. B* **2014**, *2*, 5043-5051.
- (16) Yi, D. K.; Selvan, S. T.; Lee, S. S.; Papaefthymiou, G. C.; Kundaliya, D.; Ying, J. Y. Silica-Coated Nanocomposites of Magnetic Nanoparticles and Quantum Dots. *J. Am. Chem. Soc.* **2005**, *127*, 4990-4991.
- (17) Sathe, T. R.; Agrawal, A.; Nie, S. Mesoporous Silica Beads Embedded with Semiconductor Quantum Dots and Iron Oxide Nanocrystals: Dual-Function Microcarriers for Optical Encoding and Magnetic Separation. *Anal. Chem.* **2006**, *78*, 5627-5632.
- (18) Selvan, S. T.; Patra, P. K.; Ang, C. Y.; Ying, J. Y. Synthesis of Silica-Coated Semiconductor and Magnetic Quantum Dots and their Use in the Imaging of Live Cells. *Angew. Chem., Int. Ed.* **2007**, *46*, 2448-2452.
- (19) Insin, N.; Tracy, J. B.; Lee, H.; Zimmer, J. P.; Westervelt, R. M.; Bawendi, M. G. Incorporation of Iron Oxide Nanoparticles and Quantum Dots into Silica Microspheres. *ACS Nano* **2008**, *2*, 197-202.
- (20) Zrazhevskiy, P.; Sena, M.; Gao, X. Designing Multifunctional Quantum Dots for Bioimaging, Detection, and Drug Delivery. *Chem. Rev.* **2010**, *39*, 4326-4354.
- (21) Chen, O.; Riedemann, L.; Etoc, F.; Herrmann, H.; Coppey, M.; Barch, M.; Farrar, C. T.; Zhao, J.; Bruns, O. T.; Wei, H.; Guo, P.; Cui, J.; Jensen, R.; Chen, Y.; Harris, D. K.; Cordero, J. M.; Wang, Z.; Jasanoff, A.; Fukumura, D.; Reimer, R.; Dahan, M.; Jain, R. K.; Bawendi, M. G. Magneto-Fluorescent Core-Shell Superparticles. *Nat. Commun.* **2014**, *5*, 5093.
- (22) Jun, S.; Lee, J.; Jang, E. Highly Luminescent and Photostable Quantum Dot-Silica Monolith and its Application to Light-Emitting Diodes. *ACS Nano* **2013**, *7*, 1472-1477.
- (23) Cosentino, S.; Liu, P.; Le, S. T.; Lee, S.; Paine, D.; Zaslavsky, A.; Pacifici, D.; Mirabella, S.; Miritello, M.; Crupi, I.; Terrasi, A. High-Efficiency Silicon-Compatible Photodetectors Based on Ge Quantum Dots. *Appl. Phys. Lett.* **2011**, *98*, 221107.
- (24) Rho, W. Y.; Choi, J. W.; Lee, H. Y.; Kyeong, S.; Lee, S. H.; Jung, H. S.; Jung, S.; Sung, Y. E.; Lee, Y. S.; Jun, B. H. Dye-Sensitized Solar Cells with Silica-Coated Quantum Dot-Embedded Nanoparticles Used as a Light-Harvesting Layer. *New J. Chem.* **2014**, *38*, 910-913.
- (25) Xing, G.; Liao, Y.; Wu, X.; Chakraborty, S.; Liu, X.; Yeow, E. K. L.; Chan, Y.; Sum, T. C. Ultralow-Threshold Two-Photon Pumped Amplified Spontaneous Emission and Lasing from Seeded CdSe/CdS Nanorod Heterostructures. *ACS Nano* **2012**, *6*, 10835-10844.
- (26) Sun, L.; Choi, J. J.; Stachnik, D.; Bartnik, A. C.; Hyun, B. R.; Malliaras, G. G.; Hanrath, T.; Wise, F. W. Bright Infrared Quantum-Dot Light-Emitting Diodes through Inter-Dot Spacing Control. *Nat. Nanotechnol.* **2012**, *7*, 369-373.
- (27) Lo, S. S.; Mirkovic, T.; Chuang, C. H.; Burda, C.; Scholes, G. D. Emergent Properties Resulting from Type-II Band Alignment in Semiconductor Nanoheterostructures. *Adv. Mater.* **2011**, *23*, 180-197.
- (28) Coropceanu, I.; Rossinelli, A.; Caram, J. R.; Freyria, F. S.; Bawendi, M. G. Slow-Injection Growth of Seeded CdSe/CdS Nanorods with Unity Fluorescence Quantum Yield and Complete Shell to Core Energy Transfer. *ACS Nano* **2016**, *10*, 3295-3301.
- (29) Carbone, L.; Nobile, C.; De Giorgi, M.; Sala, F. D.; Morello, G.; Pompa, P.; Hytch, M.; Snoeck, E.; Fiore, A.; Franchini, I. R.; Nadasan, M.; Silvestre, A. F.; Chiodo, L.; Kudara, S.; Cingolani, R.; Krahn, R.; Manna, L. Synthesis and Micrometer-Scale Assembly of Colloidal CdSe/CdS Nanorods Prepared by a Seeded Growth Approach. *Nano Lett.* **2007**, *7*, 2942-2950.
- (30) Hu, J.; Li, L.-S.; Yang, W.; Manna, L.; Wang, L.-W.; Alivisatos, A. P. Linearly Polarized Emission from Colloidal Semiconductor Quantum Rods. *Science* **2001**, *292*, 2060-2063.
- (31) Hadar, I.; Hitin, G. B.; Sitt, A.; Faust, A.; Banin, U. Polarization Properties of Semiconductor Nanorod Heterostructures: From Single Particles to the Ensemble. *J. Phys. Chem. Lett.* **2013**, *4*, 502-507.
- (32) Sitt, A.; Hadar, I.; Banin, U. Band-Gap Engineering, Optoelectronic Properties and Applications of Colloidal Heterostructured Semiconductor Nanorods. *Nano Today* **2013**, *8*, 494-513.
- (33) Xing, G.; Chakraborty, S.; Chou, K. L.; Mishra, N.; Huan, C. H. A.; Chan, Y.; Sum, T. C. Enhanced Tunability of the Multiphoton Absorption Cross-Section in Seeded CdSe/CdS Nanorod Heterostructures. *Appl. Phys. Lett.* **2010**, *97*, 061112.
- (34) Menagen, G.; Macdonald, J. E.; Shemesh, Y.; Popov, I.; Banin, U. Au Growth on Semiconductor Nanorods: Photoinduced versus Thermal Growth Mechanisms. *J. Am. Chem. Soc.* **2009**, *131*, 17406-17411.
- (35) Hill, L. J.; Bull, M. M.; Sung, Y.; Simmonds, A. G.; Dirlam, P. T.; Richey, N. E.; DeRosa, S. E.; Shim, I.-B.; Guin, D.; Costanzo, P. J.; Pinna, N.; Willinger, M.-G.; Vogel, W.; Char, K.; Pyun, J. Directing the Deposition of Ferromagnetic Cobalt onto Pt-Tipped CdSe@CdS Nanorods: Synthetic and Mechanistic Insights. *ACS Nano* **2012**, *6*, 8632-8645.
- (36) Baker, J. L.; Widmer-Cooper, A.; Toney, M. F.; Geissler, P. L.; Alivisatos, A. P. Device-Scale Perpendicular Alignment of Colloidal Nanorods. *Nano Lett.* **2010**, *10*, 195-201.
- (37) Hasegawa, M.; Hirayama, Y.; Dertinger, S. Polarized Fluorescent Emission from Aligned Electrospun Nanofiber Sheets Containing Semiconductor Nanorods. *Appl. Phys. Lett.* **2015**, *106*, 051103.
- (38) Gerion, D.; Pinaud, F.; Williams, S. C.; Parak, W. J.; Zanchet, D.; Weiss, S.; Alivisatos, A. P. Synthesis and Properties of Biocompatible Water-Soluble Silica-Coated CdSe/ZnS Semiconductor Quantum Dots. *J. Phys. Chem. B* **2001**, *105*, 8861-8871.
- (39) Kumar, R.; Ding, H.; Hu, R.; Yong, K. T.; Roy, I.; Bergey, E. J.; Prasad, P. N. *In vitro* and *In vivo* Optical Imaging Using Water-Dispersible, Noncytotoxic, Luminescent, Silica-Coated Quantum Rods. *Chem. Mater.* **2010**, *22*, 2261-2267.
- (40) Pan, A.; Wang, S.; Liu, R.; Li, C.; Zou, B. Thermal Stability and Lasing of CdS Nanowires Coated by Amorphous Silica. *Small* **2005**, *1*, 1058-1062.
- (41) Wang, Y.; Niu, S.-H.; Zhang, Z.-J.; Wang, H.-T.; Yuan, C.-W.; Fu, D.-G. Silica Coating of Water-Soluble CdTe/CdS Core-Shell Nanocrystals by Microemulsion Method. *Chin. J. Chem. Phys.* **2007**, *20*, 685-689.
- (42) Hu, X.; Gao, X. Silica-Polymer Dual Layer-Encapsulated Quantum Dots with Remarkable Stability. *ACS Nano* **2010**, *4*, 6080-6086.
- (43) Stöber, W.; Fink, A.; Bohn, E. Controlled Growth of Monodisperse Silica Spheres in the Micron Size Range. *J. Colloid Interface Sci.* **1968**, *26*, 62-69.
- (44) Wu, W.-C.; Tracy, J. B. Large-Scale Silica Overcoating of Gold Nanorods with Tunable Shell Thicknesses. *Chem. Mater.* **2015**, *27*, 2888-2894.
- (45) Xu, Y.; Lian, J.; Mishra, N.; Chan, Y. Multifunctional Semiconductor Nanoheterostructures via Site-Selective Silica Encapsulation. *Small* **2013**, *9*, 1908-1915.
- (46) Pietra, F.; van Dijk-Moes, R. J. A.; Ke, X.; Bals, S.; Van Tendeloo, G.; de Mello Donega, C.; Vanmaekelbergh, D. Synthesis of Highly Luminescent Silica-Coated CdSe/CdS Nanorods. *Chem. Mater.* **2013**, *25*, 3427-3434.
- (47) Hutter, E. M.; Pietra, F.; van Dijk-Moes, R. J. A.; Mitoraj, D.; Meeldijk, J. D.; Donega, C. D.; Vanmaekelbergh, D. Method to Incorporate Anisotropic Semiconductor Nanocrystals of All Shapes in an Ultrathin and Uniform Silica Shell. *Chem. Mater.* **2014**, *26*, 1905-1911.
- (48) Aubert, T.; Palangetic, L.; Mohammadimasoudi, M.; Neyts, K.; Beeckman, J.; Clasen, C.; Hens, Z. Large-Scale and Electroswitchable Polarized Emission from Semiconductor Nanorods Aligned in Polymeric Nanofibers. *ACS Photonics* **2015**, *2*, 583-588.
- (49) Darbandi, M.; Lu, W.; Fang, J.; Nann, T. Silica Encapsulation of Hydrophobically Ligated PbSe Nanocrystals. *Langmuir* **2006**, *22*, 4371-4375.
- (50) Suzuki, K.; Kobayashi, A.; Kaneko, S.; Takehira, K.; Yoshihara, T.; Ishida, H.; Shina, Y.; Oishic, S.; Tobita, S. Reevaluation of Absolute Luminescence Quantum Yields of Standard Solutions Using a Spectrometer with an Integrating Sphere and a Back-

- Thinned CCD Detector. *Phys. Chem. Chem. Phys.* **2009**, *11*, 9850-9860.
- (51) Brouwer, A. M. Standards for Photoluminescence Quantum Yield Measurements in Solution (IUPAC Technical Report). *Pure Appl. Chem.* **2011**, *83*, 2213-2228.
- (52) Bergna, H. E.; Roberts, W. O. *Colloidal Silica: Fundamentals and Applications*. CRC Press: 2005; Vol. 131.
- (53) van der Loop, T. H.; Panman, M. R.; Lotze, S.; Zhang, J.; Vad, T.; Bakker, H. J.; Sager, W. F. C.; Woutersen, S. Structure and Dynamics of Water in Nonionic Reverse Micelles: A Combined Time-Resolved Infrared and Small Angle X-Ray Scattering Study. *J. Chem. Phys.* **2012**, *137*, 044503.
- (54) Chang, C.-L.; Fogler, H. S. Controlled Formation of Silica Particles from Tetraethyl Orthosilicate in Nonionic Water-in-Oil Microemulsions. *Langmuir* **1997**, *13*, 3295-3307.
- (55) Osseo-Asare, K.; Arriagada, F. J. Growth Kinetics of Nanosize Silica in a Nonionic Water-in-Oil Microemulsion: A Reverse Micellar Pseudophase Reaction Model. *J. Colloid Interface Sci.* **1999**, *218*, 68-76.
- (56) Ebothe, J. Behaviour of Sprayed CdS Photoelectrodes Etched with Ammonia Solution. *Semicond. Sci. Technol.* **1990**, *5*, 752-758.
- (57) Zhou, R.; Zhang, Q.; Uchaker, E.; Lan, J.; Yin, M.; Cao, G. Mesoporous TiO₂ Beads for High Efficiency CdS/CdSe Quantum Dot Co-Sensitized Solar Cells. *J. Mater. Chem. A* **2014**, *2*, 2517-2525.
- (58) O'Sullivan, C.; Gunning, R. D.; Sanyal, A.; Barrett, C. A.; Geaney, H.; Laffir, F. R.; Ahmed, S.; Ryan, K. M. Spontaneous Room Temperature Elongation of CdS and Ag₂S Nanorods via Oriented Attachment. *J. Am. Chem. Soc.* **2009**, *131*, 12250-12257.
- (59) Singh, A.; Coughlan, C.; Milliron, D. J.; Ryan, K. M. Solution Synthesis and Assembly of Wurtzite-Derived Cu-In-Zn-S Nanorods with Tunable Composition and Band Gap. *Chem. Mater.* **2015**, *27*, 1517-1523.
- (60) Zhang, X.; Shamirian, A.; Jawaid, A. M.; Tyrakowski, C. M.; Page, L. E.; Das, A.; Chen, O.; Isovich, A.; Hassan, A.; Snee, P. T. Monolayer Silane-Coated, Water-Soluble Quantum Dots. *Small* **2015**, *11*, 6091-6096.
- (61) Leatherdale, C. A.; Bawendi, M. G. Observation of Solvatochromism in CdSe Colloidal Quantum Dots. *Phys. Rev. B* **2001**, *63*, 165315.
- (62) Pan, D.; Wang, Q.; Jiang, S.; Ji, X.; An, L. Synthesis of Extremely Small CdSe and Highly Luminescent CdSe/CdS Core-Shell Nanocrystals via a Novel Two-Phase Thermal Approach. *Adv. Mater.* **2005**, *17*, 176-179.
- (63) Frederick, M. T.; Weiss, E. A. Relaxation of Exciton Confinement in CdSe Quantum Dots by Modification with a Conjugated Dithiocarbamate Ligand. *ACS Nano* **2010**, *4*, 3195-3200.

Supporting Information:

**Silica Overcoating of CdSe/CdS Quantum Dot Nanorods with
Controlled Morphologies**

Bryan D. Anderson, Wei-Chen Wu, and Joseph B. Tracy*

Department of Materials Science and Engineering, North Carolina State University, Raleigh,
North Carolina 27695, United States

Synthesis of CdSe/CdS Quantum Dot Nanorods

Chemicals. Tri-*n*-octylphosphine (min. 97%, TOP) and trioctylphosphine oxide (99%, TOPO) from Strem Chemicals, *n*-hexadecylphosphonic acid (>99%; HDP), *n*-hexylphosphonic acid (>99%, HPA), and *n*-octadecylphosphonic acid (>99%, ODP) from PCI Synthesis, and CdO (99.999% metals basis), Se powder (200 mesh, 99.999% metals basis) and S pieces (99.999%) from Alfa Aesar were used to synthesize CdSe/CdS quantum dot nanorods (QDNs).

Preparation of TOP-S and TOP-Se. Complexes of TOP with Se and S (TOP-Se and TOP-S) were prepared in a nitrogen glovebox by adding Se and S, respectively, to TOP. For preparing TOP-Se, 1.16 g (14.7 mmol) of Se powder was added to 8.66 mL (19.4 mmol) of TOP. For preparing TOP-S, 0.6 g (18.7 mmol) of S powder was added to 18 mL (40.4 mmol) of TOP. Both mixtures were stirred overnight, allowing the powders to completely dissolve.

Synthesis and Purification of Spherical CdSe Nanoparticles. 15 g (38.8 mmol) of TOPO, 1.4 g (4.2 mmol) of ODP, and 0.30 g (2.3 mmol) of CdO powder were combined in a 100 mL, three-necked, round-bottomed flask. The mixture was heated under vacuum to 150 °C for 1 hour while stirring with a magnetic stir bar at approximately 300 rpm. The flask was then backfilled with nitrogen and heated to 300 °C, causing the mixture to become transparent and nearly colorless. 7.5 g (20.2 mmol) of TOP was quickly injected by syringe before increasing the temperature of the solution to 365 °C at a rate of 10 °C/min. While leaving the flask on the heating mantle, the heat was turned off, causing slow cooling of the flask. When the solution reached a temperature of 355 °C, 2.15 mL of the TOP-Se solution was quickly injected. After growth of the seeds for 20-60 seconds (shorter times for smaller sizes and longer times for larger sizes), the heating mantle was removed. Cooling was further accelerated using different methods for different temperature ranges: From 355 °C to 290 °C, cool air was blown (heat gun, with the heat turned off) over the surface of the reaction flask. From 290 °C to 150 °C, the outer surface was gently sprayed with acetone. At 200 °C, 20 mL of toluene was added dropwise. From 150 °C to 65 °C, the reaction flask was placed, while stirring, in a stirred room-temperature water bath. Once the mixture reached 65 °C, the solution was divided among four 50-mL centrifuge tubes. 20 mL of ethanol or methanol was added to each centrifuge tube to flocculate the CdSe nanoparticles, followed by centrifugation at 6,880 g for 5 min. The supernatant was decanted, and the CdSe nanoparticles were redispersed in 5-10 mL of toluene. After adding 10-20 mL of ethanol or methanol and centrifuging the mixture, the supernatant was discarded. The CdSe nanoparticles from all four centrifuge tubes were combined in a single 50-mL centrifuge tube after redispersing each fraction in 1-2 mL of toluene. After adding ethanol or methanol and performing a final round of centrifugation, the sedimented CdSe nanoparticles were transferred with a metal spatula into a small glass vial outfitted with a septum cap for further drying overnight under vacuum on a Schlenk line. Once completely dry, the vial was backfilled with nitrogen and transferred into a nitrogen glove box.

Seeded Growth of CdSe/CdS Quantum Dot Nanorods. A dispersion of CdSe nanoparticles in TOP-S was prepared to initiate growth of CdSe/CdS QDNs upon injection into a growth solution. The mass of CdSe nanoparticles (weighed as a powder in the previous step) varied, depending on their size and the desired length of the QDNs, based on guidelines provided by Hill, *et al*, Ref. 35 in the main text. The chosen mass of CdSe seeds was weighed in powdered form and transferred into a 20 mL vial in the glovebox, to which 18 mL of TOP-S solution was added. The vial was tightly sealed and was removed from the glovebox for vigorous

magnetic stirring and sonication, before returning the vial to the glovebox and loading 9.0 mL into a syringe for injection into the solution for growth of CdSe/CdS QDNRs.

CdSe/CdS QDNRs were synthesized by combining 15 g (38.8 mmol) of TOPO, 1.45 g (4.3 mmol) of ODPA, 0.375 g (2.9 mmol) of CdO, and 0.40 g (2.4 mmol) of HPA in a 100 mL three-necked, round-bottomed flask. The mixture was heated under vacuum at 150 °C for 1 hour while stirring with a magnetic stir bar at approximately 300 rpm. The flask was then backfilled with nitrogen and heated to 355 °C. During heating, the mixture became transparent and nearly colorless. 7.5 g (20.2 mmol) of TOP was injected into the flask. After the temperature returned to 355 °C, the temperature was held at 355 °C for 25 minutes. The flask was then wrapped with glass wool while holding the temperature at 355 °C for an additional 5 minutes. Immediately prior to injection of the CdSe nanoparticles, full power was applied to the heating mantle. 9.0 mL of the CdSe nanoparticles dispersed in TOP-S was quickly injected, and the temperature returned to 355 °C within 2 minutes. The solution was heated for a total of 6 minutes after injection for growth of CdSe/CdS QDNRs. The insulating wool and heating mantle were then removed, and toluene was added after cooling to 70 °C to prevent solidification of the mixture. After cooling to room temperature, the mixture was divided equally among four 50-mL centrifuge tubes. 10 mL of ethanol was added to each tube, followed by centrifugation at 4160 g for 7 minutes. After decanting the supernatant, the CdSe/CdS QDNRs from all four centrifuge tubes were combined in a single 50-mL centrifuge tube after redispersing each fraction in 2-3 mL of toluene. Two additional purification cycles were performed by adding 5 mL of ethanol and centrifuging. Between cycles, the sedimented product was redispersed in 4 mL of toluene, but after the final cycle, the sedimented product was redispersed in cyclohexane. Methanol can also be used to drive flocculation of the product for centrifugation, but if methanol is used, a final rinse with ethanol is then performed to ensure miscibility of the small amount of residual solvent with cyclohexane.

TEM Images of CdSe Quantum Dots and CdSe/CdS Quantum Dot Nanorods

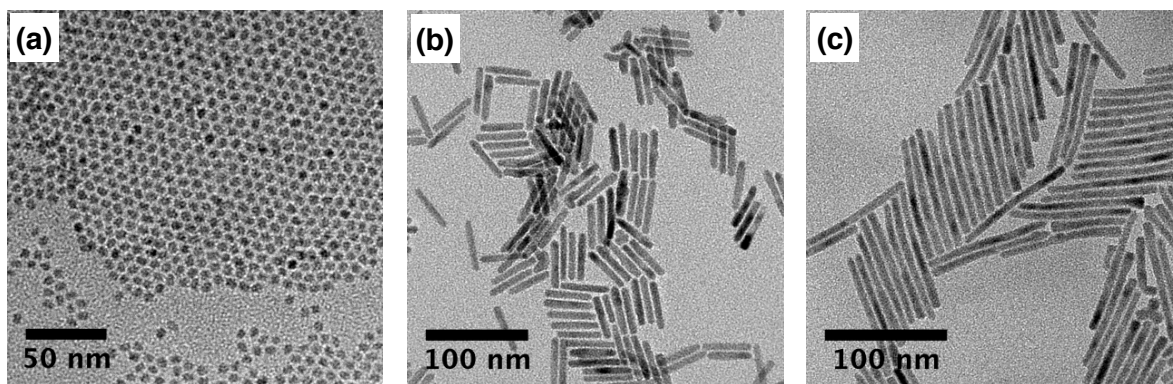


Figure S1. TEM images of (a) typical CdSe QD seeds and CdSe/CdS QDNRs with average lengths of (b) 50 nm and (c) 101 nm.

Experimental Parameters for Synthesizing SiO₂-Overcoated CdSe/CdS Quantum Dot Nanorods

Figure	Aspect Ratio	Relative Quantum Yield (%)	Morphology	Uncoated QDNR Average Length (nm)	Amount of TEOS Diluted in 4.7 mL of Cyclohexane (mL)	Volume of TEOS Solution Added to Reaction (mL)	Resulting Volume of TEOS (μ L)	Volume of NH ₄ OH (μ L)	Additional Water Added (μ L)	Total Water in System (μ L)	Mass of Igepal CO520 (g)	Volume of QDNR Solution at 2 mg/mL (μ L)	Volume of Cyclohexane (mL)
Fig. 1a	8.0		single lobe	46.3	0.3	0.25	15	60	0	42	1.06	600	10
Fig. 1b	8.0	-	double lobe	46.3	0.3	0.5	30	60	0	42	1.06	600	10
Fig. 1c	8.0	37.4	fully encapsulated	46.3	0.3	0.5	30	60	256	298	1.06	600	10
Fig. 3a	19.1	-	single lobe	134.1	0.3	0.5	30	60	42	84	1.968	1000	10
Fig. 3b	19.1	-	fully encapsulated	134.1	0.3	0.5	30	60	534	576	1.968	1000	10
Fig. S4	19.1	-	lobed	134.1	0.6	0.5	56.6	60	42	84	1.968	1000	10
Figs. 4,5	14.8	-	fully encapsulated	102.1	0.3	0.5	30	120	534	570	1.06	1020	10
Fig. 6	9.1	33.9	single lobe	58.9	0.3	0.5	30	120	100	184	1.06	1020	10
Fig. 6	9.1	31.2	fully encapsulated	58.9	0.3	0.7	42	120	534	618	1.968	1020	10
Fig. 6	6.0	48.2	fully encapsulated	40.3	0.3	0.5	30	60	256	298	1.26	900	10

Table S1. Parameters for synthesizing fully encapsulated and lobed SiO₂-QDNRs with different aspect ratios.

Optical Emission Spectra Before and After SiO₂ Overcoating

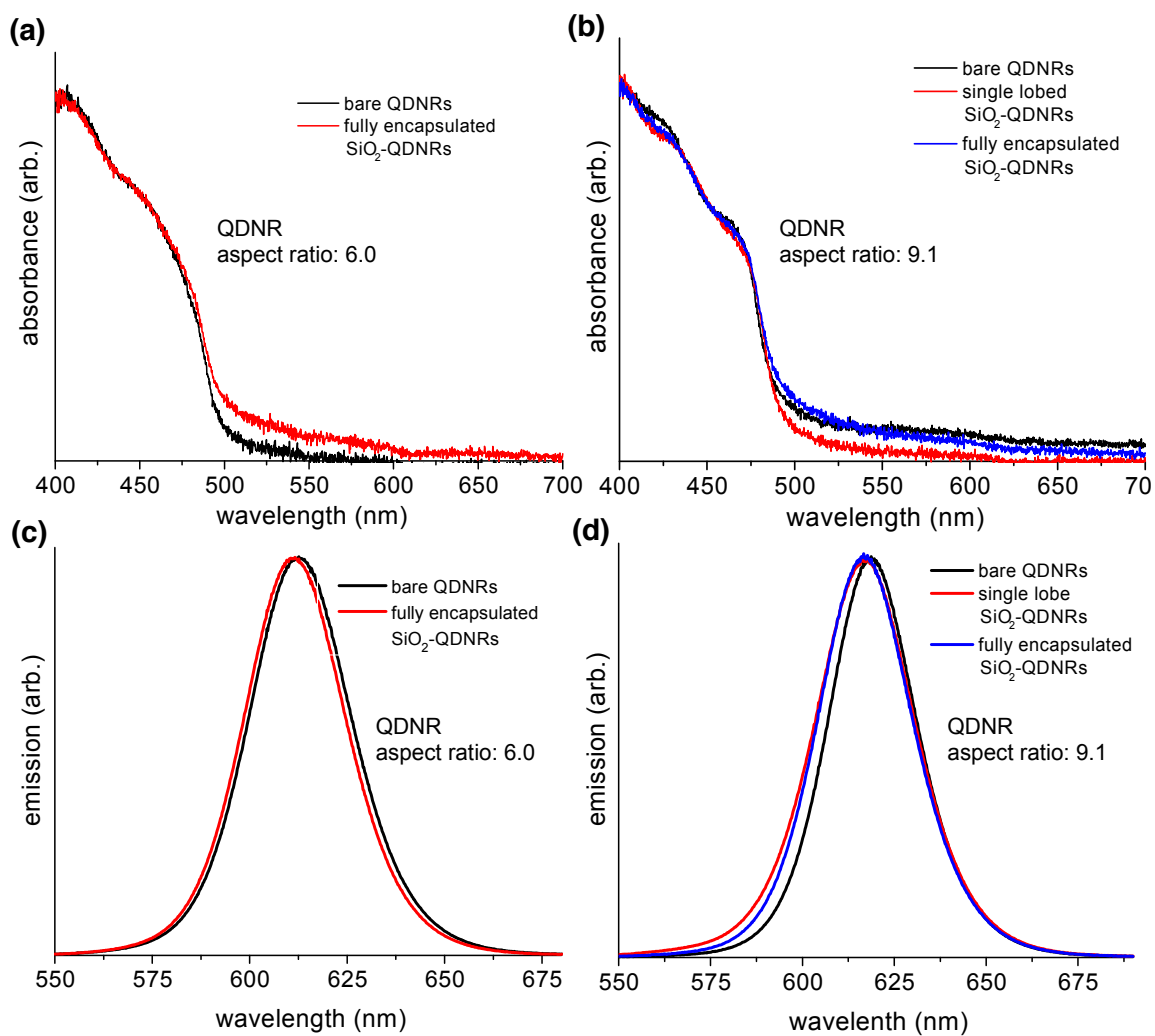


Figure S2. Normalized optical (a,b) absorbance spectra and (c,d) emission spectra of QDNRs and SiO₂-QDNRs reported in Figure 6 with aspect ratios of (a,c) 6.0 and (b,d) 9.1.

TEM Images of CdSe/CdS Quantum Dot Nanorod Samples Before and After Overcoating Used for Quantum Yield Measurements (Figure 6)

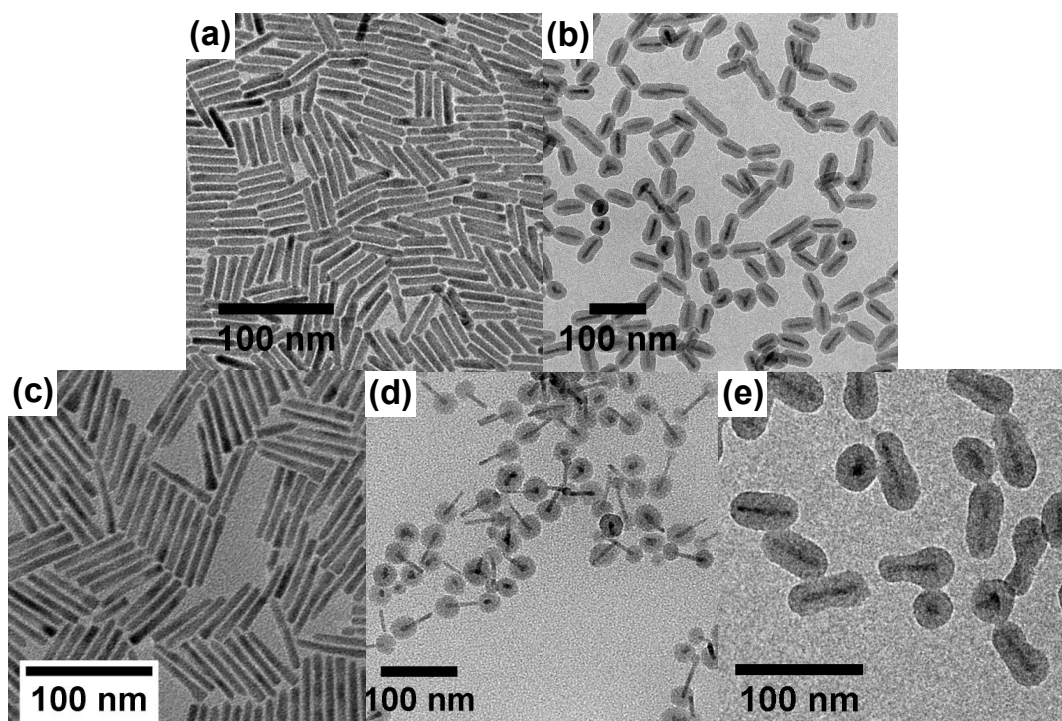


Figure S3. TEM images of the samples presented in Figure 6: (a) QDNRs with an AR of 6.0 were used to synthesize (b) fully encapsulated SiO₂-QDNRs. (c) QDNRs with AR of 9.1 were used to synthesize (d) single-lobed SiO₂-QDNRs and (e) fully encapsulated QDNRs.

TEM Image of CdSe/CdS Quantum Dot Nanorods of High Aspect Ratio (19.1) with Large Lobes Obtained When Increasing the Amount of TEOS (Comparison with Figure 3a)

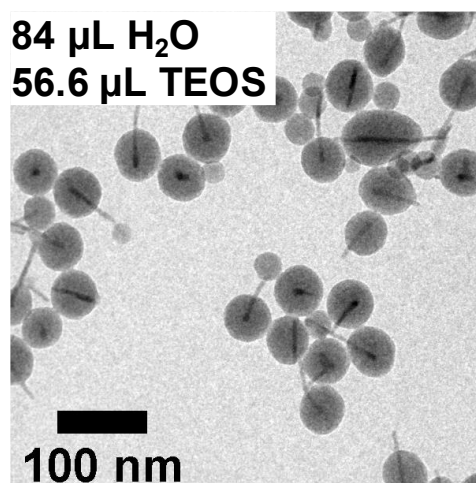


Figure S4. Asymmetric, lobed SiO₂ overcoatings on QDNRs with an initial length of 134.1 nm and an AR of 19.1.

Length Distribution of Lobed and Fully-Encapsulated CdSe/CdS Quantum Dot Nanorods of High Aspect Ratio (19.1)

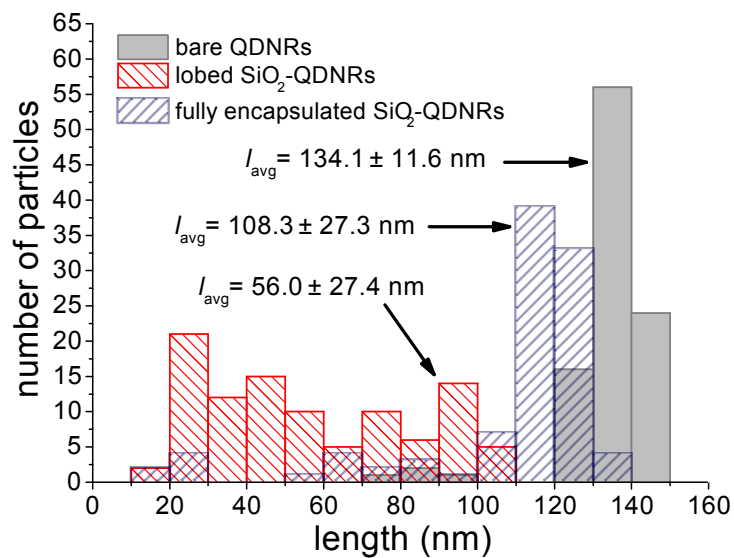


Figure S5. Histogram of length distribution measured by TEM for SiO₂-QDNRs presented in Figure 3a, synthesized using 30 μ L of TEOS. The initial length of the bare QDNR was 134.1 nm (AR of 19.1).

CHAPTER 5: Synthesis of Fe₃O₄-SiO₂-QDNR Nanocomposites

5.1 Introduction

Composite NPs are a relatively new classification of materials that have potential in many different types of applications.^{1,2} NP composites that contain more than one functional component can be beneficial in the sense that it can give rise to multifunctionality. This is particularly useful in the biomedical discipline where there is a need for multifunctional nanoparticles in multimodal imaging and theranostic applications.³

There have been some efforts in incorporating quantum dots with magnetic NPs using a SiO₂ matrix to result in multimodal NP composites that luminescent and magnetically responsive.^{2,4,5} However, fabrication of such nanocomposites with anisotropic morphologies has been limited to date. We have extended this area of research by fabricating magnetic NP and quantum dot composites with controlled anisotropy in nanocomposite structure by employing CdSe/CdS QDNRs as templates to impart an overall anisotropic morphology in the NP composites. We report in the fabrication of Fe₃O₄-SiO₂-QDNR nanocomposites using two different methods. The first approach is the solvothermal decomposition of Fe(acac)₃ in the presence of SiO₂-QDNRs. The second approach is through ligand crosslinking of surface functionalized presynthesized Fe₃O₄ NPs and SiO₂-QDNRs.

5.2 Experimental Details

5.2.1 Chemicals

Reagents for synthesizing CdSe/CdS QDNRs. A comprehensive list of chemicals used for synthesizing QDNRs is listed in Chapter 4.

Reagents for synthesizing SiO₂-QDNRs. A comprehensive list of chemicals used for synthesizing SiO₂-QDNRs is listed in Chapter 4.

Reagents for synthesizing Fe₃O₄-SiO₂-QDNRs by ligand crosslinking. 3-aminopropyltriethoxysilane (APS, ≥98%, Sigma), 2-Bromo-2-methyl-propionic acid (BMPA, 98%, Alfa Aesar), citric acid (ACS, >99.5%, Alfa Aesar), and N,N-dimethylformamide (DMF, 99.9%, EMD Millipore)

Reagents for synthesizing Fe₃O₄-SiO₂-QDNRs by thermal decomposition.

iron (III) acetylacetonate (Fe(acac)₃, 98%, Strem Chemicals), benzyl ether (, 99%, Sigma-Aldrich), oleylamine (97%, Acros).

5.2.2 Nanoparticle synthesis

Synthesis of CdSe/CdS QDNRs. CdSe/CdS QDNRs were synthesized using previous reported methods.^{6, 7} Specific details of the procedures for synthesizing QDNRs were also discussed in Chapter 4.

Synthesis of SiO₂-QDNRs. SiO₂-QDNRs were synthesized using the methods discussed in Chapter 4.

Synthesis of Fe₃O₄ NPs. The synthesis of oleylamine stabilized Fe₃O₄ NPs was adapted from a method reported by Xu *et al.*⁸ The synthesis was conducted on Schlenk line equipped with a vacuum line and N₂ supply. Fe(acac)₃ was dissolved in 15 mL of oleylamine in a three-neck round bottom flask. The solution was heated to 110 °C for 1 hour under N₂ to evaporate atmospheric water. The solution was then heated to 300 °C at a temperature ramp rate of 20

°C/min and aged for 1 hour once the target temperature was reached. Purification of the NPs from the stock solution was performed by adding 50 mL of ethanol. The particles were precipitated by centrifuging at 4,160 g for 5 minutes. Hexanes were added to redisperse the particles to complete one cycle of purification. The purification procedure was conducted a total of three cycles. On the last cycle, instead of added hexanes to redisperse the NPs, chloroform was added.

Synthesizing Fe₃O₄-SiO₂-QDNRs by ligand crosslinking. The synthesis of Fe₃O₄-SiO₂-QDNRs was adapted from the method reported by Lee *et al.*⁹ The surface of the SiO₂-QDNRs were functionalized with APS by dispersing 0.1 mg of SiO₂-QDNRs in 10 mL of ethanol. The solution was then heated to 70 °C, under gentle stirring, in an oil bath for three hours to hydrolyze the SiO₂ surface. 40 µL of APS was then added. The solution was removed from the heated bath and allowed to react for 30 minutes under gentle stirring. The APS functionalized SiO₂-QDNRs were precipitated by centrifuging at 14,140 g for 5 minute. The supernatant was decanted and the particles were dispersed in 5 mL of ethanol.

Ligand exchange was performed on the oleylamine stabilized Fe₃O₄ NPs was performed where oleylamine was exchanged with BMPA. 0.5 g of BMPA and 0.5 g of citric acid was dissolved in 5.5 mL of chloroform and 7.5 mL of DMF and stirred until the powder dissolved into solution. 2 mL of Fe₃O₄ NP solution, where the NP concentration was 7.5 mg/mL, was added to the BMPA and citric acid solution. The solution was heated to 30 °C and was stirred for 8 hours to complete the ligand exchange process. The NPs were purified by centrifuging the NP stock solution at 14,140 g for 3 minutes. The supernatant was

decanted, 5 mL of ethanol was added to the precipitate, and the solution was vortexed and sonicated to disperse the Fe₃O₄ NPs.

The Fe₃O₄-SiO₂-QDNR composite NPs were synthesized by diluting 0.5 mL of the APS functionalized SiO₂-QDNRs with 5 mL of ethanol stirred at a moderate rate. 1 mL of the BMPA functionalized Fe₃O₄ NPs were added dropwise to the SiO₂-QDNR solution to react the particles to form the composite NPs.

Synthesizing Fe₃O₄-SiO₂-QDNRs by solvothermal decomposition. 20 mg of SiO₂-QDNRs were dispersed in 10 mL of benzyl ether. A mixture of 10 mL of oleylamine, 10 mL of benzyl ether, and 0.02 g of Fe(acac)₃ was prepared in a three-neck, round bottom flask. The SiO₂-QDNR solution was added to the three-neck flask and, using a Schlenk line equipped with a vacuum line and a nitrogen supply line, the solution was stirred at a moderate rate using a 1 inch magnetic stir bar and was degassed at room temperature by applying a vacuum. The flask was backfilled with N₂ and heated to 120 °C for 30 minutes to dehydrate and evaporate methanol from the solution. The solution was then heated to 290 °C at a temperature ramp rate of 1 °C/min and aged for 30 minutes once the target temperature was reached. After aging, the heating mantle was removed and the solution was cooled to room temperature. To purify the NPs, 10 mL of ethanol was added and the solution was centrifuged at 14,140 g for 3 minutes to precipitate the NPs. The supernatant was discarded and a 1:1 volume ratio of ethanol:hexanes was added to the precipitate and the solution was vortexed and sonicated to suspend the NPs. The NPs were vortexed and sonicated then

centrifuged again. The last procedure was repeated one more time and hexanes were used as the final solvent to disperse the NPs.

5.2.3 Structural characterization

Structural characterization of the composite NPs was conducted by transmission electron microscopy (TEM). A JEOL 2000FX microscope operated at an accelerating voltage of 200kV was used. Samples were prepared by dropcasting NPs dispersed in ethanol onto Cu TEM grids with ultrathin carbon and Formvar supports.

5.2.4 Optical characterization

Optical absorbance spectra were acquired using an Ocean Optics USB4000-VIS-NIR spectrophotometer. Emission spectra were acquired using an Ocean Optics USB4000-FL spectrophotometer with a 455 nm LED as the excitation source. All spectra were acquired in a 1 cm path length quartz cuvette.

5.3 Results and Discussions

The surfaces of SiO₂-QDNRs were decorated with Fe₃O₄ NPs by solvothermal decomposition of Fe(acac)₃ (**Figure 1**). There have been some reports where magnetic NPs were overcoated with silica, however reports of growing magnetic nanoparticles on the surface of SiO₂ NPs has been limited.^{2, 4, 10} The SiO₂ surface in my study served as a preferential nucleation site for the growth of the iron oxide NPs. A relative high density of

Fe₃O₄ NPs formed on the surface of the SiO₂-QDNRs. The SiO₂-QDNRs remained relatively intact in the high temperature environment that was required to synthesize the Fe₃O₄ NPs.

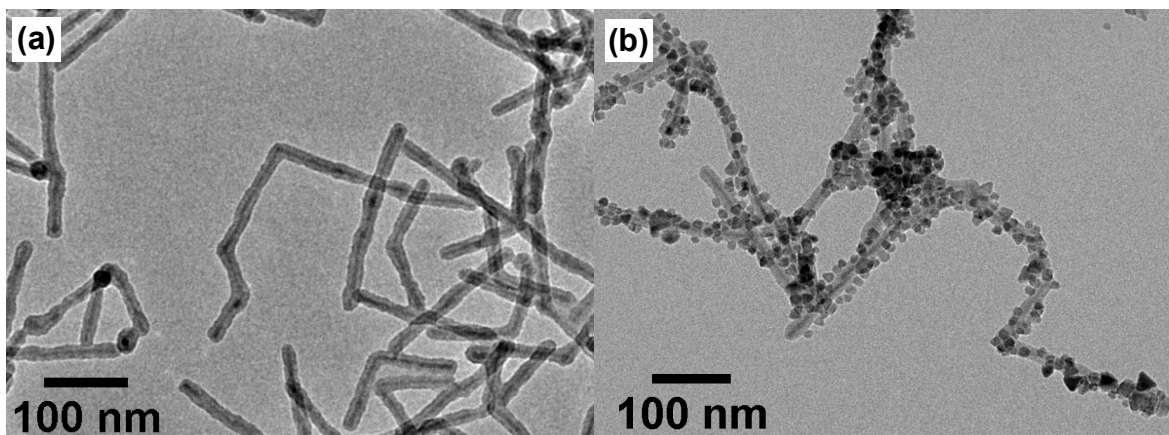


Figure 1. TEM images of (a) SiO₂-QDNRs used in the synthesis of (b) Fe₃O₄-SiO₂-QDNRs produced by thermal decomposition of Fe(acac)₃.

The thermal stability of the SiO₂-QDNRs were studied. The thermal stability of the SiO₂-QDNRs were of interest because the properties of the decomposition of the QDNRs from the high temperatures required for the growth of Fe₃O₄ NPs could result in morphological and optical changes of the QDNR. To test the thermal stability of the SiO₂-QDNRs, a solution of SiO₂-QDNRs dispersed in benzyl ether and oleylamine and was heated to 290 °C. Fe(acac)₃ was intentionally omitted the reaction since the formation of the Fe₃O₄ NPs interfere with the optical absorbance and fluorescence measurements of the QDNRs. Representative data for the heat treatment of the particles shows that there is significant structural damage to the NPs from the high temperature environment (**Figure 2**). The CdSe/CdS QDNR core in some instances are etched from the SiO₂ shell (**Figure 2a**). While

many of the particles do remain intact, TEM shows in many individual particles that the CdSe/CdS core is significantly damaged from etching. In many instances, the QDNR is completely dissolved from the SiO₂ shell. There are some reports that show that that an SiO₂ shell protects and stabilizes the NP core from thermal degradation.¹¹ The thermal stability of the QDNR from the SiO₂ shell can be a result of several factors, including the possibility that SiO₂ has a higher melting point and better mechanical rigidity than the QDNR. However, preexisting structural defects in the SiO₂ shell likely allowed benzyl ether and oleylamine to interact with the QDNR and is likely the reason for damage to some of the SiO₂-QDNRs. In other cases, the morphological integrity of the SiO₂ shell and the QDNR is not preserved post heat treatment (**Figure 2b**). The SiO₂ shell will fuse with neighboring NPs and the QDNR core becomes spherical.

Absorbance and fluorescence were acquired for heat treated samples of the SiO₂-QDNRs. Optical integrity of the SiO₂-QDNRs is also compromised from the heat treatment in benzyl ether and oleylamine at 290 °C (**Figure 2c and 2d**). The absorbance spectra for the QDNRs were normalized at 400 nm and the emission spectra were normalized at the peak of highest emission intensity. There is no significant shifts in the absorbance spectra. The emission spectra of the SiO₂-QDNRs before and after heat treatment is 618 nm and 614 nm, respectively. Additionally, the emission peak broadens after the heat treatment. The blue shifting and broadening of the emission peak is likely from the CdS shell oxidizing during the etching process. There is a significant decrease in the emission intensity of the SiO₂-QDNRs after treatment (**Figure 3**). The significant decrease in the emission of the

SiO₂-QDNRs is indicative of structural damage to the CdS shell which is forming surface traps that result in non-radiative decay pathways of the exciton.

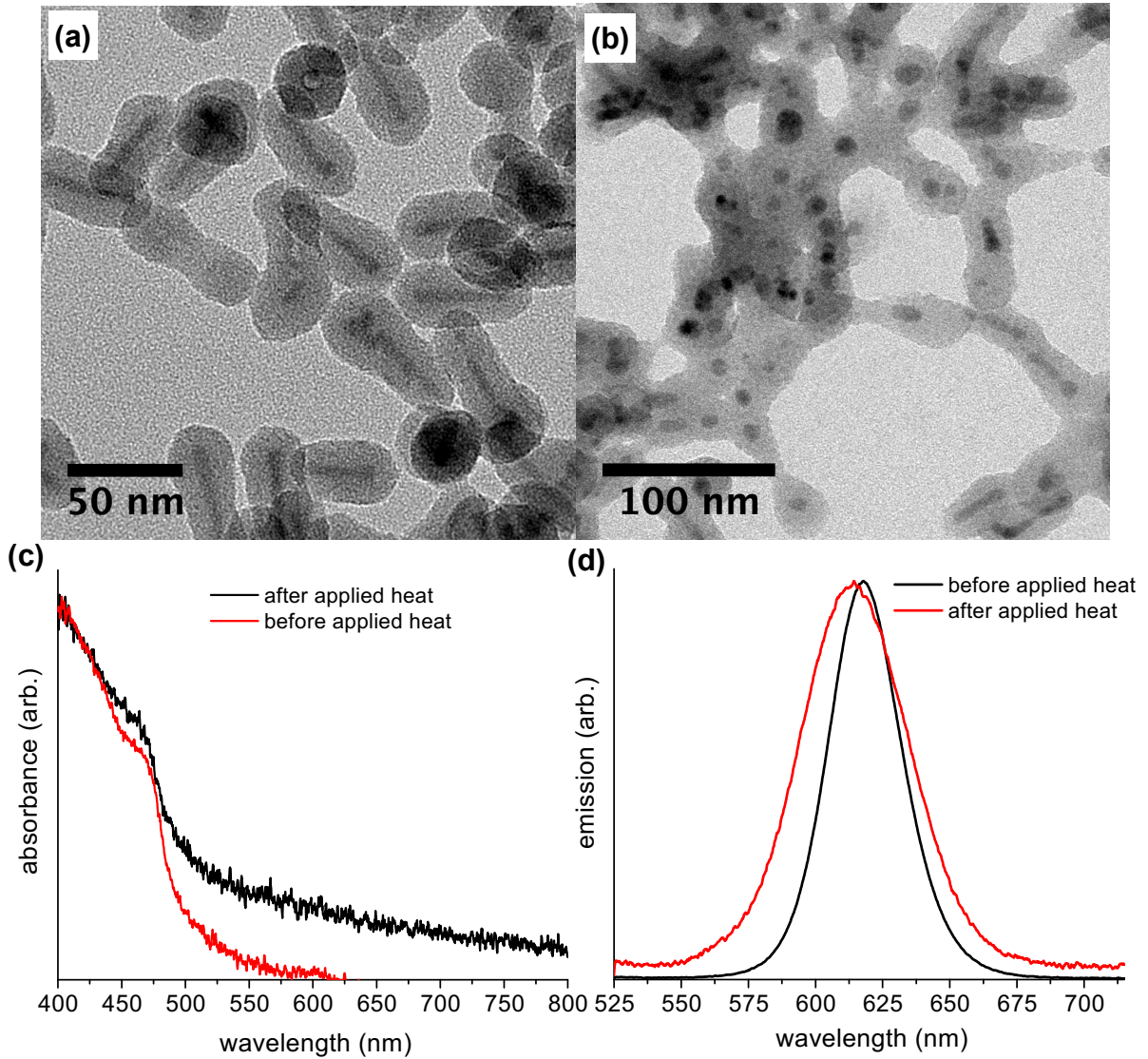


Figure 2. Heat treatment of SiO₂-QDNRs. (a-b) are TEM images of the SiO₂-QDNRs post heat treatment in benzyl ether and oleylamine at 290 °C. Normalized optical (c) absorbance spectra and (d) emission spectra.

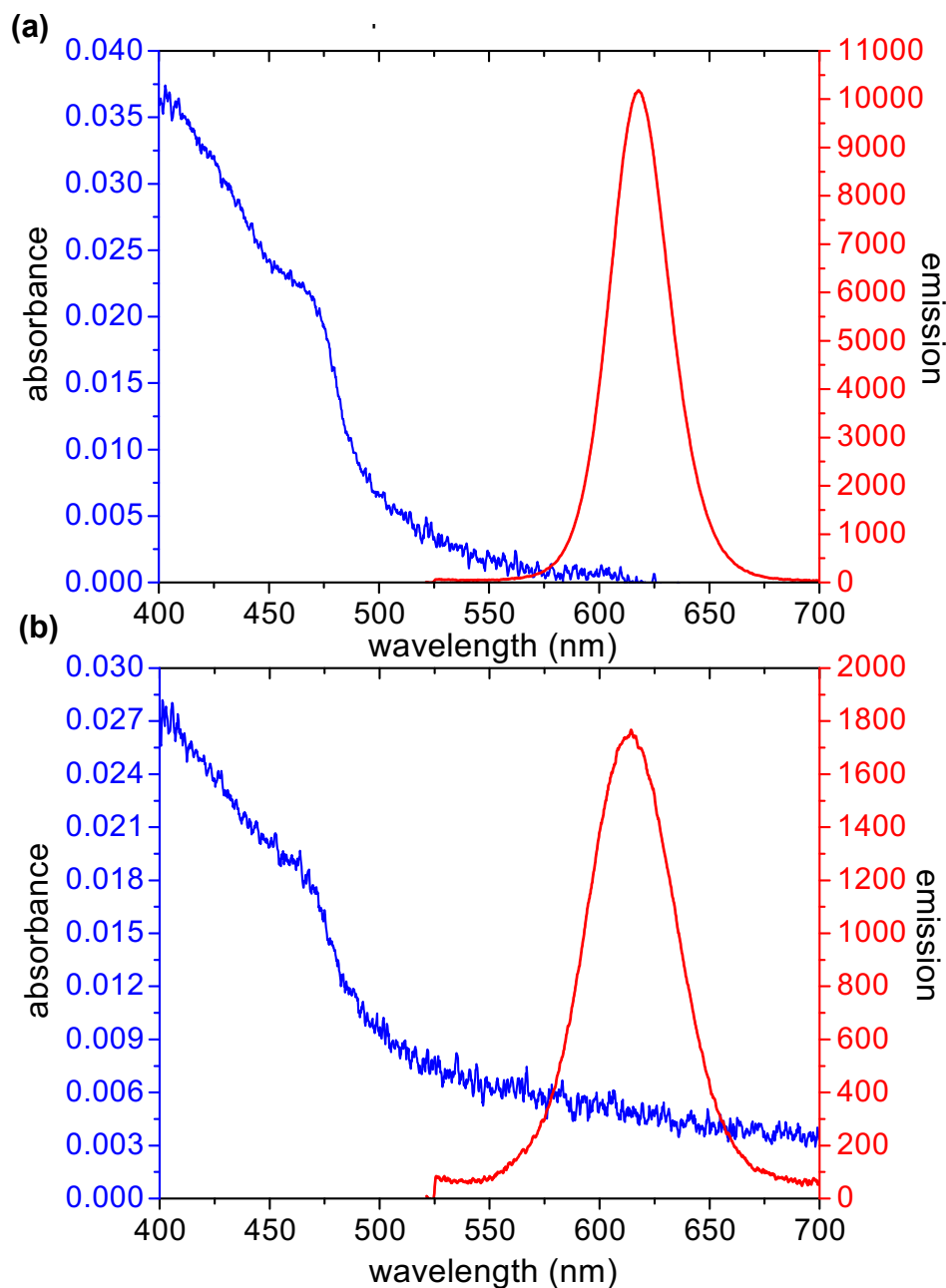


Figure 3. Optical absorbance and emission spectra of SiO₂-QDNRs (a) before and (b) after heat treatment in benzyl ether and oleylamine at 290 °C.

To circumvent the damage to the QDNRs during the high temperature growth of Fe₃O₄ NPs on the surface of SiO₂-QDNRs, a low temperature approach was used for the

synthesis $\text{Fe}_3\text{O}_4\text{-SiO}_2\text{-QDNRs}$. This approach made use of presynthesized, oleylamine stabilized Fe_3O_4 NPs and $\text{SiO}_2\text{-QDNRs}$. The surface of the Fe_3O_4 NPs were functionalized with BMPA through partial ligand exchange with the native oleylamine ligands on the NPs and the surface of the $\text{SiO}_2\text{-QDNRs}$ were modified with APS by silane coupling between the silane headgroup on APS and the SiO_2 shell. Through nucleophilic substitution reaction between the bromine functional groups of BMPA and the amine groups of APS, Fe_3O_4 NPs were assembled on the surface of $\text{SiO}_2\text{-QDNRs}$ (**Figure 4**).

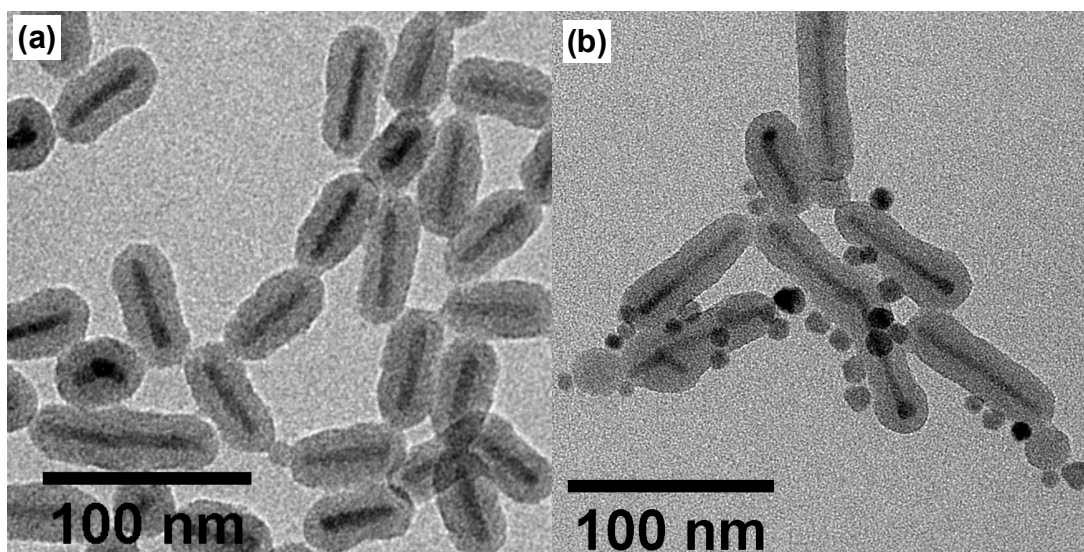


Figure 4. TEM images of (a) $\text{SiO}_2\text{-QDNRs}$ used in the synthesis of (b) $\text{Fe}_3\text{O}_4\text{-SiO}_2\text{-QDNRs}$ produced by ligand crosslinking.

5.4 Conclusions

Surface functionalization of $\text{SiO}_2\text{-QDNRs}$ with Fe_3O_4 NPs by two different approaches has been demonstrated. A thermal decomposition of the iron precursor $\text{Fe}(\text{acac})_3$

nucleated preferentially nucleated Fe₃O₄ NPs on the SiO₂ surface of SiO₂-QDNRs. A low temperature approach to decorating the surface of APS functionalized SiO₂-QDNRs was also demonstrated by reacting the NPs with presynthesized BMPA functionalized Fe₃O₄ NPs.

5.4 References

1. Wang, J. S.; Shah, Z. H.; Zhang, S. F.; Lu, R. W., *Nanoscale* **2014**, 6, (9), 4418-4437.
2. Yi, D.; Selvan, S.; Lee, S.; Papaefthymiou, G.; Kundaliya, D.; Ying, J., *Journal of the American Chemical Society* **2005**, 127, (14), 4990-4991.
3. Lee, D.-E.; Koo, H.; Sun, I.-C.; Ryu, J. H.; Kim, K.; Kwon, I. C., *Chemical Society Reviews* **2012**, 41, (7), 2656-2672.
4. Selvan, S. T.; Patra, P. K.; Ang, C. Y.; Ying, J. Y., *Angewandte Chemie, International Edition* **2007**, 46, (14), 2448-2452.
5. Chen, O.; Riedemann, L.; Etoc, F.; Herrmann, H.; Coppey, M.; Barch, M.; Farrar, C. T.; Zhao, J.; Bruns, O. T.; Wei, H.; Guo, P.; Cui, J.; Jensen, R.; Chen, Y.; Harris, D. K.; Cordero, J. M.; Wang, Z.; Jasanoff, A.; Fukumura, D.; Reimer, R.; Dahan, M.; Jain, R. K.; Bawendi, M. G., *Nature Communications* **2014**, 5, 5093.
6. Carbone, L.; Nobile, C.; De Giorgi, M.; Sala, F. D.; Morello, G.; Pompa, P.; Hytch, M.; Snoeck, E.; Fiore, A.; Franchini, I. R.; Nadasan, M.; Silvestre, A. F.; Chiodo, L.; Kudera, S.; Cingolani, R.; Krahne, R.; Manna, L., *Nano Letters* **2007**, 7, (10), 2942-2950.
7. Hill, L.; Bull, M.; Sung, Y.; Simmonds, A.; Dirlam, P.; Richey, N.; DeRosa, S.; Shim, I.; Guin, D.; Costanzo, P.; Pinna, N.; Willinger, M.; Vogel, W.; Char, K.; Pyun, J., *ACS Nano* **2012**, 6, (10), 8632-8645.
8. Xu, Z.; Shen, C.; Hou, Y.; Gao, H.; Sun, S., *Chemistry of Materials* **2009**, 21, (9), 1778-1780.

9. Lee, J. E.; Lee, N.; Kim, H.; Kim, J.; Choi, S. H.; Kim, J. H.; Kim, T.; Song, I. C.; Park, S. P.; Moon, W. K.; Hyeon, T., *Journal of the American Chemical Society* **2010**, 132, (2), 552-557.
10. Lee, D. C.; Mikulec, F. V.; Pelaez, J. M.; Koo, B.; Korgel, B. A., *Journal of Physical Chemistry B* **2006**, 110, (23), 11160-11166.
11. Chang, C.-S.; Rothberg, L. J., *Chemistry of Materials* **2015**, 27, (9), 3211-3215.

CHAPTER 6: Synthesis of Electrospun Polymer Fiber Nanocomposites and Polarization Anisotropy Dependence of Energy Transfer between Gold Nanorods and CdSe/CdS Quantum Dot Nanorods

6.1 Introduction

Recently electrospun polymer fibers have been prepared containing embedded inorganic nanoparticles.¹⁻³ In some instances, the NPs embedded in electrospun fibers can be manipulated by external fields.^{2, 4-6} NPs with anisotropic shapes have been electrospun in polymer fibers, where the optical properties of the NPs that arise from the anisotropy of the NP shape has been useful for imparting novel physical properties to the fibers. For example, CdSe/CdS semiconductor tetrapods have been investigated as optical stress probes when embedded into polylactic acid (PLLA) nanofibers.⁷

It has recently been shown that Au nanorods (GNRs) can be aligned in polymer nanofibers, where the longitudinal axes of the GNRs align with the long axes of nanofibers.^{8, 9} Au NPs exhibit a localized surface plasmon resonance (SPR), where light is absorbed and scattered at certain wavelengths, which depend on the size and shape of the NP.¹⁰ A comprehensive review of the Au NP SPR has been published.¹¹ Much of the light absorbed by GNRs is converted into heat through non-radiative processes, which makes GNRs efficient photothermal heaters. In GNRs, the SPR is split into two modes corresponding to the longitudinal and transverse axes of the nanorods. Recently, aligned GNRs in aligned nanofiber mats have been shown to cause selective melting of the nanofibers when they are illuminated with polarized light whose electric field vector is parallel to the long axis of the GNRs and on resonance with their longitudinal SPR.^{12, 13}

CdSe/Cds quantum dot nanorods (QDNRs) have been shown to exhibit polarization anisotropy in their absorbance and emission spectra.¹⁴ Early in 2015, I began to study the alignment of CdSe/CdS QDNRs in polymer fibers through electrospinning. The objective of the study was to demonstrate the alignment of QDNRs within the fibers in a similar fashion to how GNRs align in individual nanofibers and to confirm our hypothesis that the nanofibers can selectively absorb and emit polarized light as a result of the polarization anisotropy of the QDNRs. However, during the investigation, a report was published that confirmed our hypothesis.¹⁵ Consequently, the objective was shifted to study the fabrication and optical properties of polymer nanofiber composites containing multiple types of inorganic NPs.

The interactions between fluorescent dyes and Au NPs are complex, where fluorescence enhancement or quenching can occur when in close proximity with each other. It is well known that Förster resonance energy transfer (FRET) and nanometal surface energy transfer (NSET) between donor dye molecules and acceptor Au NPs can occur when they are close in proximity.¹⁶⁻²³ Quantum dots (QDs) can serve as the donor and Au NPs as the acceptor, such that quenching of the QDs by Au NPs is a FRET-dominated process, whose efficiency depends on the distance between the two types of NPs.^{20, 24-27}

In this project, poly(ethylene oxide) (PEO) fibers were electrospun containing aligned arrays of CdSe/CdS quantum dot nanorods, PEG-functionalized SiO₂ overcoated QDNRs (PEG-SiO₂-QDNRs), and CTAB-stabilized GNRs. By combining PEG-SiO₂-QDNRs with GNRs in single fibers, we have demonstrated polarization-dependent energy transfer, which we believe is FRET. Controlling energy between PEG-SiO₂-QDNRs and GNRs is a potentially powerful tool for controlling the photoluminescence in signaling or sensing

applications. While FRET between QDs and Au NPs has already been extensively studied,^{22, 25, 28, 29} to the best of our knowledge FRET between NPs with anisotropic morphologies and optical anisotropies has not been reported.

6.2 Experimental Details

6.2.1 Chemicals

Reagents for Synthesizing CdSe/CdS QDNRs. A comprehensive list of chemicals used for synthesizing QDNRs is listed in Chapter 4.

Reagents for synthesizing SiO₂-QDNRs. A comprehensive list of chemicals used for synthesizing SiO₂-QDNRs is listed in Chapter 4.

Reagents for synthesizing polymer nanofibers

Polyethylene oxide (PEO, 900,000 g/mol, Scientific Polymer Products).

6.2.2 Nanoparticle synthesis

Synthesis of CdSe/CdS QDNRs. CdSe/CdS QDNRs were synthesized using previously reported methods.^{30, 31} Specific details of the procedures for synthesizing QDNRs were also discussed in Chapter 4.

Synthesis of SiO₂-QDNRs and PEG-SiO₂-QDNRs. SiO₂-QDNRs and PEG-SiO₂-QDNRs were synthesized using the methods discussed in Chapter 4.

Synthesis of GNRs. A colleague, Brian Chapman, synthesized GNRs by making minor modifications to a procedure that our group reported previously.³² The primary modification was to the syntheses was through decreasing the ascorbic acid (30 mL volume) injection rate

from 175 $\mu\text{L}/\text{min}$ to 22.9 $\mu\text{L}/\text{min}$ (the injection rate was divided by 8), resulting in a total injection time of 1,310 min. This gives a uniform deposition of Au onto the surface of the GNRs and decreases the aspect ratio and longitudinal SPR wavelength. The aspect ratio was tuned by varying the silver concentration. For GNRs with a longitudinal SPRs of 610 nm and 650 nm, respective amounts of 55% and 60% of the amount of AgNO_3 were used, compared to the amount needed for obtaining GNRs resonant at 800 nm.

Phase transfer of CdSe/CdS QDNRs. CdSe/CdS QDNRs were transferred into water through surface modification with CTAB. A CTAB solution was prepared by adding 1.407 g CTAB to 40 mL of DI water in a 100 mL three-neck, round-bottomed flask under ambient atmosphere. The solution was vigorously stirred (1-inch stir bar) and heated to 30 $^\circ\text{C}$ to dissolve the CTAB. Due to the mixture becoming viscous when chloroform is added, a large stir bar is needed to properly mix the solution. A 2 mL of dispersion of CdSe/CdS QDNRs in chloroform (12 mg/mL) was added over a period of 1 minute to the 40-mL aqueous CTAB solution. The mixture became viscous upon the QDNR-chloroform solution due to immiscibility of chloroform with the CTAB-water solution. The mixture was heated to 70 $^\circ\text{C}$ to evaporate the chloroform, resulting in CTAB-functionalized QDNRs in water. The QDNRs were purified and concentrated using a 15 mL centrifuge filter (Millipore, NMWL of 100kDa,).

Fabrication of fiber nanocomposites. Three PEO fiber nanocomposite samples were prepared, containing either QDNRs, GNRs, or a mixture of both. For preparing the PEO fibers, a solution of 6 wt% PEO in water was prepared. NPs were added at ratio of 3 wt%

GNRs or QDNRs with respect to the PEO powder. For the sample containing both QDNRs and GNRs, they were each added at ratios of 3 wt% with respect to the PEO powder. The solutions were vigorously stirred for a total of 4-8 hours to completely dissolve the PEO prior to electrospinning.

Each sample was electrospun following a common set of procedures. The QDNR/GNR:PEO solutions were loaded into a syringe equipped with a 20-gauge, blunt-tipped, stainless steel needle with a length of 3.81 cm. A programmable syringe pump (New Era Pump Systems, Model NE-1000) was used for continuous infusion of the NR:PEO solution from the syringe at a rate of 5 $\mu\text{L}/\text{min}$, which applying a voltage of 15 kV between the tip of the needle and a grounded metal collector plate. The collector was held at a distance of 15 cm from the tip of the needle. To acquire randomly oriented nanofibers, the collector plate was covered in Al foil. Aligned nanofibers were obtained by two methods: using a grounded cylindrical mandrel with a diameter of 8 cm rotated at approximately 3,500 rpm and using a grounded parallel plate (held at a distance of 15 cm from the tip of the needle) with a separation distance between the plates of 1.5 cm. A glass slide was placed between the parallel plates, where the slide was flush with the inside edges of the parallel plates. Fiber mats were deposited directly onto the glass slides.

6.2.3 Structural characterization

A JEOL 2000FX transmission electron microscope (TEM) operated at an accelerating voltage of 200 kV was used for imaging nanorod alignment and distribution within the fibers.

An FEI Verios 460L scanning electron microscope (SEM) was used to characterize the structure of the fiber nanocomposites.

6.2.4 Optical characterization

Optical absorbance spectra of the GNRs and QDNRs in solution prior to electrospinning were acquired using an Ocean Optics USB4000-VIS-NIR spectrophotometer. Emission spectra of the QDNRs in solution were acquired using an Ocean Optics USB4000-FL spectrophotometer with a 455 nm LED as the excitation source. All spectra were acquired in a 1-cm path length quartz cuvette.

Fluorescence decay measurements were acquired in collaboration with Gaurav Singh and Marcus Jones at the University of North Carolina, Charlotte with a mode-locked femtosecond Ti:sapphire laser (Spectra Physics MaiTai), operating at 80 MHz repetition rate and 820 nm, as a synchronous pump source for an optical parametric oscillator (OPO) (Spectra Physics Inspire). The frequency-doubled output (410 nm) from the OPO was then directed through two electro-optic modulators (Conoptics 350-105 KD*P Series) driven by a high voltage amplifier (Conoptics 25D), and a synchronous counter (Conoptics model 305). The modulators were operated at 100 kHz for this experiment.

The pulse-picked, frequency-doubled light, which was vertically polarized, was then focused on the sample using a 500 mm uncoated plano-convex lens from Newport. Fluorescence was collected from the sample at room temperature using the same lens, separated from the scattered laser light by a dichroic beam splitter (Semrock FF01-480) and a subtractive double monochromator (Spectral Products CM112). The sample fluorescence was

then detected by a hybrid PMT (Becker & Hickl HPM-100-40). A film polarizer (Thor Labs) was placed before the PMT to perform fluorescence anisotropy measurements. Fluorescence dynamics were measured by time-correlated single photon counting using a Becker & Hickl SPC-130 counting module.

6.3 Results and Discussion

6.3.1 Alignment of QDNRs, GNRs, and PEG-SiO₂-QDNRs in PEO fibers

CTAB-functionalized QDNRs, PEG-SiO₂-QDNRs, and CTAB-stabilized GNRs have been embedded and aligned within PEO nanofibers by an electrospinning technique. An aqueous dispersion of NRs dispersed in a PEO solution was loaded into a syringe outfitted with a stainless steel needle. Upon application of a voltage to the needle tip, a polymer fiber formed and deposited onto a substrate. Typical fiber diameters ranged from 100 nm to 400 nm, and the embedded NPs were distributed evenly throughout the fibers (**Figure 1**). Fibers with random and aligned orientations were fabricated (**Figure 1a and 1b**). The nanofibers have smooth walls, and porosity was not evident from electron microscopy. Alignment of the CTAB-functionalized QDNRs, PEG-SiO₂-QDNR, and CTAB-stabilized GNRs was observed by TEM and SEM/STEM, where the long axes of the nanorods were oriented parallel to the length of the fibers (**Figure 1c and 1d**). Nanorod alignment likely results from a combination of shear forces produced during electrospinning and preferential alignment parallel to the electric field.

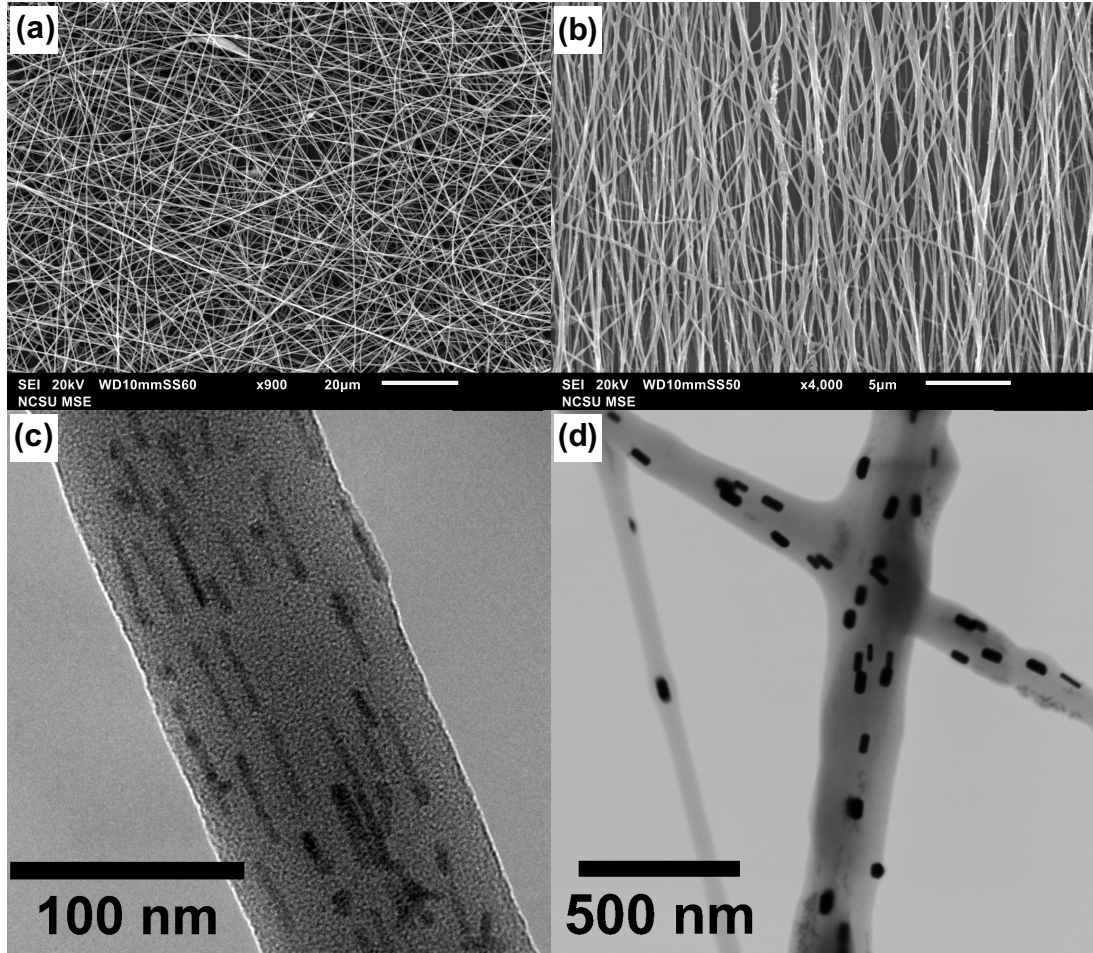


Figure 1. SEM and TEM images of electrosun PEO fibers containing embedded nanorods. SEM images of (a) randomly oriented and (b) aligned fibers. TEM images of aligned (c) CTAB-functionalized QDNRs and (d) CTAB-stabilized GNRs in PEO fibers.

Aligned PEG-SiO₂-QDNRs were embedded into PEO fibers (**Figure 2**). PEG-SiO₂-QDNRs were chosen in this study because the SiO₂ shell helps to preserve the optical integrity of the QDNRs in the fibers and can serve as a physical spacer for small interparticle separation distances. PEG functionalized surfaces of the SiO₂-QDNRs was necessary to promote compatibility with PEO and prevent crosslinking of the NRs in the fibers. PEG-

SiO₂-QDNRs with large and small ARs were used. The lengths of QDNRs with large and small ARs were 95 nm and 43 nm, respectively. Both the large and small AR PEG-SiO₂-QDNRs both show good alignment within the polymer fibers and exhibit very good dispersity within in the fiber (**Figure 2b and 2c**).

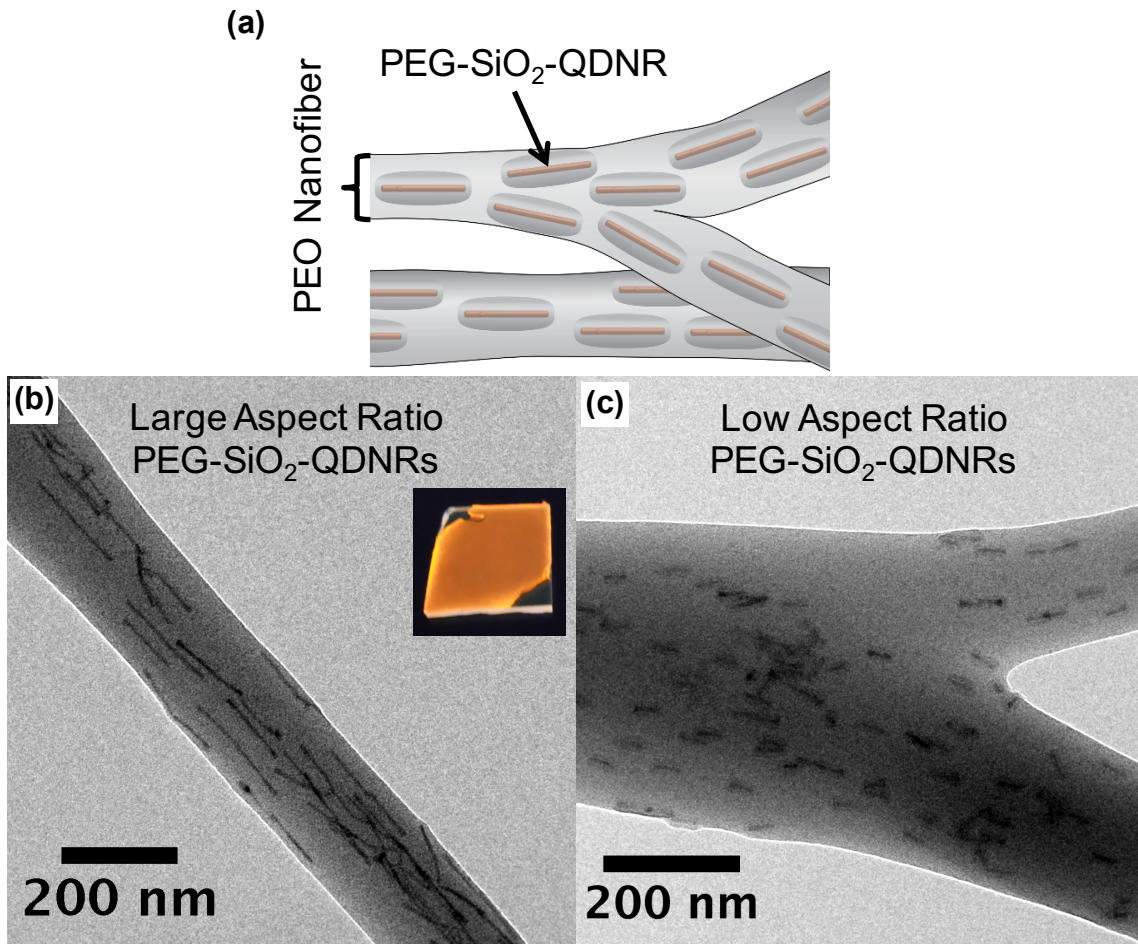


Figure 2. An illustration and TEM images of PEG-SiO₂-QDNRs in PEO fibers. (a) is an illustration showing the generalized structure of the fiber. TEM images of PEG-SiO₂-QDNRs with (a) large AR and (b) small AR embedded in PEO fibers.

Nanofiber composites containing both GNRs and PEG-SiO₂-QDNRs were fabricated for the study (**Figure 3**). Both types of particles exhibit good alignment and good interparticle separation with the fibers. However, PEG-SiO₂-QDNRs exhibit some clustering, which could result of strong electric field effects from the GNRs that arise during the electrospinning process. Due to the thick PEG-SiO₂ shell approximately 12 nm thick from the CdS shell, spacing is controlled and QDNR-QDNR contact is mitigated (**Figure 3b**).

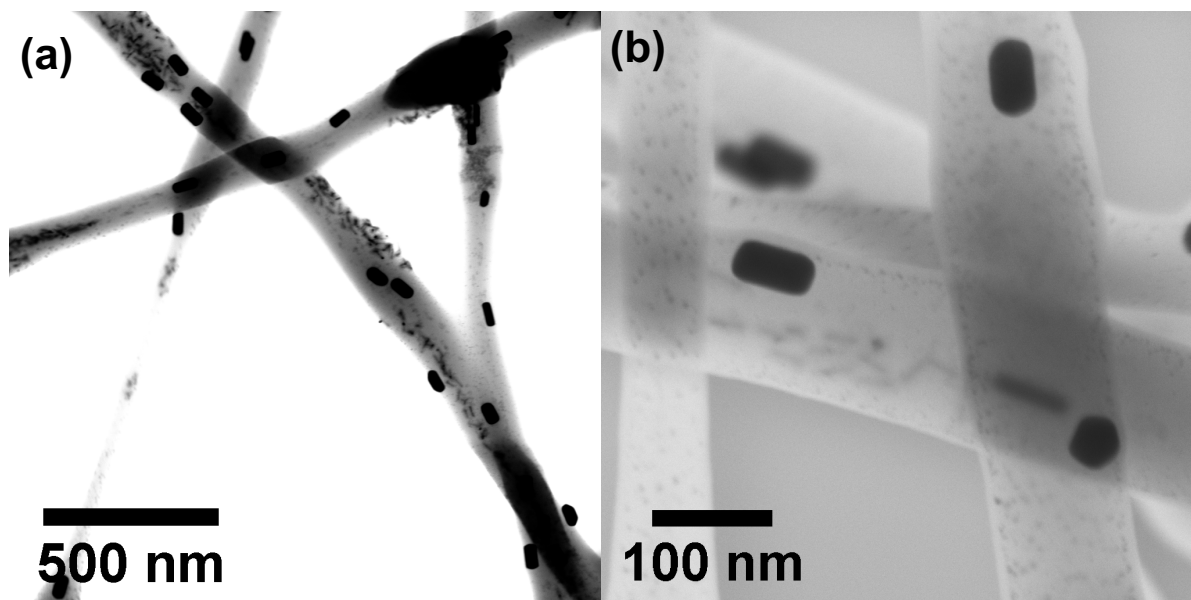


Figure 3. STEM images of aligned GNRs and PEG-SiO₂-QDNRs embedded in PEO nanofibers. (a) bright field lower magnification image and (b) dark field image show the structure of the fibers.

Optical spectra of CTAB functionalized QDNRs in PEO fibers were acquired (**Figure 4**). The nanofibers exhibited strong polarization dependence on the absorption of polarized light at 455 nm (**Figure 4a**). Emission of the nanofibers was also strongly polarized (**Figure 4b and 4c**). Optical spectra for the QDNRs and GNR used for fabricating the composite

nanofibers is shown in **Figure 5**. The absorbance and emission spectra for the QDNRs was collected and the emission peak is at 616 nm (**Figure 5a**). The spectral overlap of the emission of the QDNRs with the maximum absorbance peak of the GNRs shows that the difference between the peak intensities is approximately 6 nm where the emission of the QDNRs lies on the blue side of the GNR longitudinal SPR (**Figure 5b**). The spectral overlap between the NPs should allow for energy transfer if the interparticle distance within the fibers is small enough.

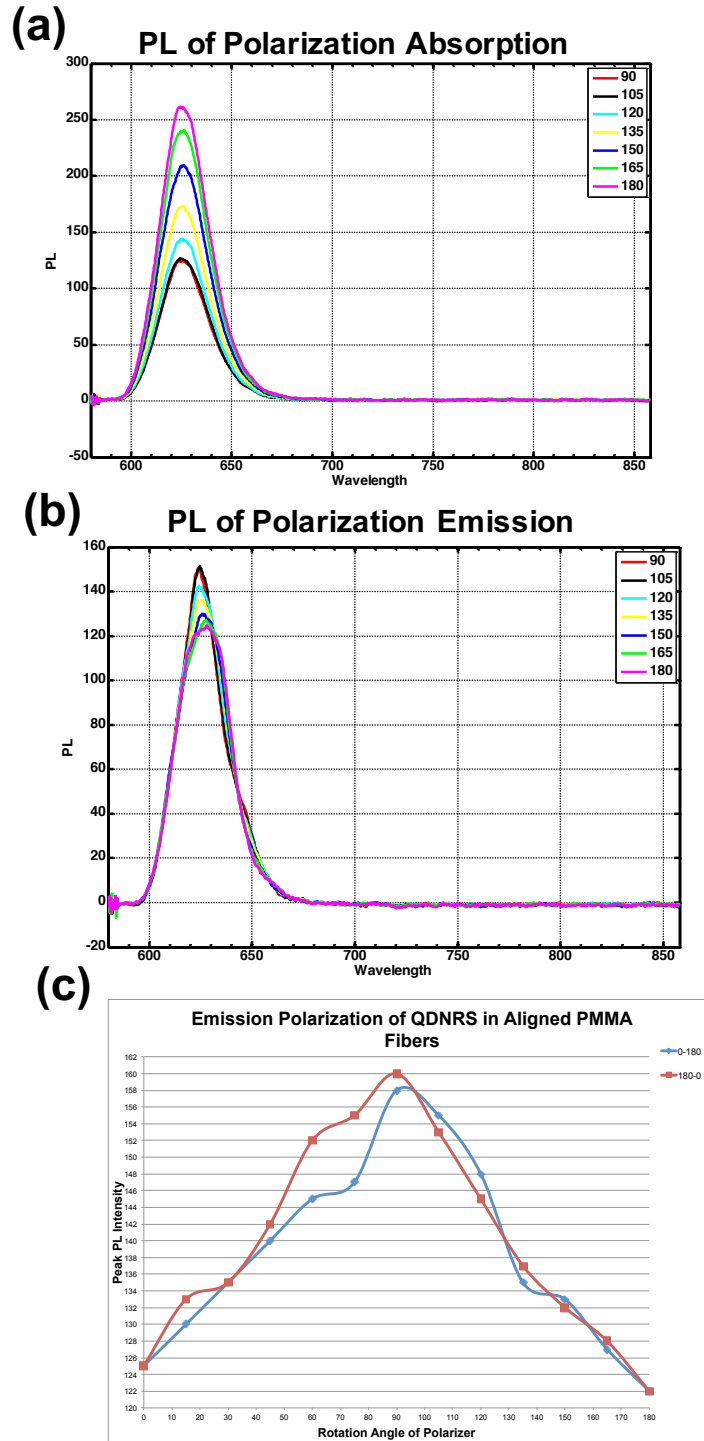


Figure 4. Polarized absorbance and emission spectra of QDNRS in PEO nanofibers.

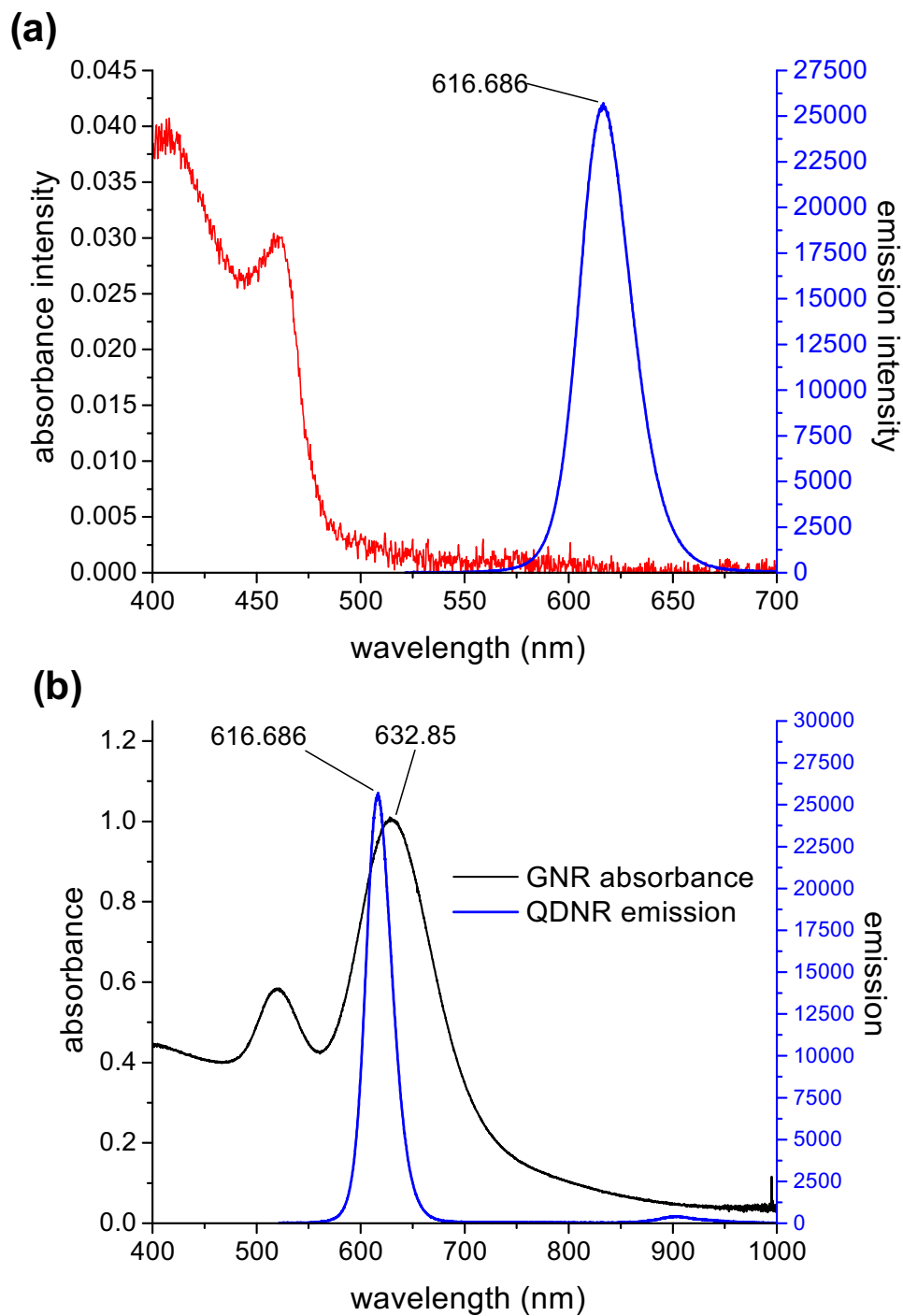


Figure 5. Optical spectra of QDNRs and GNRs. (a) Optical absorbance and emission spectra of QDNRs and (b) emission spectra of QDNRs and absorbance spectra of GNRs that were used to fabricate the composite NFs.

Optical measurements were conducted on three types of nanofiber composites that consisted of QDNR nanofibers in randomly oriented nanofibers, QDNR nanofibers in aligned nanofibers, and QDNRs-GNRs in randomly oriented nanofibers (**Figure 6**). Fluorescence lifetime measurements using vertically polarized light was also acquired on QDNR and QDNR-GNR nanofiber composites of randomly oriented fibers (**Figure 7**). The average lifetimes for QDNR nanofibers in randomly oriented nanofibers, QDNR nanofibers in aligned nanofibers, and QDNRs-GNRs in randomly oriented nanofibers were approximately 35 ns, 36 ns, and 26 ns, respectively. There is a noticeable decrease in the average lifetimes in the QDNR-GNR nanofibers versus the QDNR nanofiber composites. The decrease in the average lifetime in the QDNR-GNR nanofibers is strong evidence that energy transfer is occurring. Using equation 1.1, optical anisotropies were calculated for the nanofiber composites (**Figure 6**). Optical anisotropies for QDNR nanofibers in randomly oriented nanofibers, QDNR nanofibers in aligned nanofibers, and QDNRs-GNRs in randomly oriented nanofibers were approximately 0.133, -0.068, and 0.079, respectively.

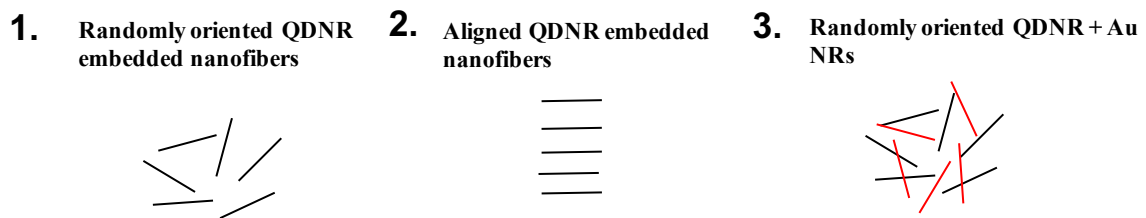


Figure 6 Schematic of the types of nanofiber composites that were used to optically characterize.

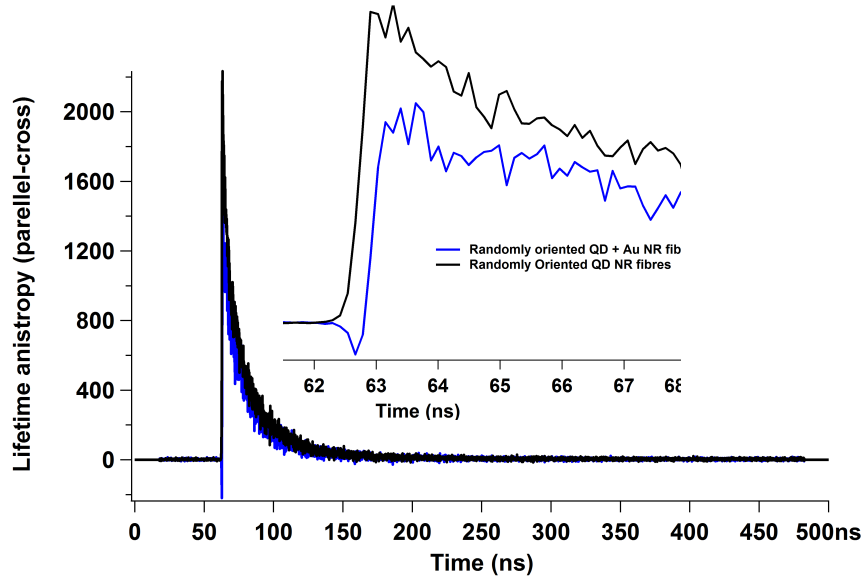


Figure 7. Fluorescence lifetime spectra of QDNR-GNR nanofiber composites with random orientation.

$$Anisotropy, r = \frac{I_{\parallel} - g I_{\perp}}{I_{\parallel} + 2g I_{\perp}}$$

$$g = \frac{S_v}{S_H}$$

g is the correction factor
accounting for polarization
sensitivity of the detection system

Equation 1.1

6.3.2 Conclusions and ongoing work

Polymer fiber nanocomposites with embedded QDNRs, PEG-SiO₂-QDNRs, and a mixture of GNRs and QDNRs were achieved by electrospinning. Longitudinal axes of the nanorods aligned with the long axis of the nanofibers. Optical measurements of the

nanofibers show polarization anisotropy that arise due to the anisotropic characteristics of the nanorods. Energy transfer between aligned GNRs and QDNRs embedded within the same fibers showed polarization dependent energy transfer. Optimization of the composite nanofiber optical properties is ongoing work, including the enhancement of energy transfer between QDNRs and GNRs. Additionally, we expect that energy transfer can eventually be controlled between GNRs and QDNRs by controlling spatial orientation of the nanorod and nanofiber assemblies.

6.4 References

1. Demir, M. M.; Gulgun, M. A.; Menciloglu, Y. Z.; Erman, B.; Abramchuk, S. S.; Makhaeva, E. E.; Khokhlov, A. R.; Matveeva, V. G.; Sulman, M. G., *Macromolecules* **2004**, 37, (5), 1787-1792.
2. Liu, H.; Edel, J. B.; Bellan, L. M.; Craighead, H., *Small* **2006**, 2, (4), 495-499.
3. Zhang, D.; Karki, A. B.; Rutman, D.; Young, D. P.; Wang, A.; Cocke, D.; Ho, T. H.; Guo, Z., *Polymer* **2009**, 50, (17), 4189-4198.
4. Maity, S.; Downen, L. N.; Bochinski, J. R.; Clarke, L. I., *Polymer* **2011**, 52, (7), 1674-1685.
5. Mthethwa, T. P.; Moloto, M. J.; De Vries, A.; Matabola, K. P., *Materials Research Bulletin* **2011**, 46, (4), 569-575.
6. Roskov, K. E.; Atkinson, J. E.; Bronstein, L. M.; Spontak, R. J., *RSC Advances* **2012**, 2, (11), 4603-4607.

7. Raja, S. N.; Olson, A. C. K.; Thorkelsson, K.; Luong, A. J.; Hsueh, L.; Chang, G.; Gludovatz, B.; Lin, L.; Xu, T.; Ritchie, R. O.; Alivisatos, A. P., *Nano Letters* **2013**, 13, (8), 3915-3922.
8. Kim, G.-M.; Wutzler, A.; Radusch, H.-J.; Michler, G. H.; Simon, P.; Sperling, R. A.; Parak, W. J., *Chemistry of Materials* **2005**, 17, (20), 4949-4957.
9. Roskov, K. E.; Kozek, K. A.; Wu, W.-C.; Chhetri, R. K.; Oldenburg, A. L.; Spontak, R. J.; Tracy, J. B., *Langmuir* **2011**, 27, (23), 13965-13969.
10. Eustis, S.; El-Sayed, M. A., *Chemical Society Reviews* **2006**, 35, (3), 209-217.
11. Huang, X.; El-Sayed, M. A., *Journal of Advanced Research* **2010**, 1, (1), 13-28.
12. Maity, S.; Kozek, K. A.; Wu, W.-C.; Tracy, J. B.; Bochinski, J. R.; Clarke, L. I., *Particle & Particle Systems Characterization* **2013**, 30, (2), 193-202.
13. Maity, S.; Wu, W.-C.; Xu, C.; Tracy, J. B.; Gundogdu, K.; Bochinski, J. R.; Clarke, L. I., *Nanoscale* **2014**, 6, (24), 15236-15247.
14. Hadar, I.; Hitin, G. B.; Sitt, A.; Faust, A.; Banin, U., *Journal of Physical Chemistry Letters* **2013**, 4, (3), 502-507.
15. Hasegawa, M.; Hirayama, Y.; Dertinger, S., *Applied Physics Letters* **2015**, 106, (5), 051103.
16. Armstrong, R. E.; Riskowski, R. A.; Strouse, G. F., *Photochemistry and Photobiology* **2015**, 91, (3), 732-738.
17. Breshike, C. J.; Riskowski, R. A.; Strouse, G. F., *The Journal of Physical Chemistry C* **2013**, 117, (45), 23942-23949.
18. Jennings, T. L.; Schlatterer, J. C.; Singh, M. P.; Greenbaum, N. L.; Strouse, G. F., *Nano Letters* **2006**, 6, (7), 1318-1324.

19. Jennings, T. L.; Singh, M. P.; Strouse, G. F., *Journal of the American Chemical Society* **2006**, 128, (16), 5462-5467.
20. Mun'delanji, C. V.; Kerman, K.; Hsing, I.-M.; Tamiya, E., *Nanobiosensors and Nanobioanalyses*. Springer: 2015.
21. Singh, M. P.; Jennings, T. L.; Strouse, G. F., *The Journal of Physical Chemistry B* **2009**, 113, (2), 552-558.
22. Tang, B.; Cao, L.; Xu, K.; Zhuo, L.; Ge, J.; Li, Q.; Yu, L., *Chemistry-A European Journal* **2008**, 14, (12), 3637-3644.
23. Yun, C. S.; Javier, A.; Jennings, T.; Fisher, M.; Hira, S.; Peterson, S.; Hopkins, B.; Reich, N. O.; Strouse, G. F., *Journal of the American Chemical Society* **2005**, 127, (9), 3115-3119.
24. Han, H.; Valle, V.; Maye, M. M., *Nanotechnology* **2012**, 23, (43), 435401.
25. Kim, Y.-P.; Oh, Y.-H.; Oh, E.; Ko, S.; Han, M.-K.; Kim, H.-S., *Analytical Chemistry* **2008**, 80, (12), 4634-4641.
26. Li, M.; Cushing, S. K.; Wang, Q.; Shi, X.; Hornak, L. A.; Hong, Z.; Wu, N., *The Journal of Physical Chemistry Letters* **2011**, 2, (17), 2125-2129.
27. Uddayasankar, U.; Krull, U. J., *Langmuir* **2015**, 31, (29), 8194-8204.
28. Liu, J.; Lee, J. H.; Lu, Y., *Analytical Chemistry* **2007**, 79, (11), 4120-4125.
29. Oh, E.; Hong, M.-Y.; Lee, D.; Nam, S.-H.; Yoon, H. C.; Kim, H.-S., *Journal of the American Chemical Society* **2005**, 127, (10), 3270-3271.
30. Carbone, L.; Nobile, C.; De Giorgi, M.; Sala, F. D.; Morello, G.; Pompa, P.; Hytch, M.; Snoeck, E.; Fiore, A.; Franchini, I. R.; Nadasan, M.; Silvestre, A. F.; Chiodo, L.; Kudera, S.; Cingolani, R.; Krahne, R.; Manna, L., *Nano Letters* **2007**, 7, (10), 2942-2950.

31. Hill, L.; Bull, M.; Sung, Y.; Simmonds, A.; Dirlam, P.; Richey, N.; DeRosa, S.; Shim, I.; Guin, D.; Costanzo, P.; Pinna, N.; Willinger, M.; Vogel, W.; Char, K.; Pyun, J., *ACS Nano* **2012**, 6, (10), 8632-8645.
32. Kozek, K. A.; Kozek, K. M.; Wu, W.-C.; Mishra, S. R.; Tracy, J. B., *Chemistry of Materials* **2013**, 25, (22), 4537-4544.

CHAPTER 7: Silica and Cobalt-Silica Aerogel Composites

7.1 Introduction

One of my first projects when I arrived at NC State University in January 2011 was in the fabrication of the three dimensional assembly of colloidal metal nanoparticles in silica aerogel composites. While the focus of research was later developed into other areas that led away from the aerogel project, the experience and knowledge gained in this project was critical in setting the stage for the development of other projects. This chapter will briefly discuss my work and findings on the fabrication of cobalt NP-silica composite aerogels.

Aerogels are a type of material that relies on the careful assembly of colloidal particles through sol-gel chemistry. Aerogels are solids that have extremely low densities and high porosities with very large internal surface areas. They are synthesized by the condensation of a colloidal gel followed by the careful removal of the liquid that fills the pores of the gel.¹⁻³ There have been significant efforts over the past several years to make high quality aerogels of many types of compositions. Aerogels are a promising material for applications such as thermal barriers, environmental remediation, batteries, gas sensing, supercapacitors, and electrocatalysts.⁴⁻¹³

Our group is well acquainted with the synthesis and magnetic properties of colloidal Cobalt and cobalt oxide NPs.^{14, 15} Co NPs are an excellent material for a wide array of applications, including battery, catalytic, magnetic fluids and solids, and fuel cell applications.¹⁶⁻²¹ Moreover, Co NPs have been used for the synthesis magnetic composite

nanomaterials and have been used to study magnetic self-assembly into higher order structures.^{22,23}

In this work, we have synthesized a composite Co NP - SiO₂ aerogel. We incorporated presynthesized ligand stabilized Co NPs with TMOS, a silica precursor. Then, we formed a gel through the hydrolysis and base catalysis of TMOS where Co NPs were dispersed throughout the gel. The gel was supercritically dried to result three dimensional assembly of Co NPs suspended in a SiO₂ framework.

7.2 Experimental Details

7.2.1 Chemicals. 1,2 dichlorobenzene (DCB, anhydrous, EMD Chemicals), trioctylphosphine oxide (TOPO, 99%, Strem), oleic acid (OAC, 99%, Alfa Aesar), di-n-octylamine (DOA, 98%, Alfa Aesar), methanol (ChromAR, Macron), hexanes (ChromAR, Macron), tetramethoxysilane (TMOS, 99.9%, Alfa Aesar), saturated ammonium hydroxide (NH₄OH; 28-30 % as NH₃, ACS reagent grade, Macron), deionized (DI) water (ACS reagent grade, ASTM Type I, ASTM Type II, Ricca), 12-hydroxydocecanoic acid (97%, Sigma-Aldrich)

7.2.2 Material synthesis

Cobalt NP synthesis. To fabricate the aerogel, oleic acid and dioctylamine stabilized cobalt nanoparticles were initially synthesized via the method outlined by Bao *et al.*²⁴ For our procedure, we synthesized multiple-grained Co nanoparticles by dissolving 1.58 mmol (0.54 g) of cobalt carbonyl in 3 mL of 1,2-dichlorobenzene (DCB). The solution was then injected into a refluxing (182 °C) solution of 12 mL DCB, 0.62 mmol (0.2 mL) oleic acid, and 0.61

mmol (0.34 mL) of di-n-octylamine (DOA) 98%. The combined solutions refluxed for 15 minutes, then aged for 15 minutes at 140 °C. The particles were flocculated by adding methanol and then redispersed in hexanes.

Ligand exchange on cobalt NPs. For adequate solubility of cobalt NPs in polar solvents, ligand exchange was performed on the particles. The nanoparticles were isolated and dried via rotoevaporation. The nanoparticles were redispersed in methanol and a generous amount of 12-hydroxydocecanoic acid was added to the solution. Excess ligands were removed by flocculating the nanoparticles by adding hexanes, centrifuging, then redispersing the particles in methanol.

Aerogel Synthesis. A base catalyst method was utilized in synthesizing Co-SiO₂ composite aerogel. 2.55 g (2.5 mL) TMOS was mixed with 1.98g (2.5 mL) of methanol and 2.5 mL of highly concentrated cobalt nanoparticle solution. 1.215 g (1.35 mL) of ammonium hydroxide was mixed with 1000 mL of deionized water. 1.25 g (1.25 mL) of the ammonium hydroxide in water solution was mixed with the tetramethoxysilane and methanol solution. Gel formation occurred in approximately 15 minutes.

After the silica-cobalt nanoparticle wet gel formation, the gel was allowed to age and solvent exchange with acetone was conducted once per day for four days. The solvent was then removed by a supercritical drying procedure. The wet gel samples were placed into a sealed high-pressure vessel (**Figure 2**) where liquid carbon dioxide was exchanged with the methanol contained in the gel. Once the carbon dioxide exchange was completed, the vessel

was then heated to the supercritical conditions of the carbon dioxide (40 °C and 1200 psi). The system was given time to equilibrate then the pressure was slowly released until atmospheric pressure in the vessel was obtained. This resulted in the final product.

7.2.3 Structural characterization

Structural characterization of the, Co NPs, SiO₂ aerogels, and Co-SiO₂ composite aerogels were conducted. A JEOL 2000FX transmission electron microscope (TEM) operated at an accelerating voltage of 200 kV was used for imaging. Samples prepared for imaging Co NPs by dropcasing NPs dispersed methanol on a TEM grid. Samples were prepared for imaging aerogels by creating a powder of the aerogel and dropping the product onto a TEM grid. The TEM grids were Cu TEM grids with ultrathin carbon and Formvar supports.

7.3 Results and Discussion

A simplified procedure for synthesizing aerogels includes three major steps (**Figure 1**). The first step is preparation of a sol (colloidal particle in solution). In the SiO₂ aerogels for our studies, colloidal SiO₂ nanoparticles are synthesized through the hydrolysis and base catalysis of TMOS. For the Co-SiO₂ composite aerogels, the Co NPs were added to the solution prior to the base catalyst. The second step is the condensation of the sol to form a gel. As the SiO₂ NPs from the first step age, they begin to destabilize from solution to form a three-dimensional interconnected network of nanoparticles. Once the gel forms, a series of solvent exchanges is performed. The first solvent exchange from methanol to acetone is conducted. The gel is then transferred into the supercritical dryer (**Figure 2**) to exchange

acetone with liquid CO₂. The third step is the supercritical drying of CO₂ from the gel to give aerogel, a dry product that consists of a porous SiO₂ or Co-SiO₂ network. In the supercritical drying step, CO₂ in the liquid phase is heated and pressurized to 40 °C and 1000 psi where it enters the supercritical phase. Once in the supercritical phase, the capillary forces between CO₂ molecules is reduced, which minimizes collapse of the open pores in the gel during the drying process. When the supercritical CO₂ is drained, aerogel is obtained.

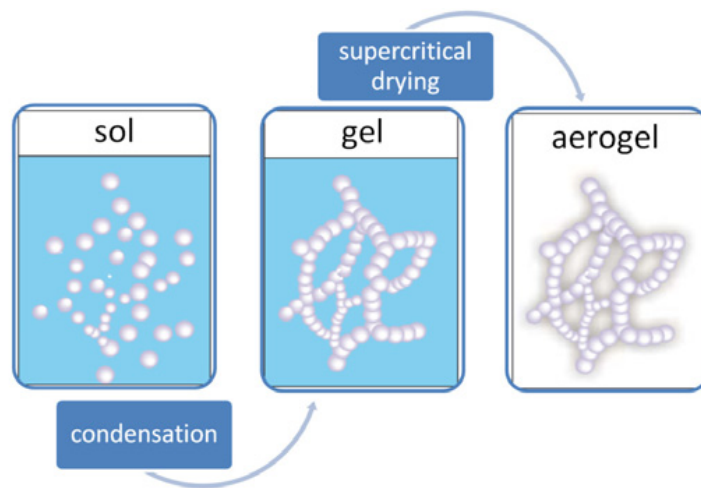


Figure 1. A simplified schematic for the synthesis of an aerogel.

A high-pressure supercritical dryer was built in our lab according to directions reported at the website, www.aerogel.org, in order to achieve elevated temperatures and pressures required acquire supercritical CO₂ (**Figure 2**). The reactor was fabricated from stainless steel 316 and consisted of a four arm cross for the sample holding location. Influent and effluent CO₂ ports were installed to introduce liquid CO₂ and drain supercritical CO₂,

respectively, into the sample chamber. We installed temperature and pressure gauges in the supercritical dryer to accurately monitor conditions in the sample chamber.

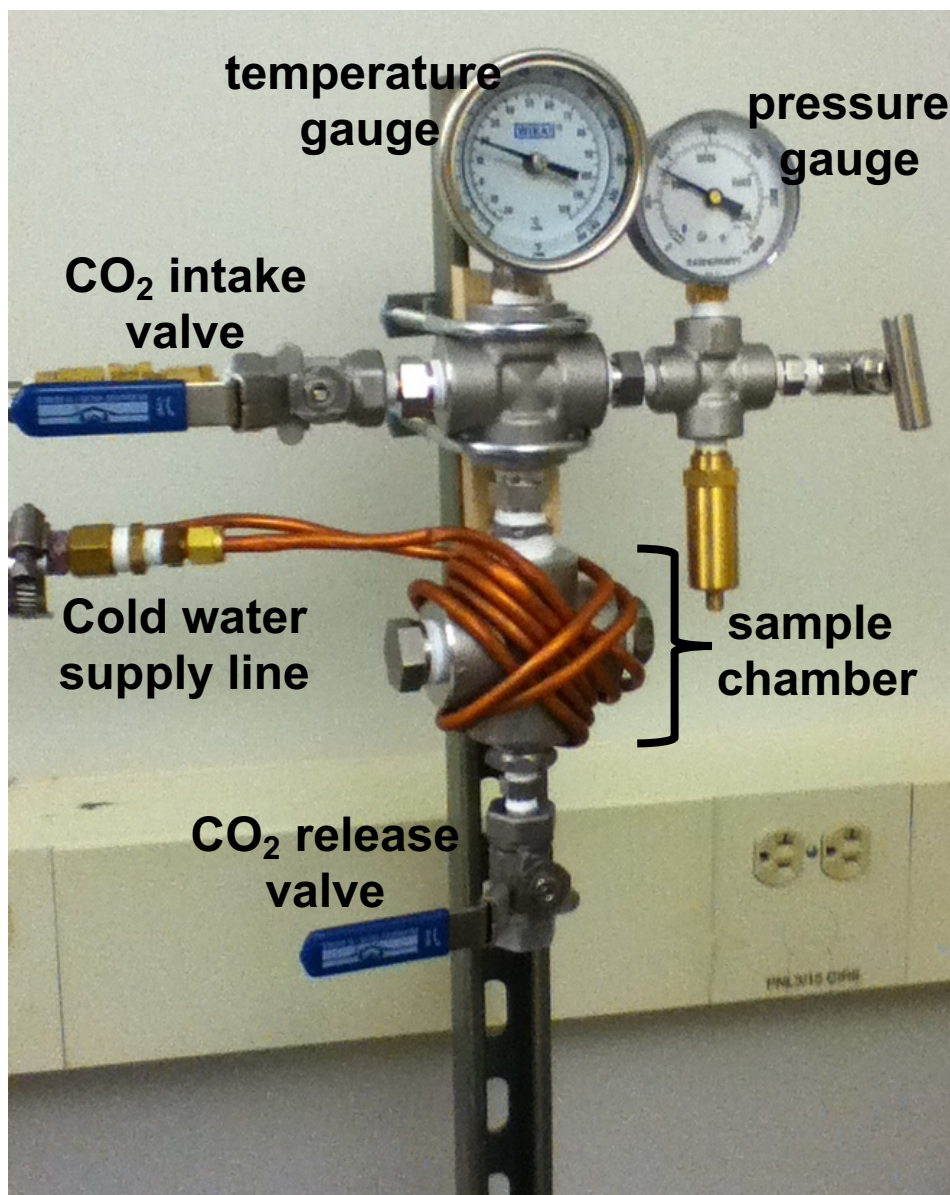


Figure 2. A photograph of the supercritical dryer built in our lab for the synthesis of SiO_2 and Co- SiO_2 composite aerogels.

Colloidal Co NPs stabilized with oleic acid and dioctylamine ligands were used for making a cobalt-silica aerogel composite (**Figure 3**). The average size of the particles were 6.3 nm in diameter with some polydispersity. Polydispersity in the size range of the Co NPs does not affect the product of the aerogel synthesis. The stock Co NPs were dispersible in non-polar solvents due to the oleic acid and dioctylamine ligands that functionalize the surface of the NPs. For fabricating the Co-SiO₂ aerogel composites the Co NPs needed to be dispersible in methanol. A ligand exchange procedure was conducted to replace oleic acid and dioctylamine ligands with hydroxydodecanoic acid. After the ligand exchange, the Co NPs were dispersible in methanol and other polar solvents.

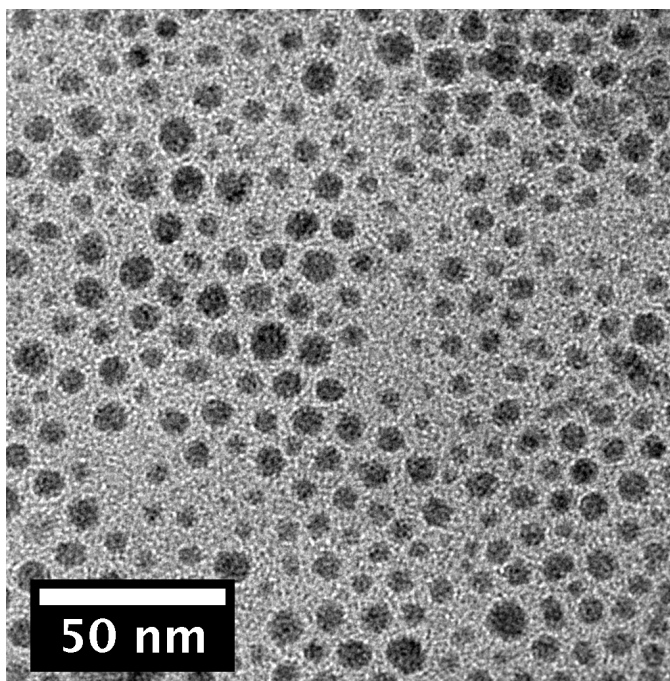


Figure 3. TEM images of colloidal Co NPs used for fabricating the Co-SiO₂ composite aerogels.

Both SiO₂ and Co-SiO₂ composite aerogels were synthesized (**Figure 4**). The porous nature of the aerogels is evident in the TEM images. The structure of the SiO₂ aerogel (**Figure 4a**) is not dissimilar to the structure found in the Co-SiO₂ composite aerogel (**Figure 4b**). Due to the small sizes of the Co NPs and low phase contrast in the TEM, the Co NPs were difficult to find in the composite product.

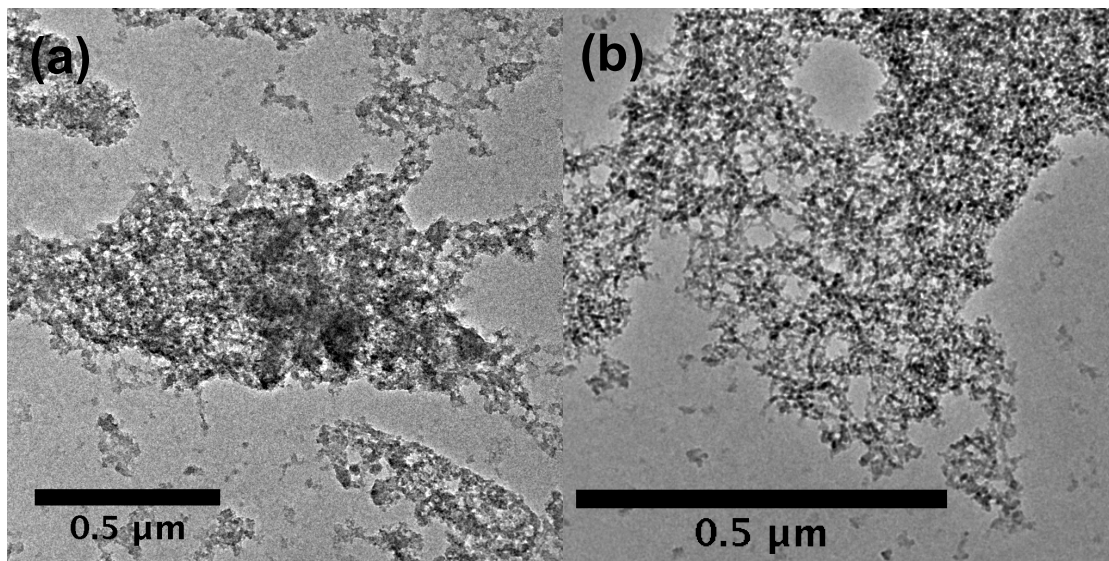


Figure 4. TEM images of (a) SiO₂ aerogel and (b) Co-SiO₂ aerogel composite.

7.4 Conclusions

SiO₂ and Co-SiO₂ composite aerogels were synthesized. A supercritical dryer was built in our lab to perform supercritical drying of CO₂ of gels. Co NPs were introduced during the hydrolysis and condensation of TMOS to be incorporated into the SiO₂ network.

7.5 References

1. Kistler, S. S., *Nature* **1931**, 127, 741.
2. Kistler, S., *The Journal of Physical Chemistry* **1932**, 36, (1), 52-64.
3. Gesser, H. D.; Goswami, P. C., *Chemical Reviews* **1989**, 89, (4), 765-788.
4. Wu, Z.-S.; Yang, S.; Sun, Y.; Parvez, K.; Feng, X.; Müllen, K., *Journal of the American Chemical Society* **2012**, 134, (22), 9082-9085.
5. Wu, Z. S.; Winter, A.; Chen, L.; Sun, Y.; Turchanin, A.; Feng, X.; Müllen, K., *Advanced Materials* **2012**, 24, (37), 5130-5135.
6. Wu, Z.-Y.; Li, C.; Liang, H.-W.; Zhang, Y.-N.; Wang, X.; Chen, J.-F.; Yu, S.-H., *Scientific Reports* **2014**, 4, 4079.
7. Wang, R.; Li, G.; Dong, Y.; Chi, Y.; Chen, G., *Analytical Chemistry* **2013**, 85, (17), 8065-8069.
8. Wang, R.; Xu, C.; Du, M.; Sun, J.; Gao, L.; Zhang, P.; Yao, H.; Lin, C., *Small* **2014**, 10, (11), 2260-2269.
9. Chen, K.; Neugebauer, A.; Goutierre, T.; Tang, A.; Glicksman, L.; Gibson, L. J., *Energy and Buildings* **2014**, 76, 336-346.
10. Liu, W.; Herrmann, A.-K.; Bigall, N. C.; Rodriguez, P.; Wen, D.; Oezaslan, M.; Schmidt, T. J.; Gaponik, N.; Eychmüller, A., *Accounts of Chemical Research* **2015**, 48, (2), 154-162.
11. Garnier, C.; Muneer, T.; McCauley, L., *Building and Environment* **2015**, 94, Part 1, 231-238.
12. Qi, H.; Liu, J.; Pionteck, J.; Pötschke, P.; Mäder, E., *Sensors and Actuators B: Chemical* **2015**, 213, 20-26.

13. Li, L.; He, S.; Liu, M.; Zhang, C.; Chen, W., *Analytical Chemistry* **2015**, 87, (3), 1638-1645.
14. Tracy, J. B.; Weiss, D. N.; Dinega, D. P.; Bawendi, M. G., *Physical Review B* **2005**, 72, (6), 064404.
15. Tracy, J. B.; Bawendi, M. G., *Physical Review B* **2006**, 74, (18), 184434.
16. Laurent, S.; Dutz, S.; Häfeli, U. O.; Mahmoudi, M., *Advances in Colloid and Interface Science* **2011**, 166, (1-2), 8-23.
17. Wen, W.; Wu, J.-M.; Tu, J.-P., *Journal of Alloys and Compounds* **2012**, 513, 592-596.
18. Zhu, Y.; Ye, Y.; Zhang, S.; Leong, M. E.; Tao, F., *Langmuir* **2012**, 28, (21), 8275-8280.
19. Deng, J.; Kang, L.; Bai, G.; Li, Y.; Li, P.; Liu, X.; Yang, Y.; Gao, F.; Liang, W., *Electrochimica Acta* **2014**, 132, 127-135.
20. Kilic, M. S.; Korkut, S.; Hazer, B.; Erhan, E., *Biosensors and Bioelectronics* **2014**, 61, 500-505.
21. Raj, P. M.; Sharma, H.; Reddy, G. P.; Altunyurt, N.; Swaminathan, M.; Tummala, R.; Nair, V., *Journal of electronic materials* **2014**, 43, (4), 1097-1106.
22. Hill, L.; Bull, M.; Sung, Y.; Simmonds, A.; Dirlam, P.; Richey, N.; DeRosa, S.; Shim, I.; Guin, D.; Costanzo, P.; Pinna, N.; Willinger, M.; Vogel, W.; Char, K.; Pyun, J., *ACS Nano* **2012**, 6, (10), 8632-8645.
23. Keng, P. Y.; Bull, M. M.; Shim, I.-B.; Nebesny, K. G.; Armstrong, N. R.; Sung, Y.; Char, K.; Pyun, J., *Chemistry of Materials* **2011**, 23, (5), 1120-1129.
24. Bao, Y.; An, W.; Turner, C. H.; Krishnan, K. M., *Langmuir* **2010**, 26, (1), 478-483.

CHAPTER 8: Contributions to Other Projects

8.1 Airbrushed Nickel Nanoparticles for Large-Area Growth of Vertically Aligned Carbon Nanofibers on Metal (Al, Cu, Ti) Surfaces¹

This project was one of the first projects that I worked on during my PhD. It was a group collaboration between Dr. Joseph Tracy's research group and Dr. Anatoli Melechko's research group at North Carolina State University. The Melechko research group had capabilities of growing silicon nitride coated vertically aligned carbon nanofibers (VACNFs) by plasma enhanced chemical vapor deposition (PECVD). The growth of VACNFs required the use of Ni NP catalysts.

The motivation for this project was to demonstrate that large-area arrays of VACNFs could be grown on various metal substrates by using an air brush technique to deposit Ni NP catalysts and silicon powder. At the time, there was not a facile way to grow large-area arrays of VACNFs. We developed a method for large-area deposition of Ni NPs on Al, Cu, and Ti substrates for the subsequent growth of VACNFs (**Figure 1**). My role in the project was to help set up air brushing unit to spray Ni NPs and silicon powder in a controlled and safe manner, help synthesize Ni NPs, and conduct the air brushing of the Ni NPs and silicon powder on various substrates.

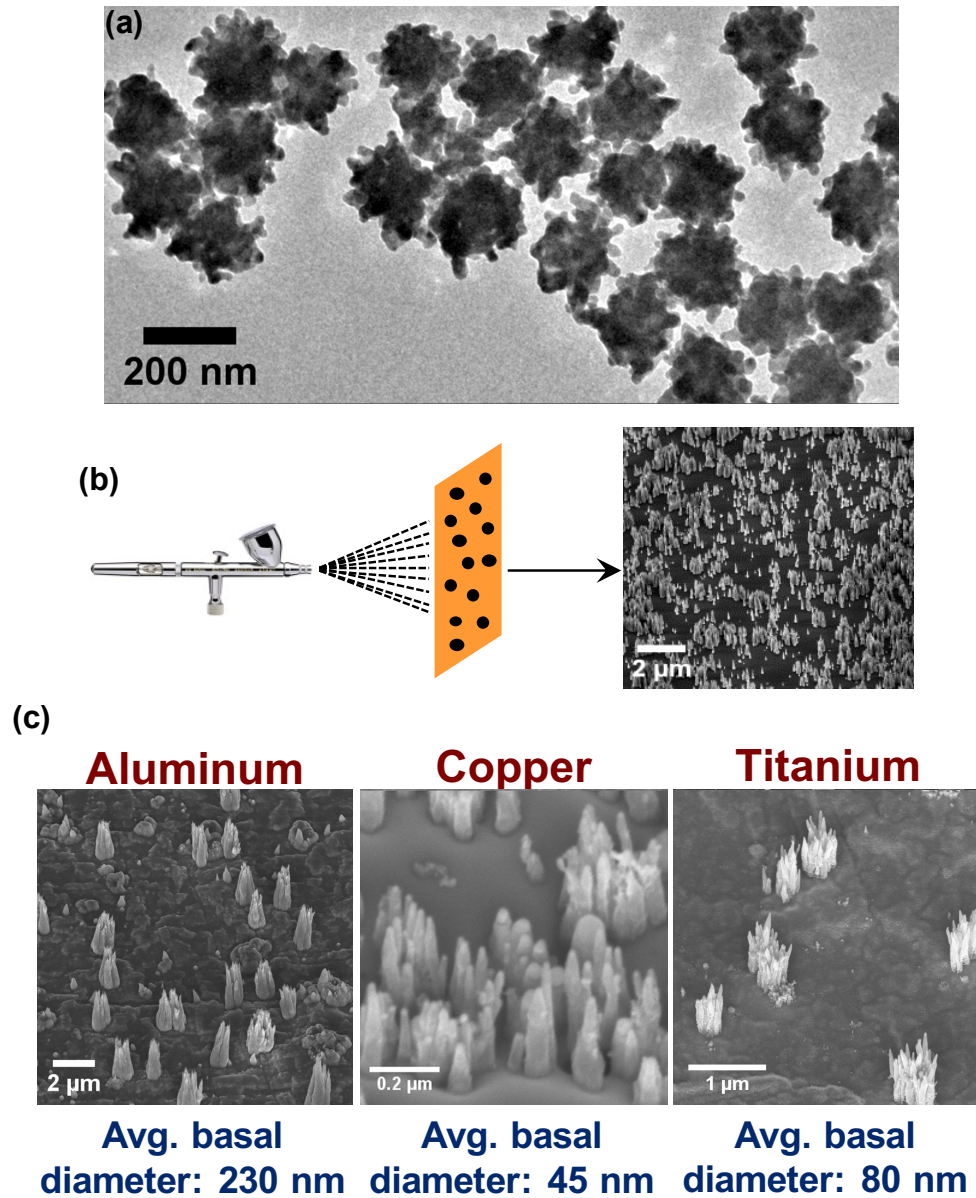


Figure 1. (a) TEM image of 150 nm Ni NPs used to grow VACNFs. (b) A schematic illustrating a simplified method of depositing Ni NPs and silicon powder to grow VACNFs. (c) SEM images of VACNFs grown on aluminum, copper, and titanium substrates.

8.2 Transfer of Vertically Aligned Carbon Nanofibers to Polydimethylsiloxane (PDMS) While Maintaining their Alignment and Impalefection Functionality²

This project was a continuation of the project in section 8.1. The VACNFs that were grown from our Ni NP catalysts and silicon powders deposited by the air brushing technique that we developed were embedded into a PDMS membrane (**Figure 2**).

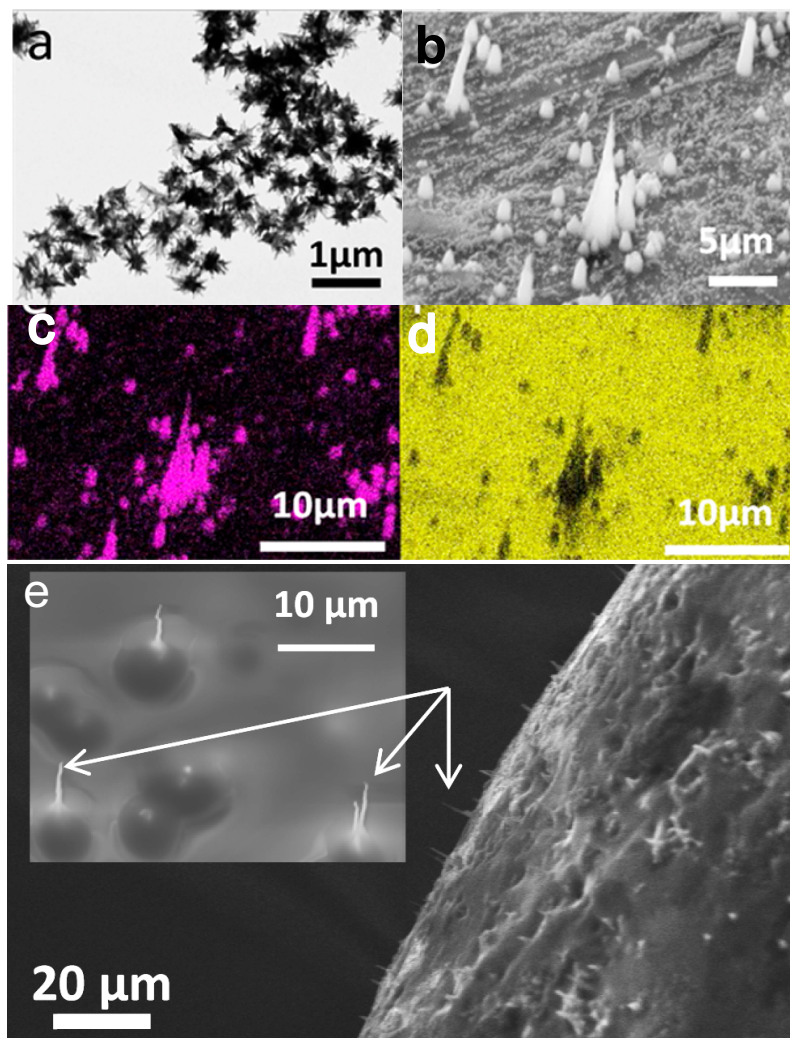


Figure 2. Images of Ni NPs, VACNFs, and VACNFs embedding PDMS (a) TEM images of the Ni NPs (b) SEM image of the silicon nitride coated VACNFs grown on an aluminum substrate (c) EDX map illustrating the location of silicon in the same area as panel b (d) EDX map illustrating the location of aluminum in the same area as panel b (e) VACNFs that project from the surface of PDMS.

8.3 Silica overcoating of nickel and Fe_3O_4 nanoparticles in a reverse microemulsion

I participated on this project with Brian Lynch. Mr. Lynch was a new graduate student in Dr. Joseph Tracy's research group and was developing a project a project for using

Ni NPs in gas phase catalytic reactions. However, during catalysis, coking becomes problematic, which carbon forms on the surface of the catalytic NPs. The carbon decreases the catalytic effectiveness of the Ni NPs, therefore it was proposed that silica may be able to prevent the buildup of carbon on the nickel surface by fabricating SiO₂ overcoated Ni (SiO₂-Ni) NPs. Mr. Lynch was tasked with conducting the studies of using SiO₂-Ni NPs for conducting gas phase catalytic reactions. I contributed to this project by training and helping Brian develop the initial phases of his project. I trained Mr. Lynch in fabricating Ni NPs for his studies. I then developed a procedure using a reverse microemulsion to form a SiO₂ shell on the Ni NPs. During formation of the SiO₂ shell, Ni NPs were found to disassociate from being a single NP to form small Ni nuclei dispersed in the SiO₂ matrix. I also performed initial TEM analyses on Ni NPs and SiO₂-Ni NPs to help confirm the NP morphologies.

In developing the SiO₂ overcoating for Ni NPs, I successfully adapted methods for overcoating Fe₃O₄ NPs (**Figure 3**). The composite NPs can have low and higher loadings of Fe₃O₄ NPs. The method that was used for encapsulating the NPs made was easily adaptable for overcoating Ni NPs for Mr. Lynch's project.

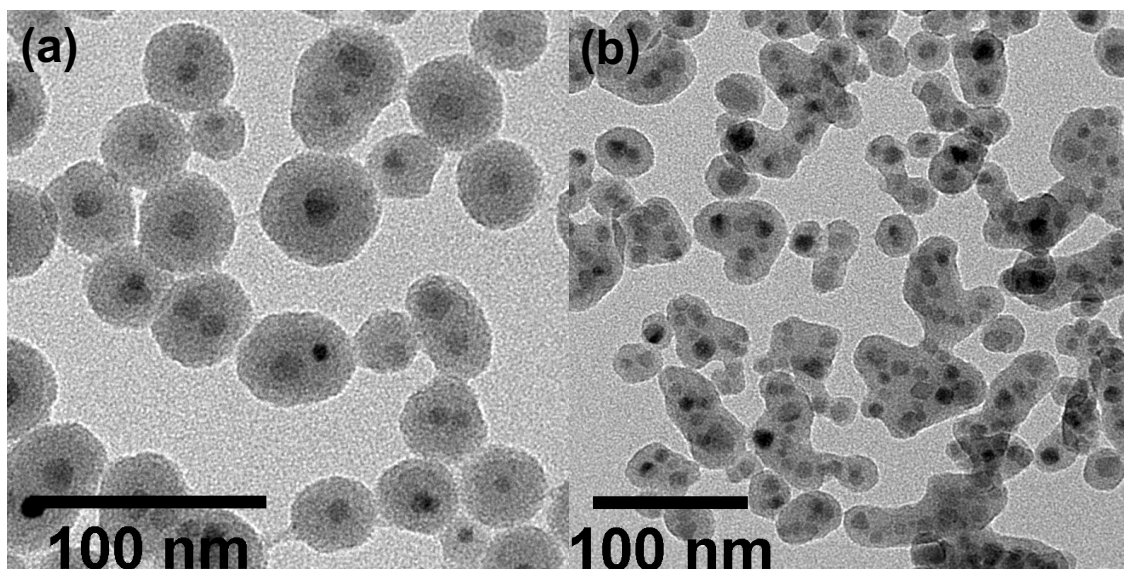


Figure 3. TEM images of SiO₂ overcoated Fe₃O₄ NPs with (a) low loading of NPs and (b) high loading of Fe₃O₄ NPs.

8.4 Synthesis of porous nickel sulfide nanoparticles obtained through the Kirkendall effect

This project is an extension of the review article that I authored on NP conversion chemistry.³ Here, I worked with undergraduate students, Andrew Kelliher and Alexander Japit, on the development of porous nickel sulfide NPs by reacting Ni NPs with sulfur precursors (**Figure 4**). The Ni NPs served as a initial template and, when reacted with sulfur, a diffusion couple is established with sulfur species. As sulfur diffuses towards the center of the Ni NP to react with Ni ions, Ni diffuses towards the surface to react with S ions. A porous structure forms when the relative outward diffusion rate of Ni exceeds inward diffusion rate of sulfur. We fabricated nickel sulfide NPs of various compositions by reacting Ni NPs with different sulfur precursors (**Figure 4**). We also varied reaction temperatures to form new phases of nickel sulfide. The project is ongoing, but we have so far been able to

synthesize many different types of nickel sulfide NPs while controlling the development of porosity in the NPs.

The importance of this project is that we are able to study and control the formation NPs with controlled chemistries and morphologies. This is important for applications that may rely on the NP core chemistry or may rely on NPs that have high surface areas for employment into applications. The review article that I authored discusses potential applications for these types of particles.³

S-precursor	Composition	
	290 °C	350 °C
1-hexadecanethiol	Ni ₉ S ₈	Ni ₉ S ₈
TOP:S	Ni ₃ S ₂	Ni ₃ S ₂
	NiS	
elemental sulfur	Ni ₉ S ₈	Ni ₉ S ₈
	NiS	
	Ni ₁₇ S ₁₈	NiS

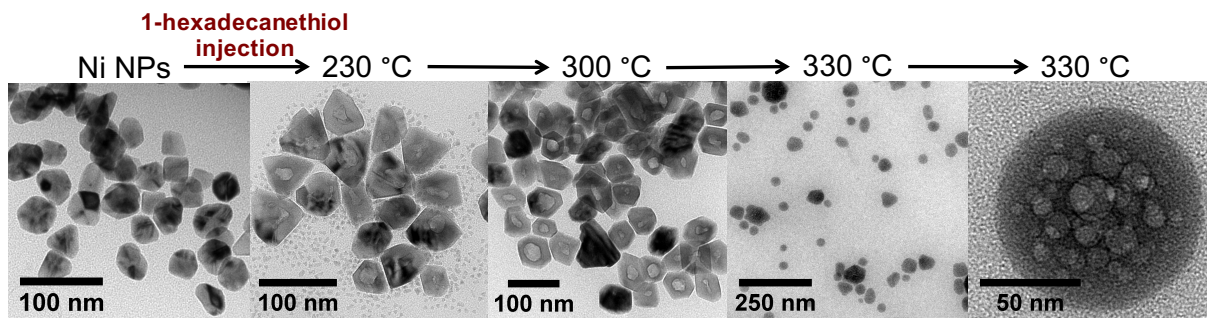


Figure 4. A table indicating the compositions of nickel sulfide synthesize and TEM images of the formation of porosity when Ni NPs react to form nickel sulfide.

8.5 Surface modification and convective assembly of PbS nanoparticles

This is another project where I worked closely with an undergraduate student, Daniel Hernandez, from Texas State University. Daniel participated in the Research Experience for Undergraduate (REU) program and was conducting research in the convective assembly of nanoparticles. Octahedral PbS NPs (**Figure 5a**) were being investigated for convective assembly since the morphology of the NPs could allow for increased packing density when assembled into a monolayer. The particles needed to be water soluble to be compatible with the convective assembly process that Daniel is familiar with in his research lab. To impart water solubility on the PbS, I established a route to perform a silica overcoating on the NPs (**Figure 5b-5e**). I conducted TEM analysis on the SiO₂ overcoated PbS particles to confirm morphology.

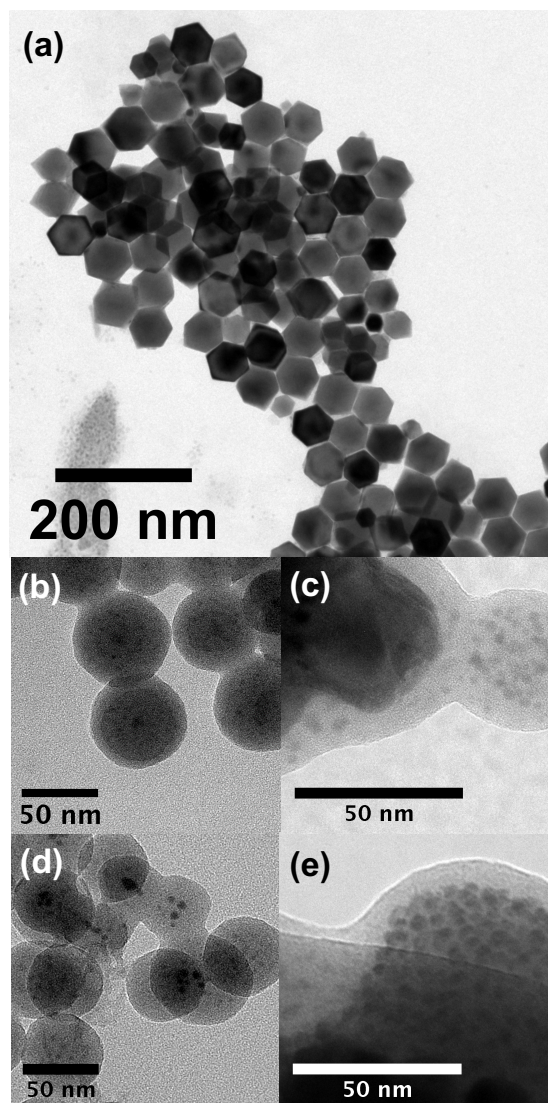


Figure 5. TEM images of (a) PbS NP (b-e) SiO₂ overcoated PbS NPs. The images show that the PbS NPs partially decompose during the SiO₂ overcoating synthesis.

8.6 References

1. Sarac, M. F.; Anderson, B. D.; Pearce, R. C.; Railsback, J. G.; Oni, A. A.; White, R. M.; Hensley, D. K.; LeBeau, J. M.; Melechko, A. V.; Tracy, J. B., *Acs Applied Materials & Interfaces* **2013**, 5, (18), 8955-8960.

2. Pearce, R. C.; Railsback, J. G.; Anderson, B. D.; Sarac, M. F.; McKnight, T. E.; Tracy, J. B.; Melechko, A. V., *ACS Applied Materials & Interfaces* **2013**, 5, (3), 878-882.
3. Anderson, B. D.; Tracy, J. B., *Nanoscale* **2014**, 6, (21), 12195-12216.